

ABSTRACT

ROBERTSON, BENJAMIN DANIEL. Linking Form and Function: Frequency-Phase Coupling in Biological Muscle-Tendon Unit and the Impact of Exoskeleton Assistance. (Under the direction of Dr. Gregory S. Sawicki).

The overall goal of the four studies presented herein is to identify physiological factors (i.e. form) that ultimately govern mechanical behavior at the muscle, joint, and limb level (function), as well as the mechanical and energetic effects of modifying form through the use of passive elastic exoskeletons. This was done using computational and experimental models of vertical hopping.

Computational model of unassisted hopping consisted of a Hill-type muscle model of the triceps surae-Achilles tendon complex working against a gravitational load during cyclic contractions. In chapter 1, we used this model to sweep a 2D parameter space of frequency and magnitude of muscle stimulation centered on the passive resonant frequency (ω_0) of the modeled biological-inertial system. Results from this study indicate that frequency of stimulation plays a primary role in regulating whole muscle-tendon unit (MTU) dynamics, including phase of stimulation and peak force, average positive power, and apparent efficiency. Stimulation amplitude was primarily responsible for regulating peak active forces, contractile element (i.e. active muscle, CE) and series elastic element (i.e. tendon, aponeurosis, SEE) interaction, and overall metabolic demand. Peak ‘tuning’ of CE-SEE interaction in this study was observed at driving frequencies just above ω_0 of the passive MTU system.

Due to known inaccuracies of Hill-type muscle models, chapter 2 replaced the modeled MTU with a biological one from the American bullfrog *Rana Catesbeiana*, and simulated inertial environments similar to those in chapter 1 on a feedback controlled

ergometer. We characterized ω_0 by allowing the MTU to oscillate passively against simulated gravitational loads, and drove the muscle contraction via direct nerve stimulation across a range of frequencies centered on ω_0 . We found that a driving frequency of ω_0 maximized force output, minimized the ratio of CE to MTU work, minimized estimated metabolic demand, and maximized MTU apparent efficiency due to inherent frequency-phase coupling of system dynamics. This study concludes that high level active control are not required to ‘tune’ muscle tendon interactions if driving frequency matches ω_0 of the passive biomechanical system.

Computational models of Exo assisted hopping in chapter 3 were developed using the same base model as chapter 1, with the addition of a linear spring in parallel to modeled biological components. By sweeping a 2D parameter space of stimulation amplitude and Exo stiffness at a fixed frequency, we were able to identify trends in observed behavior that mimic human response to Exo assisted hopping. This included constant MTU+Exo stiffness and CE positive power output, reductions in MTU force, SEE energy cycling, MTU apparent efficiency, and metabolic demand, and increases in MTU+Exo efficiency. This model also provided insight into mechanisms underlying metabolic cost minimization and enhanced performance in Exo assisted hopping, and concludes that these outcomes cannot be optimized simultaneously, i.e. one must come at the detriment of the other.

Our final experimental study used a preparation similar to that from Chapter 2, with modified environment controllers that simulated an exoskeleton in parallel with the biological MTU. We used a ‘pulsed’ rate coding approach to control relative levels of stimulation amplitude, and selected stimulation amplitude-Exo stiffness combinations from

chapter 3 that mimicked human response to exoskeleton assistance. In all conditions, the biological MTU was driven at its estimated ω_0 . This study indicates that increased ω_0 due to an artificially stiffened MTU+Exo system, along with invariant stimulation frequencies, may be a critical factor limiting beneficial response to springy assistance.

© Copyright 2014 by Benjamin D. Robertson

All Rights Reserved

Linking Form and Function: Frequency-Phase Coupling in Biological Muscle-Tendon Unit,
and the Impact of Exoskeleton Assistance

by
Benjamin Daniel Robertson

A dissertation submitted to the Graduate Faculty of
North Carolina State University
in partial fulfillment of the
requirements for the degree of
Doctor of Philosophy

Biomedical Engineering

Raleigh, North Carolina

2014

APPROVED BY:

Dr. Gregory S. Sawicki
Committee Chair

Dr. Richard L. Segal

Dr. Elizabeth G. Loba

Dr. Alper Bozkurt

Dr. Lawrence M. Silverberg

DEDICATION

I would like to dedicate this work to all those who have supported me throughout my graduate studies.

- To my parents, grandparents, and siblings, thank you for your continuous love and support. Without you, none of this would have been possible. I love you all.
- To Dr. Sawicki and the rest of the PoWeR lab, thank you for your patience, constructive criticism, and encouragement throughout my graduate studies. Research is a group effort, and y'all made it a wonderful experience.
- Finally, to my girlfriend Brigitte Crawford, there are no words appropriate to express the thanks I feel that you are part of my life. Your love, patience, and constant encouragement have been a source of strength for me. You never lost faith in me, even when I had none in myself. I can never thank you enough for that.

BIOGRAPHY

I was born in Chicago, Illinois on June 7th, 1986, and graduated high school in The spring of 2004. For my undergraduate education, I attended Emory University and received a B.S. in Applied Physics in the spring of 2008. During my time at Emory, I was fortunate enough to get involved in undergraduate research in the labs of Dr. Stefan Koehler and Ivan Raznik. In the Koehler lab, I studied the mechanics of self-propulsion while submerged in a loose granular media (i.e. fluidized sand) using a bio-inspired robotic swimmer. With the Rasnik lab, I used fuzzy logic algorithms to understand the molecular mechanics of viral helicase function.

Following my undergraduate studies, I received a Science and Engineering Apprenticeship Program (SEAP) fellowship to investigate biomechanical, electrophysiological, and biochemical mechanisms of closed head traumatic brain injury (i.e. blast concussion) in the laboratory of Dr. Debra Yourick at the Walter Reed Army Institute of Research.

My previous work in biomechanics, robotics, controls, and neural instrumentation led me to the lab of Dr. Greg Sawicki, where I was able to apply these skills to investigate the functional neuromechanics of human movement, and the neurophysiological/mechanical impact of wearable robotic devices designed to assist/enhance human movement. This most recent work is contained herein.

ACKNOWLEDGMENTS

I would like to acknowledge several individuals for their contributions to the work herein:

- Dr. Gregory Sawicki, without whom none of this would have been possible. Thank you for material, personal, and intellectual support throughout this process.
- Sid Vadakkevedu, for assisting on almost all of the experimental work presented here. Thank you for your dedication and effort.
- Finally, I would like to generally thank current and past members of the Human PoWeR lab for their continued encouragement and support.

TABLE OF CONTENTS

LIST OF TABLES	vii
LIST OF FIGURES	viii
GENERAL INTRODUCTION	1
References	4
CHAPTER 1: EXPLOITING ELASTICITY: MODELING THE INFLUENCE OF NEURAL CONTROL ON MECHANICS AND ENERGETICS OF ANKLE MUSCLE-TENDONS DURING HUMAN HOPPING	6
1.1 Abstract	6
1.2 Introduction	7
1.3 Methods	10
1.4 Results	20
1.5 Discussion and Conclusions	25
1.6 Future Directions	31
References	48
CHAPTER 2: FREQUENCY-PHASE COUPLING IN CYCLICALLY DRIVEN BIOLOGICAL MUSCLE-TENDONS	55
2.1 Abstract	55
2.2 Introduction	56
2.3 Results	61
2.4 Discussion and Conclusions	66
2.5 Future Directions	70
2.6 Materials and Methods	70
References	86
CHAPTER 3: MORE IS NOT ALWAYS BETTER: MODELING THE EFFECTS OF ELASTIC EXOSKELETON COMPLIANCE ON UNDERLYING ANKLE MUSCLE-TENDON DYNAMICS	91
3.1 Abstract	91
3.2 Introduction	92
3.3 Methods	95
3.4 Results	102
3.5 Discussion and Conclusions	105
3.6 Future Directions	112
References	124
CHAPTER 4: A BIO-ROBOTIC FRAMEWORK FOR EVALUATING MUSCLE-LEVEL EFFECTS OF EXOSKELETON ASSISTANCE IN A COMPLIANT MUSCLE-TENDON UNIT	129
4.1 Abstract	129
4.2 Introduction	130
4.3 Materials and Methods	134
4.4 Results	146

4.5 Discussion and Conclusions	151
4.6 Future Directions	156
References	170
GENERAL CONCLUSIONS	176
References	179

LIST OF TABLES

CHAPTER 1: EXPLOITING ELASTICITY: MODELING THE INFLUENCE OF NEURAL CONTROL ON MECHANICS AND ENERGETICS OF ANKLE MUSCLE-TENDONS DURING HUMAN HOPPING

Table 1 **Model Parameters**33

Table 2 **Model Equations**34

CHAPTER 2: FREQUENCY-PHASE COUPLING IN CYCLICALLY DRIVEN BIOLOGICAL MUSCLE-TENDONS

Table 1 **Measured and Estimated Parameters**76

Table 2 **Regression Fits**.....77

CHAPTER 3: MORE IS NOT ALWAYS BETTER: MODELING THE EFFECTS OF ELASTIC EXOSKELETON COMPLIANCE ON UNDERLYING ANKLE MUSCLE-TENDON DYNAMICS

Table 1 **Model Parameters**113

Table 2 **Model Equations**114

CHAPTER 4: A BIO-ROBOTIC FRAMEWORK FOR EVALUATING MUSCLE-LEVEL EFFECTS OF EXOSKELETON ASSISTANCE IN A COMPLIANT MUSCLE-TENDON UNIT

Table 1 **Measured and Estimated Parameters**158

Table 2 **Regression Fits**.....159

Table 3 **Paired t-tests**161

LIST OF FIGURES

CHAPTER 1: EXPLOITING ELASTICITY: MODELING THE INFLUENCE OF NEURAL CONTROL ON MECHANICS AND ENERGETICS OF ANKLE MUSCLE-TENDONS DURING HUMAN HOPPING

Figure 1	Model Schematic	35
Figure 2	Cycle Dynamics	36
Figure 3	Hop Height and Injury Risk	37
Figure 4	Peak Force	39
Figure 5	Force Sharing	40
Figure 6	Stimulation and Force Phasing	41
Figure 7	Muscle Operating Point	42
Figure 8	Average Power Output	43
Figure 9	Average Power Sharing	45
Figure 10	Metabolic Rate and Apparent Efficiency	46
CHAPTER 2: FREQUENCY-PHASE COUPLING IN CYCLICALLY DRIVEN BIOLOGICAL MUSCLE-TENDONS		
Figure 1	Experimental Schematic and Sample Data	78
Figure 2	Cycle Dynamics	80
Figure 3	Peak Force, Phasing, and CE Operating Point	81
Figure 4	Average Power Output and Sharing	82
Figure 5	Estimated Metabolic Cost and Apparent Efficiency	84
CHAPTER 3: MORE IS NOT ALWAYS BETTER: MODELING THE EFFECTS OF ELASTIC EXOSKELETON COMPLIANCE ON UNDERLYING ANKLE MUSCLE-TENDON DYNAMICS		
Figure 1	Model Schematic	115
Figure 2	Injury Risk and Hop Height	116
Figure 3	Average Power and Workloop Dynamics	117
Figure 4	Force and Power Sharing	118
Figure 5	CE Operating Point	119
Figure 6	Metabolic Rate and Apparent Efficiency	120
Figure 7	Comparison to Human Data	122
CHAPTER 4: A BIO-ROBOTIC FRAMEWORK FOR EVALUATING MUSCLE-LEVEL EFFECTS OF EXOSKELETON ASSISTANCE IN A COMPLIANT MUSCLE-TENDON UNIT		
Figure 1	Experimental Schematic and Sample Data	162
Figure 2	Cycle Dynamics	164
Figure 3	Peak Force, Phasing, and CE Operating Point	165
Figure 4	Average Power Output and Sharing	167
Figure 5	Estimated Metabolic Rate and Apparent Efficiency	169

GENERAL INTRODUCTION

The human leg consists of three major joints, all of which spanned by mono- and multi-articular muscles of variable size, degree of pennation, fiber type, and attachment geometry. Despite its inherent physiological complexity, the mechanical behavior of the human leg is remarkably simple. All modes of human bouncing gait (i.e. walking, running, and hopping) can be predicted by treating the entire leg as a simple linear compression spring supporting a point mass [1,2]. While much is known about the physiology, or ‘form’, of the lower limb, as well as its ultimate spring-like mechanical ‘function’, little is understood about the link between the two.

To begin approaching this problem, researchers have relied on ankle-driven hopping as an experimental model. This behavior is of utility for understanding links between form and function because it preserves the spring-like whole limb behavior, while simultaneously minimizing the involvement of higher level joints, thereby reducing the physiological complexity of movement [3,4]. As with walking and running [5], the ankle joint, and the triceps surae-Achilles tendon complex in particular, provide the majority of mechanical work/power required for hopping [6]. By studying movement patterns primarily driven by a single muscle-tendon unit, linking form and function becomes a challenge of reduced order.

Many classic studies of hopping have used a ‘frequency response’ approach to probing limb mechanics. In doing so, investigators have identified movement frequencies

which ‘tuned’ interactions between muscle and tendon by coordinating muscle activation timing with body inertial dynamics to store and return the majority of mechanical energy required for hopping in series tendon [3,7-9]. The first two chapters of this dissertation focus on this sort of ‘resonant’ limb behavior, and the role that driving frequency plays in its emergence using both computational and experimental models of ankle-driven hopping. Unlike previous studies, however, this one ties ‘form’ back to ‘function’ by identifying how the combination of passive biological stiffness, limb geometry, and inertial loads govern driving frequencies for which ‘tuned’ interactions are observed.

Other classical experiments in hopping have modified ‘form’ through the additional of parallel stiffness via wearable passive exoskeletons [9-13]. In doing so, investigators have found that it is possible to reduce metabolic demands of hopping at the expense of ‘function’ [9,12,13]. That is to say, reducing biological loads via external assistance disrupts the ‘tuned’ interaction of biological muscle and tendon of the ankle plantar flexors, which is dependent on high forces for tendon energy storage and return [9]. Emerging evidence shows that the addition of artificial limb stiffness is beneficial *to a point*, and that beyond some terminal device stiffness, metabolic benefits are eliminated [12,14]. In the final two chapters of this work, we use both computer and experimental models of hopping to investigate the influence of modified ‘form’ via external springy assistance, and its influence on ‘function’. We conclude by identifying physiological factors that ultimately limit the potential benefits of external assistance.

Identifying underlying principles linking form to function is not only of use for understanding typical patterns of bouncing gait, but also for understanding emergent characteristics of pathological gait. If a link can be made between altered form (i.e. muscle atrophy, increased tendon compliance, increased body mass, etc.) and pathological function, these same principles may be applied for altering form to *restore* function. This is addressed further in the general conclusions section following chapter 4.

References

1. Blickhan R (1989) The spring-mass model for running and hopping. *J Biomech* 22: 1217-1227.
2. Geyer H, Seyfarth A, Blickhan R (2006) Compliant leg behaviour explains basic dynamics of walking and running. *Proc Biol Sci* 273: 2861-2867.
3. Farley CT, Blickhan R, Saito J, Taylor CR (1991) Hopping frequency in humans: a test of how springs set stride frequency in bouncing gaits. *J Appl Physiol* 71: 2127-2132.
4. Farley CT, Morgenroth DC (1999) Leg stiffness primarily depends on ankle stiffness during human hopping. *J Biomech* 32: 267-273.
5. Farris DJ, Sawicki GS (2012) The mechanics and energetics of human walking and running: a joint level perspective. *J R Soc Interface* 9: 110-118.
6. Farris DJ, Sawicki GS (2012) Linking the mechanics and energetics of hopping with elastic ankle exoskeletons. *J Appl Physiol* 113: 1862-1872.
7. Dean JC, Kuo AD (2011) Energetic costs of producing muscle work and force in a cyclical human bouncing task. *J Appl Physiol* 110: 873-880.
8. Takeshita D, Shibayama A, Muraoka T, Muramatsu T, Nagano A, et al. (2006) Resonance in the human medial gastrocnemius muscle during cyclic ankle bending exercise. *J Appl Physiol* 101: 111-118.
9. Farris DJ, Robertson BD, Sawicki GS (2013) Elastic ankle exoskeletons reduce soleus muscle force but not work in human hopping. *J Appl Physiol* (1985) 115: 579-585.
10. Ferris DP, Bohra ZA, Lukos JR, Kinnaird CR (2006) Neuromechanical adaptation to hopping with an elastic ankle-foot orthosis. *J Appl Physiol* 100: 163-170.

11. Chang YH, Roiz RA, Auyang AG (2008) Intralimb compensation strategy depends on the nature of joint perturbation in human hopping. *J Biomech* 41: 1832-1839.
12. Grabowski AM, Herr HM (2009) Leg exoskeleton reduces the metabolic cost of human hopping. *J Appl Physiol* 107: 670-678.
13. Farris DJ, Sawicki GS (2012) Linking the mechanics and energetics of hopping with elastic ankle exoskeletons. *J Appl Physiol*.
14. Robertson BD, Farris DJ, G.S. S More is not always better: modeling the effects of elastic exoskeleton compliance on underlying ankle muscle-tendon dynamics. *Bioinspir Biomim: In Press*.

CHAPTER 1: EXPLOITING ELASTICITY: MODELING THE INFLUENCE OF NEURAL CONTROL ON THE MECHANICS AND ENERGETICS OF ANKLE MUSCLE-TENDONS DURING HUMAN HOPPING

Benjamin D. Robertson, Gregory S. Sawicki

As published in the Journal of Theoretical Biology

1.1 Abstract

We present a simplified Hill-type model of the human triceps surae-Achilles tendon complex working on a gravitational-inertial load during cyclic contractions (i.e. vertical hopping). Our goal was to determine the role that neural control plays in governing muscle, or contractile element (CE), and tendon, or series elastic element (SEE), mechanics and energetics within a compliant muscle-tendon unit (MTU). We constructed a 2D parameter space consisting of many combinations of stimulation frequency and magnitude (i.e. neural control strategies). We compared the performance of each control strategy by evaluating peak force and average positive mechanical power output for the system (MTU) and its respective components (CE, SEE), force-length (F-L) and –velocity (F-V) operating point of the CE during active force production, average metabolic rate for the CE, and both MTU and CE apparent efficiency. Our results suggest that frequency of stimulation plays a primary role in governing whole-MTU mechanics. These include the phasing of both activation and peak

force relative to minimum MTU length, average positive power, and apparent efficiency. Stimulation amplitude was primarily responsible for governing average metabolic rate and *within* MTU mechanics, including peak force generation and elastic energy storage and return in the SEE. Frequency and amplitude of stimulation both played integral roles in determining CE F-L operating point, with both higher frequency and amplitude generally corresponding to lower CE strains, reduced injury risk, and elimination of the need for passive force generation in the CE parallel elastic element (PEE).

1.2 Introduction

Decades of research on the mechanics and energetics of locomotion has established the role of passive elastic tissues (e.g. tendons, aponeuroses) in shaping efficient and stable movement [1-9]. This concept is best illustrated by simple spring-based models of human locomotion that predict walking [1,10,11], running [1,11,12], and hopping [12,13] mechanics in the absence of any active components (i.e. muscles). These purely elastic models successfully predict center of mass mechanics and are intrinsically stable, but they ignore the contribution of active muscle resonant behavior in the coupled muscle-tendon system.

Other simple modeling frameworks have explored the role that *only* active tissues play in cyclic force/power production and stability of movement [14,15]. Purely muscle-based models can address questions related to the extent that feed-forward and feedback

based neuromuscular control in conjunction with non-linear force-length and –velocity dynamics can stabilize perturbed movements [14,15]. However, these models lack key elastic tissues; both series tendon/aponeurosis *and* parallel structures that can generate force passively in muscle. Both series and parallel elastic tissues can alter the force and length trajectories of the muscle contractile elements, but few models take into account combined muscle-tendon architecture. Models that include series elasticity have given important insight into the role of elastic tissues in optimizing movement (i.e. walking running, jumping, swimming) for minimum metabolic cost, maximum efficiency or maximum mechanical power output [16-18]. None of these studies, however, directly explores how neural control pattern modulates muscle-tendon interaction dynamics during cyclic contractions.

More complex modeling frameworks have been developed for examining the interplay of many muscle-tendon units of the lower limbs during walking, running, and hopping. These models incorporate complex limb geometries with distributed mass , physiologically accurate muscle and tendon architecture, and can track joint-level kinematics and kinetics to predict neuromuscular control patterns with similar timing and magnitude to those observed experimentally [19-25]. This is extremely useful for examining the role of elastic tissues in shaping whole limb, joint, and muscle-level mechanics and energetics [23,24,26]. Complex musculoskeletal models have also been used to predict locomotion behavior based on optimization of some objective function ((i.e minimal metabolic cost/muscle activation, maximum height jumping, etc.) [27]. However, it is unclear that there is a single underlying factor that humans seek to optimize as part of functional gait

[28,29], motivating the need for studies that examine performance along multiple objectives (i.e. metabolic cost, injury risk, stability, efficiency, etc.)

Our goal in this study was to develop a simple framework to examine the fundamental aspects of how neural control (e.g. frequency and magnitude of stimulation) mediate muscle-tendon unit (MTU) dynamics during functional movement. For example, utilizing active muscle versus passive elastic tissues to modulate compliant limb/joint mechanics may allow for more robust control, but also requires consumption of additional metabolic energy- an important trade-off that may shape preferred movement strategies. Many studies have shown that a coupled muscle-tendon system can significantly reduce energy costs with little effect on overall power output by minimizing muscular length change, and maximizing energy storage and return in series elastic tissues [1,3,9,30-32]. Under these conditions, the muscle is said to be contracting isometrically, and the muscle-tendon unit (MTU) is “tuned” to exploit compliance. When a MTU becomes tuned there are significant reductions in contractile element (CE) mechanical power and increases in peak force; both of which likely play an important role in overall metabolic cost and efficiency of movement [9,19,31,32] . The benefits of an optimally tuned MTU are clear, but the role of the central nervous system in coordinating the timing and magnitude of muscle activation to optimize elastic energy storage in and return in series elastic elements (SEE) is not.

In this study we explored how a compliant MTU responded to different frequencies and magnitudes of stimulation during a simple, rhythmic movement (i.e. human hopping) that relies heavily (up to ~80% of limb total positive mechanical power) on the ankle muscle

tendon units (i.e. triceps-surae Achilles tendon complex) to perform the mechanical work required by the task [33]. To simplify the model, we lumped the triceps-surae muscle group into a single, mono-articular muscle with a series tendon and a fixed mechanical advantage (**fig. 1**). We started our exploration of possible operating frequencies by first finding the resonant frequency ($\omega_{MTU\ resonance}$) of the passive mechanical system under the load of the body in the absence of any CE activation. For the system detailed here, we found $\omega_{MTU\ resonance} = 2.1$ Hz. We hypothesized that stimulating this compliant muscle-tendon system at $\omega_{MTU\ resonance}$ would ‘tune’ the mechanical system and (1) maximize MTU force generation and elastic energy storage and return in the SEE and (2) minimize CE work for any given stimulation amplitude. We also expected that (3) the amplitude of muscle stimulation would modulate force/power production between CE and SEE within the MTU. Finally, we predicted that, owing to the fact that low velocity contractions are metabolically inexpensive [34], driving the MTU at $\omega_{MTU\ resonance}$ would (4) minimize metabolic rate and maximize MTU apparent efficiency.

1.3 Methods

To investigate the effect that neural control has on the mechanics and energetics of human hopping we developed a mathematical model of a cyclically stimulated compliant MTU (i.e. bouncing gait). The model included a massless Hill-type muscle and parallel elastic element (PEE) collectively referred to here as the CE, in series with a non-linear tendon-spring, or

SEE, operating with a fixed mechanical advantage on a point mass experiencing constant gravitational forces; which captures the muscle-tendon dynamics at distal joints of the lower-limb (e.g. ankle) (**fig. 1**). To approximate mechanical properties of the human triceps-surae Achilles tendon complex, several key simplifications were made. First and foremost, we combined the gastrocnemii and soleus muscles into a single, monoarticular, muscle. This disregards the fact that the gastrocnemii muscles act across both the ankle and knee joints, which will limit our models ability to reliably predict MTU mechanics under conditions where humans no longer exhibit spring-like behavior and employ deep knee bends as part of functional gait (i.e. low frequency hopping, $\leq \sim 2.0$ Hz) [35]. Secondly, we model our lumped triceps-surae muscle group as non-pennate. Experimental studies exploring decoupling of fascicle and whole-muscle length/velocity dynamics due to pennation have demonstrated that there is little difference between the two under high force conditions like those modeled here [36]. Third, the mechanical advantage of this system was fixed, disregarding shifts in moment arm length that occur in an intact biological system during overground gait (i.e. walking and running) [37,38]. We believe this to be a reasonable approximation for hopping, as there are no dramatic shifts in center of pressure over the course of ground contact as might be observed in forward progression [37-39]. Fourth, there are no antagonist muscles in this model; cyclic mechanics arose from interplay between our modeled triceps surae and gravitational and inertial forces acting on a point mass. Our mass was modeled as half body mass to approximate loads experienced during two-legged hopping. Finally, there were no set configuration for a flight phase. There was, however, an

‘aerial’ portion in which MTU-load coupling goes slack for a large portion of modeled conditions, and the only force remaining is gravitational (**figs. 2, 3a**). Model parameters and equations can be found in **tables 1** and **2** respectively.

1.3.1 Muscle Activation Dynamics

Force is generated in our modeled CE by a Hill-type muscle with classic, normalized, non-linear force-length (F-L) and –velocity (F-V) relationships, and non-linear PEE with slack length l_0 based on equations from Azizi et. al. [40-42] (**table 2**). Experimental measurements used to derive human F-L fit values were generously provided by Rubenson et. al. [43]. Normalized F-V curves were taken from Haeufle et. al. [14] and based on experimental curves from Hill [44].

Stimulation was modeled as a square wave pulse that had a duty equal to 10% of the cycle period T_{stim} (i.e. $T_{stim} = \omega_{stim}^{-1}$, stimulation duty = $0.1 * T_{stim}$) (**fig. 2**). This square wave was subject to a first order excitation-activation coupling dynamics to generate a corresponding activation function $\alpha(t)$ to drive muscular contraction, resulting in an activation/active force duration of 50-80% of a cycle. These values are in agreement with experimentally observed force/EMG duties [33,45-47] (**fig. 2**). Force generated by the CE was equal to:

$$F_{CE} = F_{max} * \alpha(u(t), \tau_{act}, \tau_{deact}) * F_{l\ active}(l_{CE}, l_0) * F_v(v_{CE}, v_{max}) + F_{l\ passive}(l_{CE}, l_0)$$

Where F_{CE} is total CE force, F_{max} was maximum active isometric force possible from the CE, $\alpha(u(t), \tau_{act}, \tau_{deact})$ was normalized muscle activation in terms of periodic square-wave stimulation $u(t)$, as well as muscle activation (τ_{act}) and relaxation (τ_{deact}) time constants [19,47]. Time constants were determined by taking a weighted average of reported values for medial/lateral gastrocnemius and soleus based on their peak cross-sectional area [48-50]. F_l was instantaneous normalized F-L operating point as a function of muscle length (l_{CE}) and l_o for muscle. F_v was instantaneous normalized F-V operating point in terms of rate of muscular length change (v_{CE}) and v_{max} for the CE. Normalized F-L and F-V relationships are visualized in **fig. 7**, and their equations can be seen in **table 2**. Muscle and system parameter values used were based on literature values for human plantar flexors and can be found in **table 1**.

1.3.2 Tendon Dynamics

The SEE in our compliant MTU was modeled with a non-linear “toe” region at operating points just above the slack length, after which its stiffness can be approximated as linear [5-7]. Forces generated in the SEE are described by the following relationship:

$$F_{SEE} = \begin{cases} 0 & l_{SEE} \leq l_{slack} \\ k_{SEE}(k_t, F_{CE}) * (l_{SEE} - l_{slack}) & l_{SEE} > l_{slack} \end{cases}$$

Where k_{SEE} was the stiffness function for the tendon (**table 2**), l_{SEE} was the length of the SEE, and l_{slack} was the slack length of the SEE, below which it cannot store or return energy.

1.3.3 Model Implementation

Periodic excitation of the ‘lumped’ triceps-surae Achilles tendon MTU was modeled for a range of stimulation values (10-100% of maximum) and frequencies (1-4Hz) about the resonant frequency of the passive mechanical system ($\omega_{MTU\ resonance} \sim 2.1\text{ Hz}$). All simulations were run for 15 seconds with a fixed time step ($dt = 0.0005\text{ s}$) and used the 4th order Runge-Kutta method to solve for system dynamics (MATLAB 2010b, MathWorks Inc). The last four cycles of stimulation were used in final analysis to be sure that the system had ample time to settle into steady-state mechanics.

1.3.3.1 Periodic Behavior

The relationship between ω_{MTU} , the frequency of MTU mechanical output, and ω_{stim} , the frequency of stimulation input, was of fundamental interest in this study. There was an assumed relationship:

$$\omega_{MTU} = n * \omega_{stim}$$

where n is a scalar multiple. To determine periodicity with stimulation, we developed a metric dubbed the “integrated return map” (IRM) based on the variability of MTU length (l_{MTU}) and velocity (v_{MTU}) dynamics within each of the K cycles included in final analysis (for all work presented here, $K=4$). First we averaged $l_{MTU}(t)$ and $v_{MTU}(t)$ values from each of our K cycles for every timepoint $t = [0, T_{stim}]$ within a given cycle of stimulation, with

T_{stim} being the period of stimulation (i.e. $T_{stim} = \omega_{stim}^{-1}$). Mean position ($\bar{l}_{MTU}(t)$) and velocity ($\bar{v}_{MTU}(t)$) values were computed as follows:

$$\bar{l}_{MTU}(t) = \left(\sum_{k=1}^K l_{MTU}(t, k) \right) / K, \quad \bar{v}_{MTU}(t) = \left(\sum_{k=1}^K v_{MTU}(t, k) \right) / K$$

The absolute difference between average and individual $l_{MTU}(t)$ and $v_{MTU}(t)$ values was then integrated over period T_{stim} for K cycles used in analysis, and summed to determine an IRM value for each condition as follows:

$$IRM(\omega_{stim}, A_{stim}) = \sum_{k=1}^K \left[\int_{t=0}^{T_{stim}} [|l_{MTU}(t, k) - \bar{l}_{MTU}(t)| + |v_{MTU}(t, k) - \bar{v}_{MTU}(t)|] * dt \right]$$

Where ω_{stim} and A_{stim} were the frequency and magnitude of stimulation for each experimental condition. IRM values within an acceptable range to be considered round off error (i.e. $IRM \approx 0$), indicate dynamics that were cyclic with stimulation, or had period one dynamics (i.e. $\omega_{MTU} = \omega_{stim}, n = 1$). Conditions exhibiting $n \neq 1$ mechanics (i.e. $\omega_{MTU} \neq \omega_{stim}$) had IRM values several orders of magnitude larger than those for $n=1$ conditions (i.e. $IRM \neq 0$).

1.3.3.2 Flight Phase

Hopping was considered to encompass any emergent behavior consisting of alternating flight and ground contact phases. Flight was defined as any instance where our point mass acceleration was equal to that of gravity (e.g. $F_{net} = Mg$, **table 1**).

1.3.3.3 Injury Risk and Average Strain

Injury risk was determined based on peak eccentric engineering strain using the following equation:

$$\epsilon_{peak} = \max((l_{CE}(t) - l_0)/l_0) \quad \text{when } (dl_{CE}(t)/dt) > 0$$

High potential for injury was associated with $\epsilon_{peak} > .3$ based on in-vitro experiments in animal tissues [51-55].

We also chose to examine the average CE strain during active force production to evaluate what, if any, conditions operated closest to l_0 while the muscle was in an active state. Average strain was evaluated as follows:

$$\bar{\epsilon}_{CE} = \text{mean}(\text{abs}((l_{CE}(t) - l_0)/l_0)) \quad \text{when } \alpha(u(t), \tau_{act}, \tau_{deact}) > .01$$

1.3.3.4 Peak Force

To further assess mechanical performance we computed peak MTU force over a cycle of stimulation. MTU peak force is equivalent to peak forces produced in both the CE and SEE, and is a good indicator of the amount of elastic energy cycling in the SEE.

The peak value of force was taken for each of the four cycles used in analysis, normalized to F_{max} , and averaged for all conditions. The CE can produce force both actively *and* passively at operating lengths greater than l_0 . To understand how active and passive elements of CE contribute to total CE force we computed the percentage from each as follows:

$$\%F_{CE\ active}^{max} = F_{CE\ active}(t_{max})/F_{MTU}(t_{max}) * 100$$

Where $F_{CE\ active}$ is force produced actively in the CE, and t_{max} is the time of peak MTU force for a given cycle. The percentage of contribution to F_{MTU}^{max} from passive elements in the CE adhered to the relationship:

$$\%F_{CE\ passive}^{max} = 100 - \%F_{CE\ active}^{max}$$

1.3.3.5 Stimulation and Peak Force Phase Metrics

To assess the whether or not stimulation onset timing was a contributing factor in hopping behavior, we assessed the average phasing of the time of both CE stimulation onset and MTU peak force in a cycle of hopping relative to the time within a given cycle when MTU is at its shortest length. These phase delays are reported as a percentage of the period of stimulation, $T_{stim} = \omega_{stim}^{-1}$.

1.3.3.6 Average Positive Mechanical Power

To asses mechanical output of the MTU and its components we computed average positive power (i.e. rate of mechanical work) produced over a cycle of stimulation. We chose average power because mechanical work performed on the load (i.e. COM) has been strongly associated with metabolic cost of movement [31,56]. We used average *positive* power because SEE's can only cycle energy, and their net power production over a cycle of stimulation is zero for period one mechanics. For a given stimulation frequency ω_{stim} , and ignoring power outputs less than zero:

$$\bar{P}_{mech}^+ = \left[\int_{t=0}^{T_{stim}} P_{mech}^+(t) dt \right] * \omega_{stim}$$

Where \bar{P}_{mech}^+ is average positive mechanical power produced over a cycle of stimulation, $P_{mech}^+(t)$ is positive mechanical power as a function of time, and T_{stim} is the period of stimulation. All stimulation cycles used for analysis were averaged to ensure a reasonable representation for conditions where $n \neq 1$. This method was used to compute average power from the MTU, CE, and SEE with all values normalized to $|F_{max} * v_{max}|$ for the CE (**table 1**).

While overall MTU mechanics are of great importance, our model allowed us to decouple these mechanics to explore CE and SEE contributions. To this end, we looked at the percentage of total positive power produced over a cycle by the CE as follows:

$$\% \bar{P}_{mech CE}^+ = (\bar{P}_{mech CE}^+ / (\bar{P}_{mech CE}^+ + \bar{P}_{mech SEE}^+)) * 100$$

Where $\% \bar{P}_{CE}^+$ is the average percentage of total positive power over a cycle of stimulation from the CE, and \bar{P}_{CE}^+ and \bar{P}_{SEE}^+ are positive power as a function of time for the CE and SEE respectively. The percent contribution from SEE was assumed to adhere to the relationship:

$$\% \bar{P}_{SEE}^+ = 100 - \% \bar{P}_{CE}^+$$

Standard deviations for $\% \bar{P}^+$ were also computed to observe variations from average values for the $n \neq 1$ case.

1.3.3.7 Metabolic Power and Apparent Efficiency

To assess metabolic performance of different control strategies we calculated average metabolic rate, and associated apparent MTU and CE efficiencies. Metabolic rate was determined based on CE velocity, and scaled by activation, using a model taken from [19].

$$P_{met}(t) = p(v_{CE}(t)) * \alpha(t) * |F_{max} * v_{max}|$$

Where $P_{met}(t)$ is instantaneous metabolic rate at time t , and $p(v_{CE}(t))$ is a cost function taken from [16,57] and shown in **table 2**. Average metabolic rate for each condition was computed by integrating instantaneous metabolic cost for each period, multiplying by frequency (i.e. dividing by period), and dividing by the system mass M (**table 1**) to get units of units of Watts/kg (shown below):

$$\dot{P}_{met} = \left[\int_0^{T_{stim}} P_{met}(t) dt \right] * (\omega_{stim}/M)$$

Apparent efficiency of positive mechanical work was also determined for each experimental condition to examine how different neural control strategies utilize metabolic energy to perform mechanical work on the load. Apparent efficiency of positive mechanical work for each component (e.g. MTU, CE) was determined as follows:

$$\bar{e}_{met} = \left(\int_0^{T_{stim}} P_{mech}^+(t) dt \right) / \left(\int_0^{T_{stim}} P_{met}(t) dt \right)$$

Where \bar{e}_{met} is average apparent efficiency, P_{mech}^+ is positive mechanical work, and P_{met} is metabolic cost. Apparent efficiency can be related to the fraction of average positive

mechanical power contributed by the CE versus the SEE (i.e. muscle work fraction = $0.25/\bar{\epsilon}_{met}$) [58].

1.4 Results

1.4.1 Periodic Mechanics

Most stimulation frequency-amplitude combinations resulted in behavior that was periodic with stimulation onset (i.e. $n=1$) (**fig. 2**). The only notable exception to this was for low frequency stimulations ($\omega_{stim} < 1.4$), for which mechanical behavior was period two ($n=2$) and each cycle of stimulation resulted in two hops; one driven by active muscle, and one driven by purely passive forces in the MTU.

1.4.2 Flight Phase

A flight phase was observed for all stimulation frequencies less than ~ 3.4 Hz. Flight required the least stimulation amplitude for frequencies in the 3.0-3.2 Hz range (**fig. 3a**). Conditions that did not achieve flight are indicated by a speckled region bordered in white and labeled “No Flight” in all relevant figures.

1.4.3 Peak and Mean CE Strain

Peak strains associated with elevated risk of injury ($\epsilon_{peak} > .3$) occurred at every frequency for stimulation amplitude below 30% of maximum (**fig. 3b**). In general, lower

stimulation frequencies required higher stimulation amplitude to keep peak strain below .3. For stimulation frequencies > 2.0 Hz, risk of injury could be drastically reduced by increasing stimulation amplitude by amounts that vary depending on the frequency of operation. (**fig. 3b**). While it is entirely possible for humans to hop outside the range of frequencies constrained by this criteria, deep knee bends would be required to reduce injury risk. As a result, these conditions would no longer be considered “ankle driven,” and predictions made by this model are unlikely to be reflective of human behavior.

Values of average CE strain during active force production also showed both strong stimulation frequency and amplitude dependence. For frequencies ≥ 2.2 Hz, it is possible to remain at an average operating length $\sim l_0$ (i.e. $\pm 0.05l_0$, ± 2.75 mm) with the proper stimulation amplitude. This region of parameter space is bordered in white dashed lines in (**figs. 3a,b**) and all subsequent contour plots. From the region bordered in white, if stimulation magnitude or frequency is increased, the average CE operating length will fall below l_0 onto the ascending limb of F-L (**fig. 7a,c**); but if stimulation magnitude or frequency is decreased, the average CE operating length will rise above l_0 onto the descending limb of F-L. It is worth noting that, while a mean operating strain of $\pm 0.05l_0$ allows for a peak isometric force of F_{max} , mean operating strains of $\pm .2l_0$ (± 11 mm) can still produce active forces $\geq .9F_{max}$. This leads to a broad range of operating points capable of producing high active forces without excessive risk of injury.

1.4.4 Peak Force

Peak MTU (as well as CE and SEE) forces were observed in the 2.2-2.4 Hz range and maximal (100%) stimulations (**fig. 4**). At frequencies ≤ 1.8 Hz, peak forces were almost entirely the result of passive forces in the CE. As frequency of stimulation increased, so too did active contributions to CE force (**fig. 5**). The extent to which active forces contribute to CE force production was also dependent on stimulation amplitude. At 70% of maximum stimulation all frequencies required at least some contribution from the CE PEE (e.g. at 2.4 Hz, $\sim 15\%$ of total force is from the PEE) (**fig. 5d**). For maximal stimulation (100%), all CE force was produced actively for stimulation frequencies ≥ 2.6 Hz (**fig 5b**). Conditions in which passive CE force played a significant role also posed significant risk of injury (**fig. 3b, 5a,c**).

1.4.5 Stimulation and Peak Force Phasing

Phasing of stimulation onset relative to MTU minimal length underwent a relatively sharp transition, dropping from $\sim 70\%$ to $\sim 30\%$ near the passive resonant frequency (~ 2.1 Hz) (**figs. 2, 6a**). Furthermore, for combinations of frequency and magnitude of stimulation between 1.6-3.6 Hz and stimulation amplitudes $\geq 50\%$, there is a well-defined “ground contact” phase that is nearly coincident with stimulation onset, resulting in peak forces that occur consistently at 50% of a cycle following the time of MTU shortest length (**fig. 6b**). For frequencies < 1.8 Hz there were two cycles of ground contact and flight per period of stimulation, one driven entirely by passive mechanics and the other by muscle activation.

This ultimately resulted in peak force preceding stimulation onset for these conditions (**fig. 6**). Phasing of stimulation onset and peak MTU force did not depend strongly on stimulation amplitude (**fig. 6**).

1.4.6 CE Operating Length and Velocity

CE operating length and velocity had both stimulation frequency and amplitude dependent effects. In general, increasing either stimulation frequency or amplitude decreases CE operating length-driving it towards the ascending limb; but has little effect on CE operating velocity (**fig. 7**). When stimulation amplitude is held constant and frequency is varied, average operating length decreases as frequency increases (**fig. 7a**). In general, lower frequencies have a greater *range* of CE operating velocities, but *average* CE operating velocity appears to be nearly uniform across frequency at 100% stimulation for cases where little to no passive force is required (i.e. $\omega_{stim} \geq 2.2$ Hz) (**fig. 7b**).

When frequency is held constant at 2.8 Hz (or any frequency > 1.6 Hz), increasing activation simultaneously decreases CE operating length and total excursion (**fig. 7c**). Stimulation amplitude does not affect *average* operating velocity, but does influence the *range* of shortening velocities (**fig 7d**).

1.4.7 Mechanical Power Production

Greatest average positive MTU power output was observed in the 1.8-2.0 Hz range for stimulation amplitudes ranging from 60-100%; and in the 2.2-2.4 Hz range at 100% of

maximum stimulation amplitude (**fig. 8a**). CE average positive power was minimized when operating at frequencies greater than ~ 2.8 Hz (**fig. 8b**). SEE average positive power was maximized in the range of 2.2-2.4 Hz for high amplitude stimulations ($\geq 80\%$) (**fig. 8c**). For frequencies > 1.6 Hz, the SEE contributed the majority of power, ranging anywhere from ~ 55 -85% of total power production at stimulation amplitudes greater than 50% of maximum (**fig. 9**). In general, increasing stimulation amplitude served to increase contribution of SEE to total MTU positive power for all frequencies > 2.0 Hz (**fig. 9**).

1.4.8 Metabolic Rate, MTU and CE Apparent Efficiency

In the range of stimulation frequency/amplitude which poses little to no risk of injury, average metabolic rate was highly dependent on stimulation amplitude (**fig. 10a**). This is indicated by nearly horizontal contours of metabolic rate in 2.0-3.8 Hz range (**fig. 10a**)

MTU apparent efficiency reached a maximal value of ~ 2.0 at 2.2 Hz (i.e. CE work/SEE work fraction = 12.5%/87.5% respectively, **fig. 9b**), and declined with frequency to lows around 1.0 for the 3.6 Hz, 100% stim condition (i.e. CE work/SEE work fraction = 20%/80% respectively **fig. 9b**). MTU apparent efficiency was frequency dependent in regions that safely achieve hopping, as indicated by vertical contours (**fig 10b**).

CE apparent efficiency was strongly dependent on both frequency and amplitude of stimulation as indicated by the angled contours in **figure 10c** that safely achieve flight. CE apparent efficiency ranged from a low of ~ 0.2 at 4.0 Hz and 100% stimulation to a high of ~ 0.55 at 2.6Hz and 50% stimulation.

1.5 Discussion and Conclusions

1.5.1 Stimulation Frequency Sets Overall MTU Mechanics

We expected that the neural stimulation strategy ‘tuned’ to drive the human triceps-surae MTU at its passive resonant frequency ($\omega_{MTU\ resonance} = 2.1\text{ Hz}$) would maximize MTU force and SEE elastic energy storage and at the same time minimize CE length changes and mechanical power output (i.e. optimal ‘tuning’). In contrast to our expectation, the frequency at which maximal MTU force and SEE energy cycling occurred was 2.2 Hz, slightly higher than the predicted value of 2.1 Hz from hypothesis (1) (**fig. 4**).

Our hypothesis that optimal tuning would occur at 2.1 Hz was based on the fundamental principle from linear systems theory that driving a spring-mass system at its natural frequency would lead to resonant behavior [59]. Lack of optimal ‘tuning’ at 2.1 Hz was due, in large part, to the fact that MTU stiffness was determined by the *both* passive and active tissues (i.e. CE). For example, when considering only passive, linear components (k_{CE} and k_{SEE}) of the spring-mass system the resonant frequency is $\sim 2.1\text{ Hz}$ ($k_{MTU} \sim 60,000\text{ N/m}$). On the other hand, during an isometric contraction when the active component of the CE stiffens and become strut-like, the SEE is left as the only “spring-like” component of the MTU. In this case the resonant frequency would be $\sim 3.8\text{ Hz}$ ($k_{MTU} = k_{SEE} \approx 120,000\text{ N/m}$). Essentially, shifts in the non-linear F-L and F-V dynamics of the CE determined by its active state dynamically change its impedance [60]. This makes it very

difficult to predict the frequency response of muscle-driven systems *a priori* based on system parameters.

1.5.2 Frequency and Phasing: The Role of CE Operating Length

CE length at which stimulation onset occurred was critical in determining both the safety and functional efficacy of MTU mechanics. For nearly all frequencies explored here ($\omega_{stim} > 1.4\text{Hz}$), peak MTU force occurred almost exactly 50% of a stimulation cycle after the MTU reached its minimum length. This phenomena was entirely frequency dependent, and not influenced by changes in stimulation amplitude (**fig. 6b**). In the case of frequencies from 1.6-1.8Hz this phasing was purely the result of passive mechanics, as demonstrated by peak forces *preceding* stimulation onset (**fig. 5, 6**). Under these conditions, muscle was stretched to injurious strains, and activated against a shortening SEE (**fig. 3b**). This not only results in high CE positive power production (**fig. 8b**) and metabolic rates due to rapid CE shortening (**fig. 10a**), but also relatively low SEE positive power production (**fig. 8c**) and MTU efficiency (**fig. 10b**).

This trend starts to reverse with the 2.0 Hz condition. While there is still high risk of injury due to loading of the MTU prior to stimulation onset (**fig. 2a, 3b**), it does occur prior to observed peak forces (**fig. 6**). As stimulation frequency is increased, stimulation onset occurs earlier relative to minimum MTU length (**fig. 6**) and at lower CE strains resulting in reduced injury risk (**fig. 2, 3b**). Stimulation frequencies > 2.0 Hz also facilitate muscle activation on/near the crest of the CE F-L curve during lengthening, resulting in high

total/active CE force production (**figs. 4,5**), low positive power output in the CE (**fig. 8b**), high positive power production from the MTU/SEE (**fig. 8a,c**), reduced metabolic rate (**fig. 10a**) and increased MTU efficiency (**fig. 10b**). These ideal mechanics/energetics are observed for an operational bandwidth of $\sim 2.2\text{-}3.4$ Hz. Above this frequency, the CE is not allowed adequate time to lengthen, and active force production occurs exclusively on the ascending portion of the F-L curve (**fig. 7a**). This results in lower peak forces (**fig. 4**), and an inability to meet task demands for hopping (**fig. 3a**).

In contradiction with hypothesis (2), however, minimal CE work/average positive power output did not occur at $\omega_{MTU\ resonance} = 2.1$ Hz. Rather, minimal/low CE work was observed for stimulation frequencies > 2.4 Hz (**fig. 8b**). Stimulation onset timing in these conditions is such that there is no undue stretch and recoil (i.e. mechanical work) performed by the CE PEE. While stimulation amplitude also plays a role in this phenomena (discussed below), frequency played a critical role in regulating CE operating length at stimulation onset, and was solely responsible for phasing of stimulation onset and peak force (**fig. 6**).

1.5.3 Stimulation Amplitude Adjusts Within MTU Mechanics

In agreement with hypothesis (3), stimulation amplitude controlled MTU force as well as relative contributions of CE vs. SEE to overall power output of the MTU. Stimulation amplitude, in conjunction with frequency, can also modulate operating length of the CE (**fig. 7c**) and therefore active/passive force sharing (**fig. 3b, 5**). In general, higher stimulation amplitude leads to shorter CE operating lengths and thus low or no CE passive

force (**fig. 3b, 5, 7c**). This effect was most pronounced where lack of adequate stimulation forced the CE to shift from ascending portions to the crest of F-L, and even onto the descending limb where the CE PEE could compensate for reduced active CE force production (**fig. 3b, 7c**).

Muscle stimulation amplitude was an effective means of modulating injury risk and the portion of MTU power output that came from elastic energy storage and return versus active muscle shortening. While stimulation amplitude did not significantly affect CE positive power, as indicated by nearly vertical (i.e. frequency dependent) contours (**fig. 8b**); it did have an impact on both MTU and SEE average positive power as indicated by diagonal (i.e. stimulation frequency and amplitude dependent) contours (**fig. 8a,c**). The most notable effect of stimulation amplitude on power output was how it was *shared* between CE and SEE. For example, at a stimulation frequency of 2.2 Hz with an amplitude of 70%, there is high injury risk and 30%-70% power sharing in CE and SEE respectively (**fig. 9d**). By increasing stimulation amplitude to 100%, risk of injury can be eliminated and CE-SEE power sharing is 10%-90% (**fig. 9b**).

1.5.4 Role of Stimulation Frequency and Amplitude on Metabolic Rate and Efficiency

Our hypothesis that (4) metabolic rate and MTU apparent efficiency are maximized at the passive resonant frequency (2.1 Hz) was not supported in its entirety. Metabolic rate was almost entirely dependent on stimulation amplitude, as indicated by horizontal contours in

figure 10a. This is somewhat unexpected given that our metabolic cost model also possessed a strong velocity dependence; but is consistent with the observation that varying frequency in the range of 2.2-3.0 Hz does very little to influence the average operating velocity of the CE during active force production (**fig. 7b**).

By modulating stimulation frequency in a compliant MTU, it is possible to achieve a constant metabolic “rate of return” (e.g. MTU apparent efficiency) regardless of amplitude (**fig. 10b**). Stimulation amplitude primarily governed power sharing between CE and SEE (**fig. 5, 9**). Its role was to regulate the tradeoff between high force production with significant SEE energy storage and return (**fig. 4, 8c**), or force compensation via CE PEE recoil resulting in lower metabolic demand (**fig. 10a**), greater CE efficiency (**fig. 10c**), and increased risk of injury (**fig. 3b**). The combination of these factors resulted in peak MTU apparent efficiency at a stimulation frequency of 2.2 Hz (**fig. 10b**), and peak CE apparent efficiency occurring for stimulation amplitudes that operate with strains on the cusp of injury at all frequencies between 2.2-3.2 Hz (**fig. 3b, 10c**). Above this frequency band increased stimulation amplitude is required to achieve a flight phase, resulting in reduced muscle strains/CE PEE utilization (**fig. 3b**), increased metabolic rate (**fig. 10a**), and ultimately reduced CE apparent efficiency (**fig. 10c**).

1.5.5 Minimizing metabolic cost while avoiding muscle injury- A trade-off criterion that drives movement preference?

Trying to determine what, if any, mechanical and energetic criteria humans seek to optimize in bouncing gait is a daunting task. Lower frequencies of movement (i.e. 2.2-2.4 Hz) require high mechanical power output (**fig. 8a**) and stimulation amplitude/metabolic rate (**fig. 10a**), but also most effectively utilize series elastic tissues (**fig. 8c**) and have the greatest apparent efficiency of movement (**fig. 10b**). Intermediate frequencies of movement (i.e. 2.6-3.0 Hz) require the lowest stimulation amplitudes to safely hop (**fig. 3b**) reducing overall metabolic demand (**fig. 10a**) and increasing CE apparent efficiency (**fig. 10c**). These benefits, however, come at the cost of increased CE PEE strains and injury risk (**fig. 3b**), reduced contributions from the SEE (**fig. 8c**), and decreased MTU apparent efficiency (**fig. 10b**). High frequencies of movement (e.g. > 3.2 Hz) force the CE onto its ascending limb (**fig. 3b**), reducing its capacity to actively produce force. These high frequencies of movement also necessitate greater rates of force to achieve hopping, ultimately requiring higher stimulation amplitudes and increased metabolic rates (**fig. 3a, 10a**).

While there are conflicting trends in metabolic cost for human hopping, the spectrum of experimental outcomes can be observed in our modeled data depending on how parameter space is traversed. Based on Farris et. al., one would expect rises in metabolic beyond operating frequencies of ~ 2.8 Hz [33]. Based on trends from Gutmann et. al. and Grabowski et. al., however, it would be expected that metabolic rate would continue to decline as

stimulation frequency is increased [61,62]. In our modeled data, the range of stimulation frequency/amplitude combinations that facilitate hopping are limited by injury risk and the ability to achieve an aerial phase. Using 2.2 Hz and 100% stimulation amplitude as a starting point, our model predicts that it is possible to safely and effectively trade lower stimulation amplitude for increasing stimulation frequency until ~2.8-3.2 Hz (**fig. 3**). This would result in reduced metabolic rate, a direct correlate with stimulation amplitude (**fig. 10a**). It can also be seen that, as frequency is increased, it becomes necessary to also increase stimulation amplitude to achieve an aerial phase for stimulation frequencies > 3.2 Hz (the highest frequency condition from Farris et. al. and Guttman et. al. [33,61]) (**fig. 3a**). It is not possible to predict human preference based on our model, but if people employ a strategy to minimize activation while avoiding injury risk during frequency constrained hopping, experimentally observed trends in metabolic rate mesh well with those predicted here.

1.6 Future Directions

Despite its inherent simplicity, the model presented here provides ample insight into the role of neural control in shaping compliant MTU mechanics and energetics. Emergent behaviors from this model that correspond remarkably well to observed human mechanics include ground reaction force (i.e. MTU force) profiles [33,35,46,61-63], near isometry in the CE [45], effective SEE energy cycling [45], and frequency dependent minimums in metabolic cost [33,61,62]. This baseline model is meant to serve the backbone for an *in silico* testbed to optimize assistive exoskeleton technologies

designed to improve human performance in bouncing gaits. Thus, in future research we will extend the current model to (1) explore the influence that parallel assistive devices (e.g. elastic exoskeletons) have on compliant MTU mechanics and energetics during steady cyclic movements and (2) assess the interplay between MTU morphology and afferent feedback pathways during perturbed movements with and without assistive devices.

1.7 Tables

Table 1, Model Parameters: Parameter values used in model implementation.
*indicates half body mass.

Muscle Parameters (CE)	Value
F_{max}	6000 N [3, 7, 19]
v_{max}	-0.45 m/s [3, 7]
l_0	0.055 m [6, 7, 48]
k_m	90,000 N/m [6]
Tendon Parameters (SEE)	Value
l_{slack}	.237 m [6, 7]
k_t	180,000 N/m [6]
Activation Parameters	Value
τ_{act}	0.011 s [49, 50]
τ_{deact}	0.068 s [49, 50]
Pulse Duty	10.0%
Environment Dynamics	Value
g	9.8 m/s ²
$EMA (l_{in}/l_{out})$	0.33 [7]
m	35 kg*

Table 2, Model Equations: Equations and parameter values used in model implementation

Muscle Force Length	Equation	Values
$F_l \text{ active}$	$e^{- (l_m/l_0)^b - 1 /s ^a}$ [34, 35]	$b = .8698, s = .3914, a = 3.1108$
$F_l \text{ passive}$	$A * e^{(b*(l_m/l_0)-1)}$ [34, 36]	$A = 2.38 * 10^{-2}, b = 5.31$
Muscle Force Velocity	Equation	Values
$F_v \text{ when } v_m > 0$	$(1 - (v_{CE}/v_{max})) / (1 + (v_{CE}/(k * v_{max})))$ [14, 38]	$k = .17$
$F_v \text{ when } v_m < 0$	$1.8 - 0.8 * ((1 + v_{CE}/v_{max}) / (1 - 7.56 * (v_{CE}/(k * v_{max}))))$ [14, 38]	$k = .17$
Tendon Stiffness	Equation	Values
k_{SEE}	$k_t * (1 + (0.9 / -e^{((Q * F_{CE}) / F_{max})}))$ [6]	$Q = 20$
Activation Dynamics	Equation	Values
$\alpha(t)$	$\int [(u(t)/\tau_{act}) - (1/\tau_{act}) * (\beta + (1 - \beta) * u(t))] dt$ [39]	$\beta = \tau_{act} / \tau_{deact}$

1.8 Figures

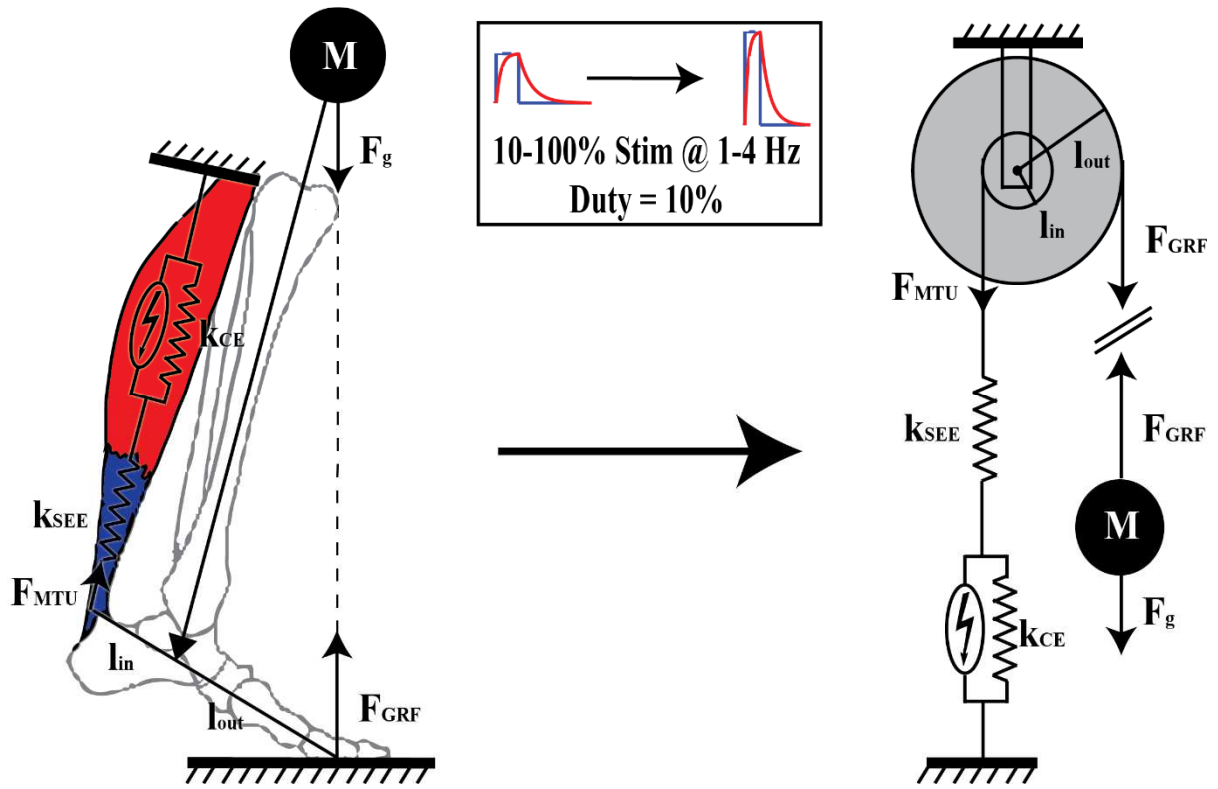


Figure 1, Model Schematic: Physiological basis for (left), and mechanical schematic of (right), lumped triceps surae-Achilles tendon group interacting with mass in gravity. Parameter space traversed is indicated in the box between the two schematics, with red arrows indicating control parameter point of action in active components of the modeled MTU. System parameters and equations can be seen in **table 1** and **2** respectively.

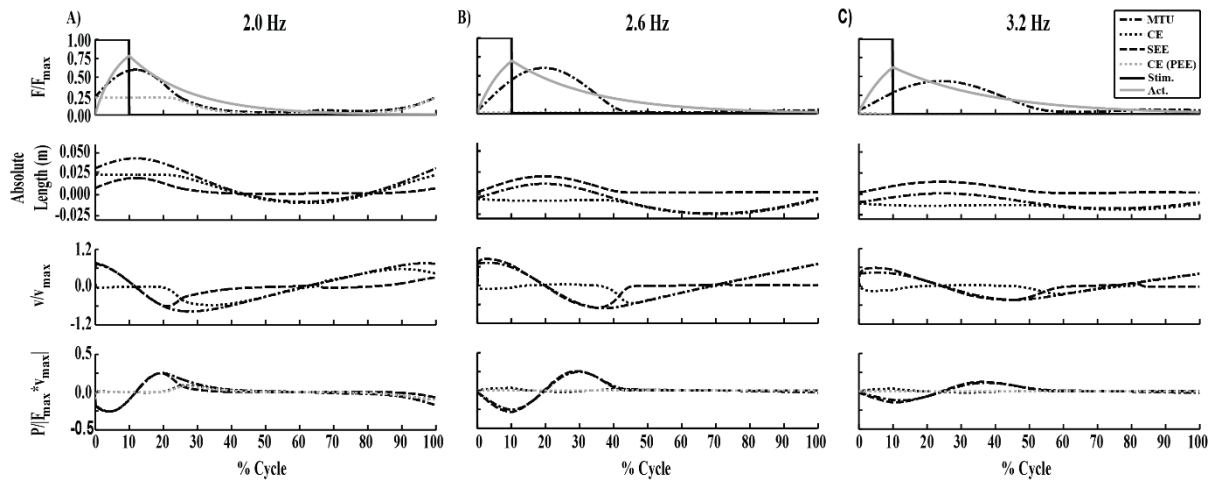
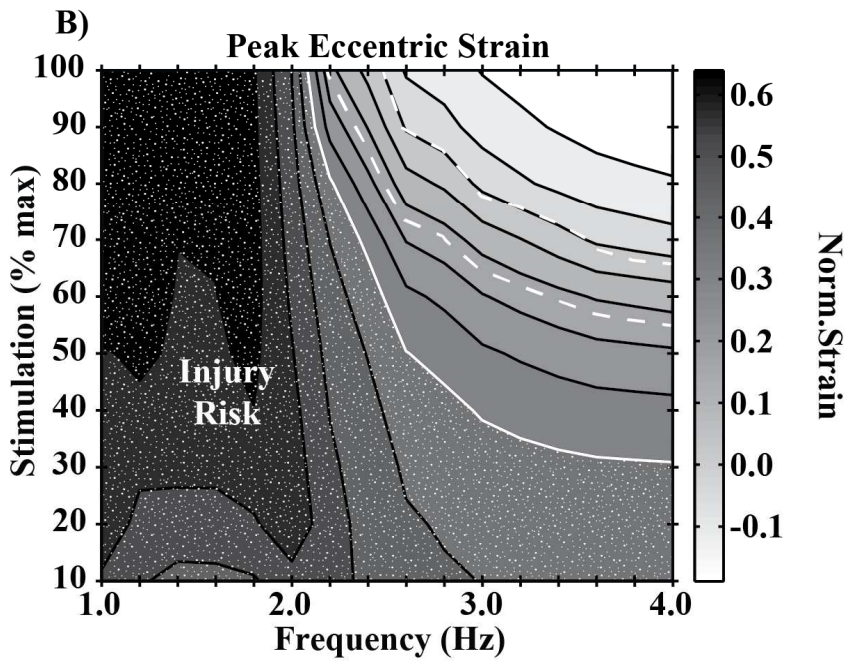
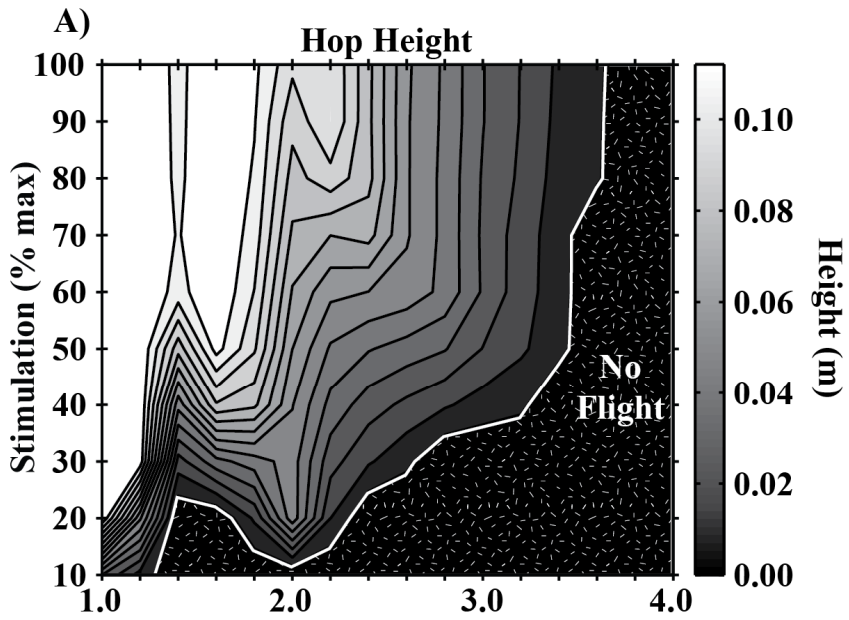


Figure 2, Cycle Dynamics: Periodic data for 100% stimulation amplitude condition at frequencies of **A)** 2.0 Hz, **B)** 2.6 Hz, and **C)** 3.2 Hz. Each data set contains normalized stimulation/activation and force dynamics (top, F/F_{max}), absolute length (first from top, $l_{CE}^{abs} = l_{CE} - l_0$, $l_{SEE}^{abs} = l_{SEE} - l_{slack}$, $l_{MTU}^{abs} = l_{MTU} - (l_0 + l_{slack})$), normalized velocity (second from top, v/v_{max}), and normalized power (bottom, $P/|F_{max} * v_{max}|$) (**table 1**). Each data set is plotted for a single period of stimulation relative to stimulation onset (0% of Cycle). Note well defined regions of high force production (“stance”), and regions where $F/F_{max} = 0$ (“flight”) at every stimulation frequency.

Figure 3, Hop Height and Injury Risk: **A)** Hop height (contours) vs. frequency (x-axis) and amplitude (y-axis) of stimulation. Conditions which did not achieve flight are indicated by a white border and hatched region labeled “No Flight.” These primarily include high stimulation frequency and low stimulation amplitude regions of parameter space. **B)** Normalized peak eccentric CE strain (contours) vs. stimulation frequency (x-axis) and amplitude (y-axis). Regions of high injury risk are indicated by a white border and speckled region labeled “injury risk”, and generally occur at frequencies ≤ 2.0 Hz. The Region outlined by the white dashed line indicates an average operating strain of $\pm 1.05l_0$ during active force production.



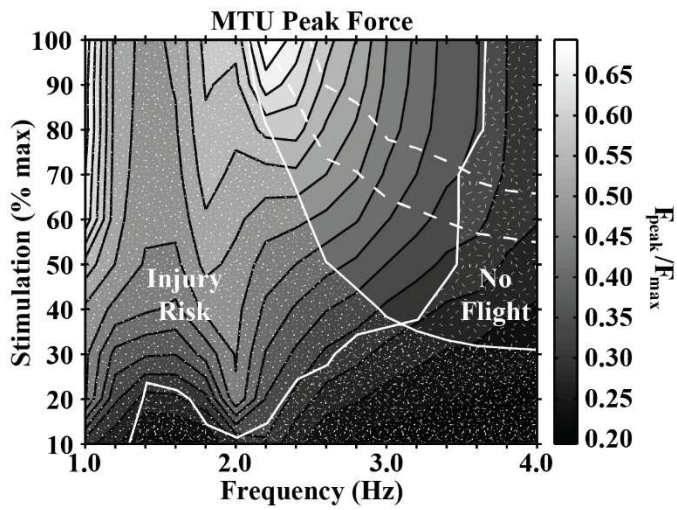


Figure 4, Peak Force: Normalized peak MTU force (F_{peak}/F_{max}) (contours) vs. stimulation frequency (x-axis) and amplitude (y-axis). Peak forces observed that achieve flight without posing injury risk were at 2.2 Hz and maximal (100%) stimulation. Dropping stimulation amplitude or raising/lowering frequency from this point resulted in reduced peak forces.

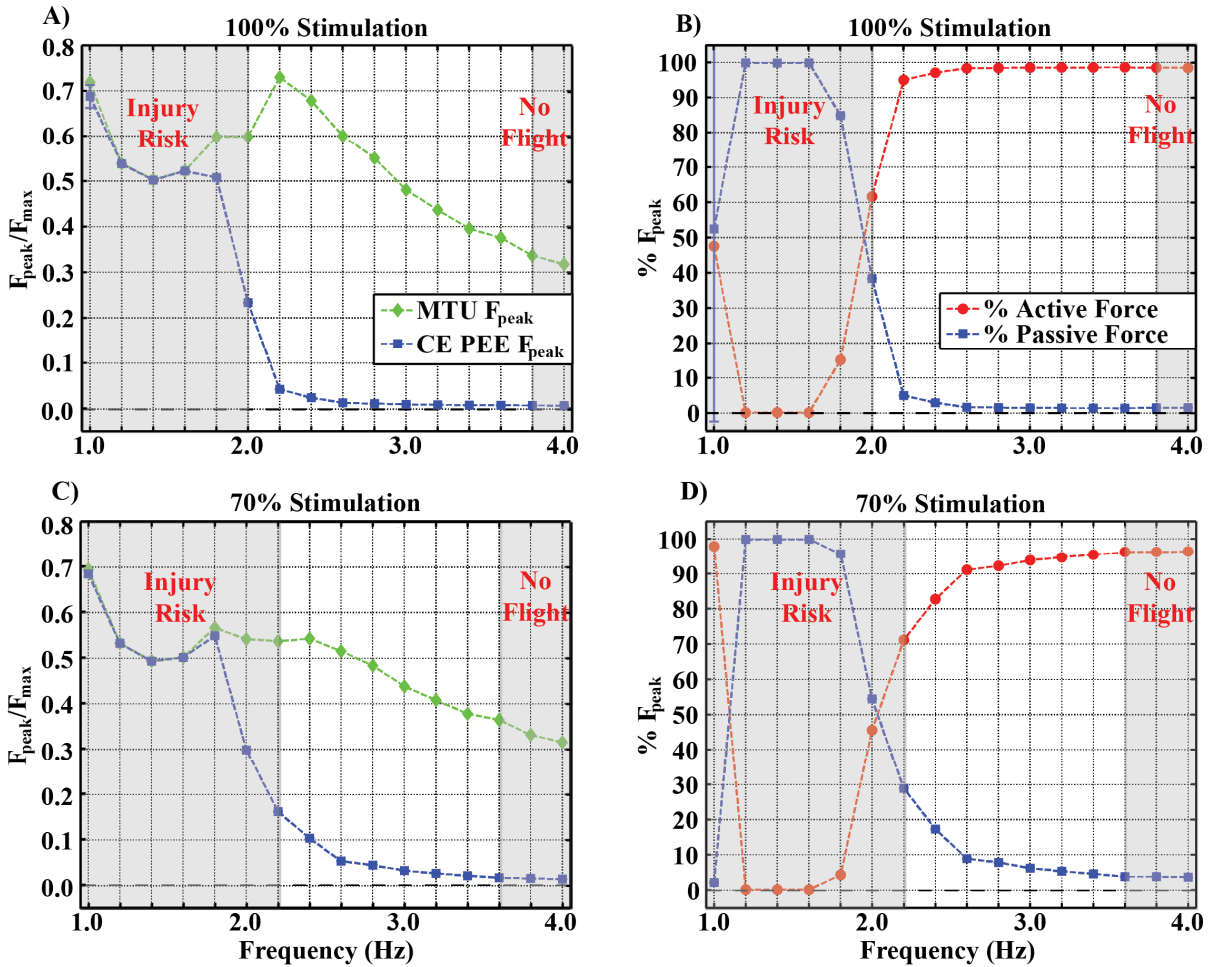


Figure 5, Force Sharing: Contour slice of MTU and passive CE peak force, as well as their % contribution to total force, for stimulation amplitudes of 100% (A and B respectively) and 70% (C and D respectively). Conditions that pose excessive risk of injury or do not achieve a flight phase are indicated by opaque gray regions. Note that both higher frequencies and amplitudes of stimulation have less dependence on passive CE force generation.

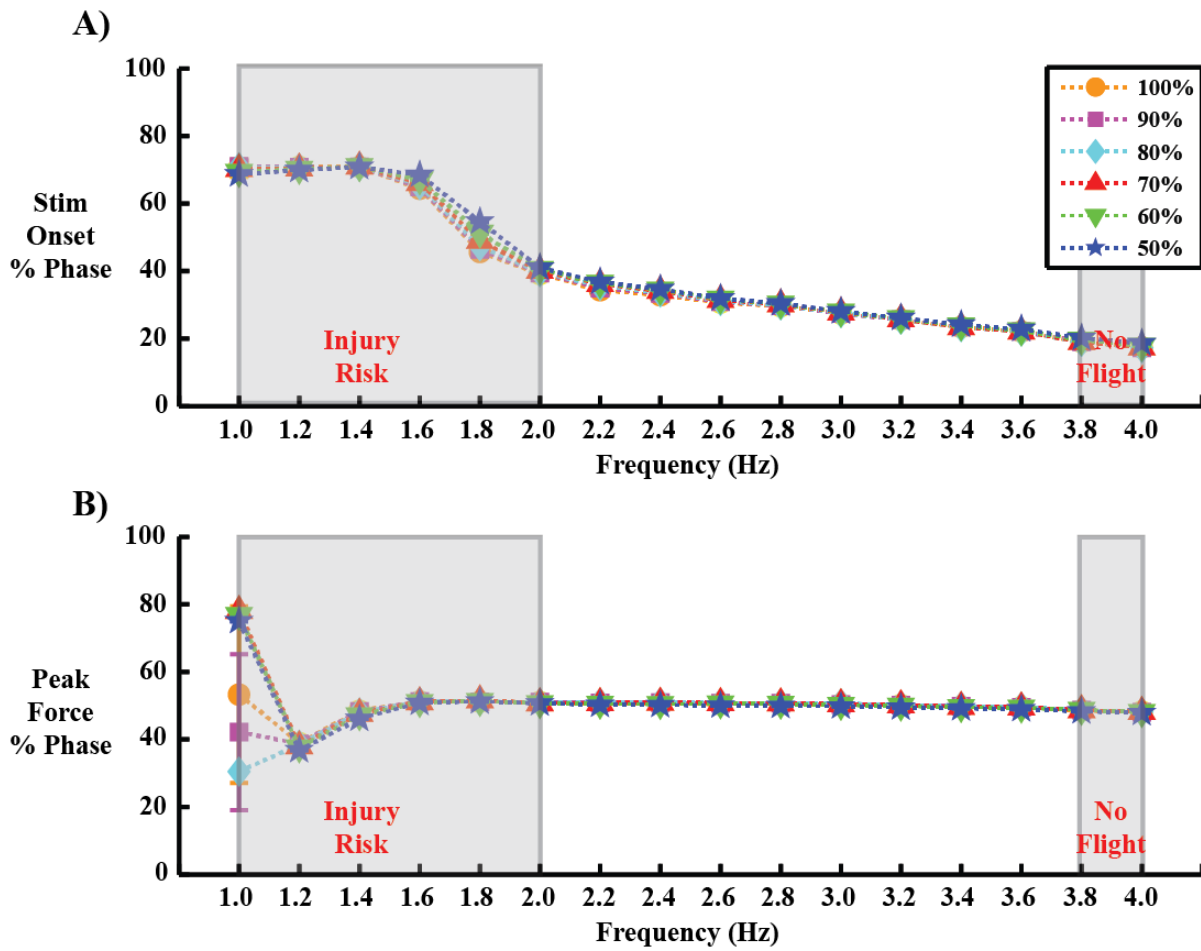


Figure 6, Stimulation and Force Phasing: Phasing of stimulation onset (A) and peak force (B) relative to minimum MTU length at all frequencies of stimulation for amplitudes ranging from 50-100% of maximum. Conditions with elevated injury risk and no flight phase for the 100% stimulation amplitude condition are indicated by opaque gray regions. Note that, for frequencies > 1.4 Hz, stimulation onset occurs earlier relative to minimum MTU length as frequency is increased, while peak force phasing remains constant.

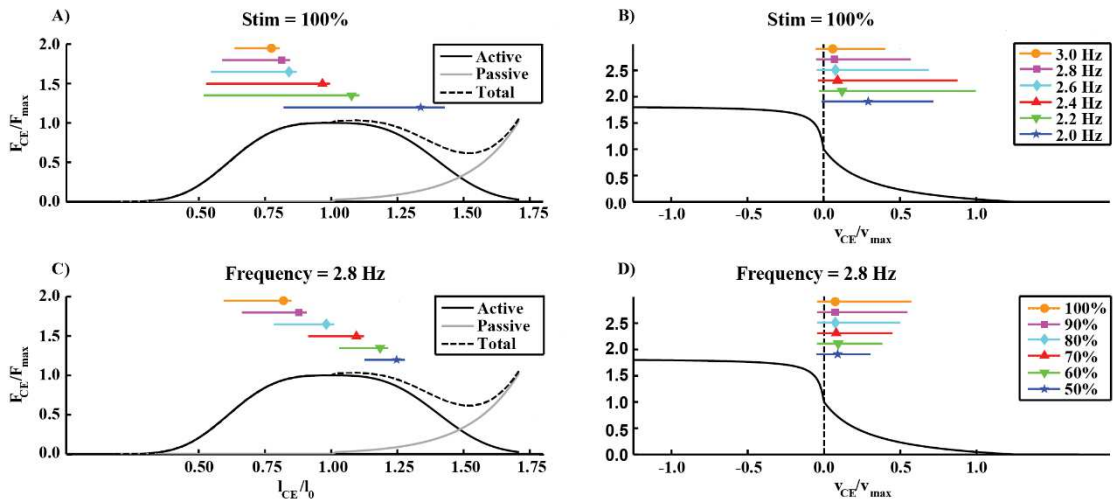
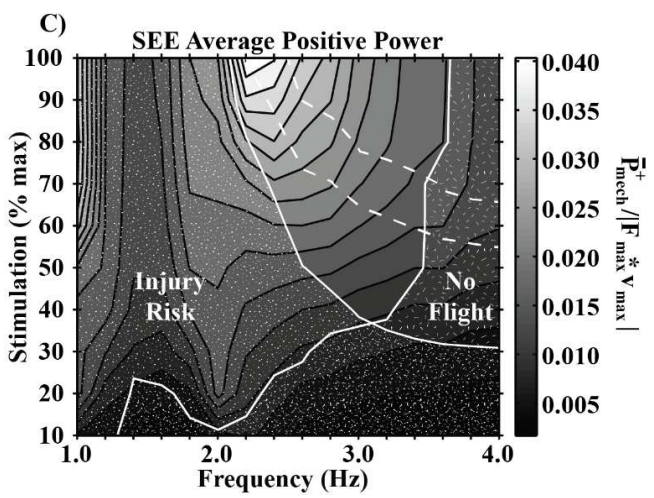
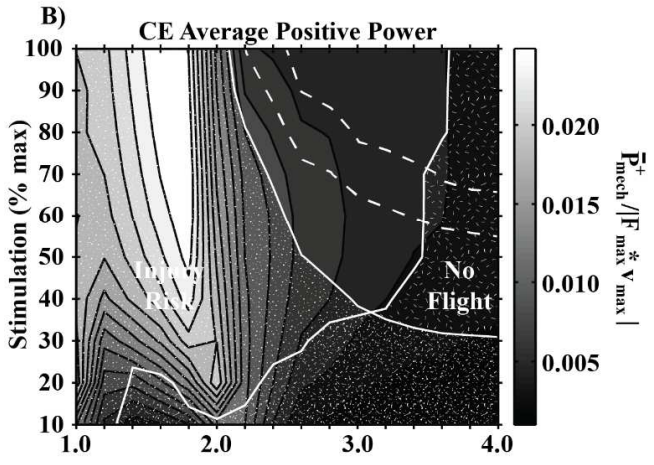
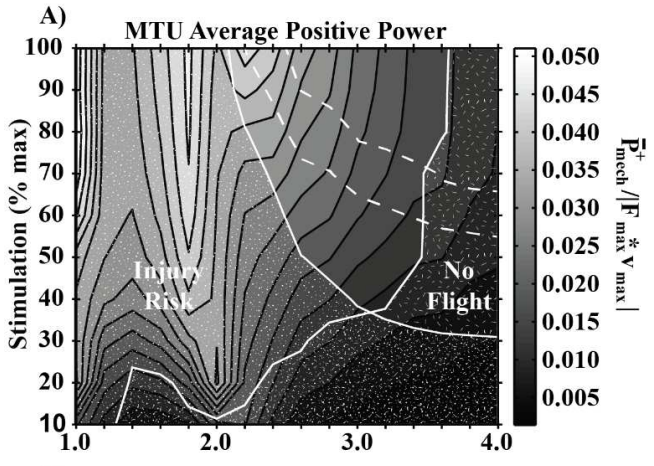


Figure 7, Muscle Operating Point: Normalized CE force-length (F-L) and velocity (F-V) operating point for a range of frequencies at maximum stimulation amplitude (**A** and **C** respectively) and a range of stimulation amplitudes at 2.8 Hz (**B** and **D** respectively). The range of F-L and F-V operating conditions during active force production is indicated by color-coded bars, and the average operating point is indicated by a marker placed over each bar. Note that both frequency and magnitude of stimulation modulate force-length operating point (**A** and **B**), while there is little effect of either parameter on average operating velocity for frequencies > 2.0 Hz (**C** and **D**).

Figure 8, Average Power Output: Average positive power produced in the MTU (A), CE (B), and SEE (C) (contours) for all stimulation frequency (x-axis) and amplitude (y-axis) combinations. All values are normalized to $|F_{max} * v_{max}|$ (table 1). Note that MTU average positive power generally trends with frequency (i.e. nearly vertical contours) (A), CE positive power is relatively constant (B), and SEE power is has both frequency and amplitude dependence (i.e. diagonal contours)(C) in regions where



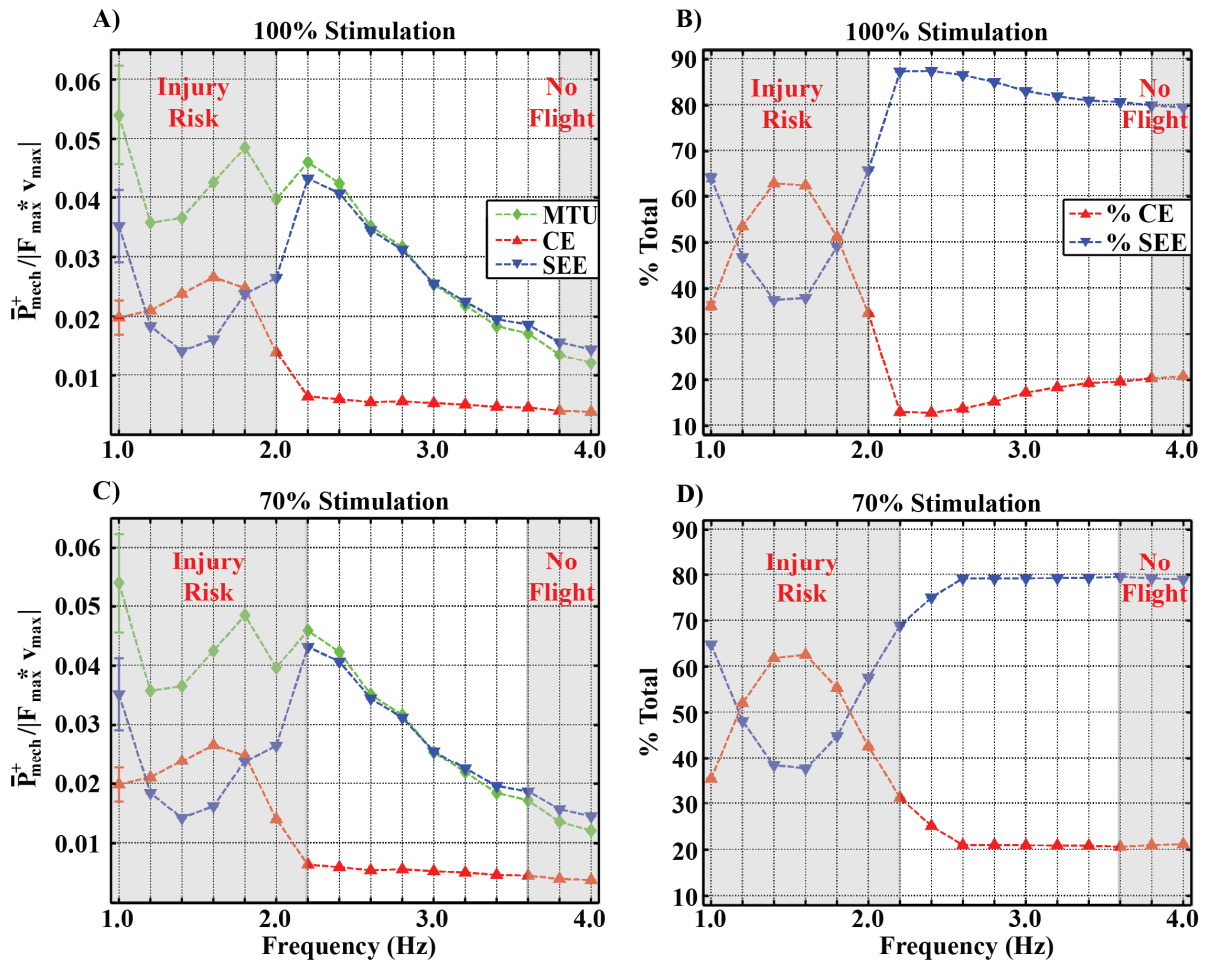
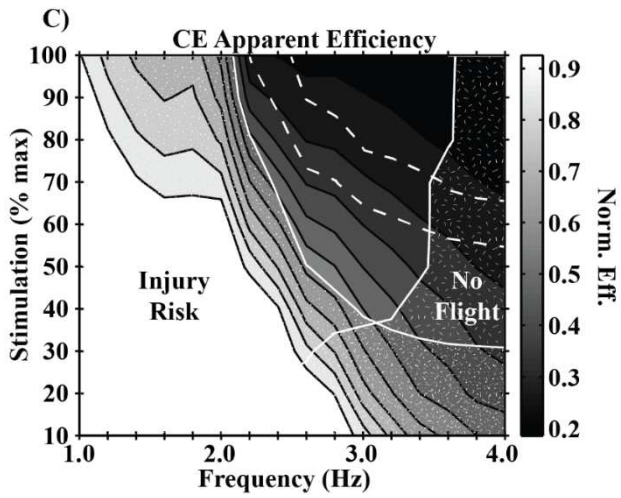
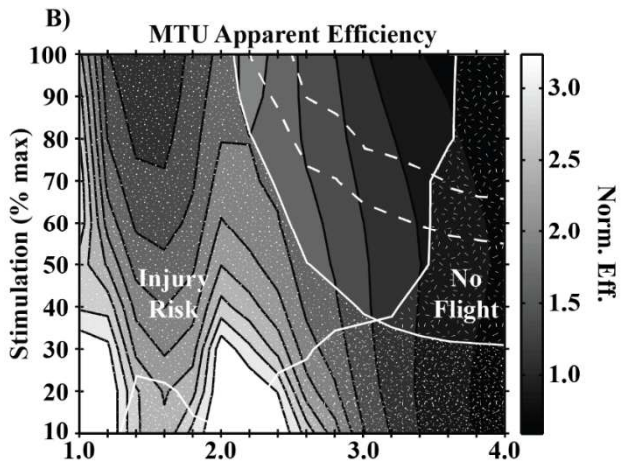
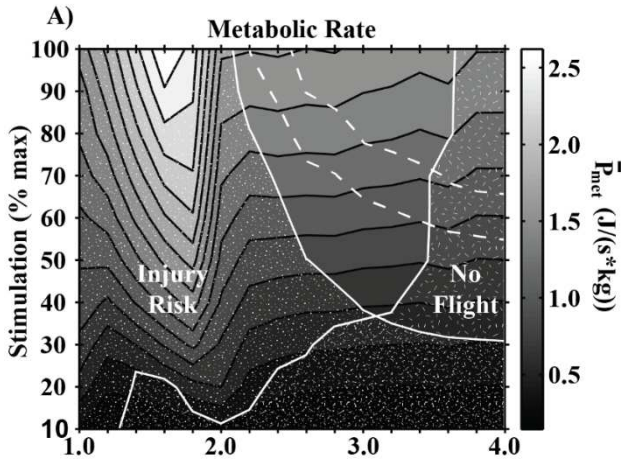


Figure 9, Average Power Sharing: Power sharing. Normalized average positive power produced by MTU, CE, and SEE, as well as % contributions from CE and SEE at all stimulation frequencies for amplitudes of 100% (A and B respectively) and 70% (C and D respectively). Regions of high injury risk and no flight are indicated by opaque gray areas. Note that the majority of positive power comes from the SEE for stimulation frequencies > 1.8 Hz for both stimulation amplitudes.

Figure 10, Metabolic Rate and Apparent Efficiency: Average metabolic rate ($J/(s \cdot kg)$) (**A**), and apparent efficiency (P_{mech}^+/P_{met}) of the MTU (**B**) and CE (**C**) (contours) versus stimulation frequency (x-axis) and amplitude (y-axis). Conditions with high risk of injury (speckled) or no flight (hatched) are filled and bordered in white. Note that metabolic rate was entirely stimulation amplitude dependent (i.e. horizontal contours) (**A**), MTU apparent efficiency was entirely frequency dependent (i.e. vertical contours) (**B**), and CE apparent efficiency is dependent on both (i.e. diagonal contours) (**C**) in regions where hopping is safely



References

1. Geyer H, Seyfarth A, Blickhan R (2006) Compliant leg behaviour explains basic dynamics of walking and running. *Proc Biol Sci* 273: 2861-2867.
2. Alexander RM (2002) Tendon elasticity and muscle function. *Comp Biochem Physiol A Mol Integr Physiol* 133: 1001-1011.
3. Hof AL, Van Zandwijk JP, Bobbert MF (2002) Mechanics of human triceps surae muscle in walking, running and jumping. *Acta Physiol Scand* 174: 17-30.
4. Ishikawa M, Komi PV, Grey MJ, Lepola V, Bruggemann GP (2005) Muscle-tendon interaction and elastic energy usage in human walking. *J Appl Physiol* 99: 603-608.
5. Lichtwark GA, Bougoulias K, Wilson AM (2007) Muscle fascicle and series elastic element length changes along the length of the human gastrocnemius during walking and running. *J Biomech* 40: 157-164.
6. Lichtwark GA, Wilson AM (2008) Optimal muscle fascicle length and tendon stiffness for maximising gastrocnemius efficiency during human walking and running. *J Theor Biol* 252: 662-673.
7. Lichtwark GA, Wilson AM (2007) Is Achilles tendon compliance optimised for maximum muscle efficiency during locomotion? *Journal of Biomechanics* 40: 1768-1775.
8. van der Krogt MM, de Graaf WW, Farley CT, Moritz CT, Richard Casius LJ, et al. (2009) Robust passive dynamics of the musculoskeletal system compensate for unexpected surface changes during human hopping. *J Appl Physiol* 107: 801-808.
9. Takeshita D, Shibayama A, Muraoka T, Muramatsu T, Nagano A, et al. (2006) Resonance in the human medial gastrocnemius muscle during cyclic ankle bending exercise. *J Appl Physiol* 101: 111-118.

10. Holt KG, Hamill J, Andres RO (1990) The Force-Driven Harmonic-Oscillator as a Model for Human Locomotion. *Human Movement Science* 9: 55-68.
11. Srinivasan M, Holmes P (2008) How well can spring-mass-like telescoping leg models fit multi-pedal sagittal-plane locomotion data? *J Theor Biol* 255: 1-7.
12. Blickhan R (1989) The spring-mass model for running and hopping. *J Biomech* 22: 1217-1227.
13. Farley CT, Morgenroth DC (1999) Leg stiffness primarily depends on ankle stiffness during human hopping. *J Biomech* 32: 267-273.
14. Haeufle DF, Grimmer S, Seyfarth A (2010) The role of intrinsic muscle properties for stable hopping--stability is achieved by the force-velocity relation. *Bioinspir Biomim* 5: 16004.
15. Haeufle DF, Grimmer S, Kalveram KT, Seyfarth A (2012) Integration of intrinsic muscle properties, feed-forward and feedback signals for generating and stabilizing hopping. *J R Soc Interface*.
16. Alexander RM (1997) Optimum Muscle Design for Oscillatory Movements. *Journal of Theoretical Biology* 184: 253-259.
17. Roberts TJ (2002) The integrated function of muscles and tendons during locomotion. *Comp Biochem Physiol A Mol Integr Physiol* 133: 1087-1099.
18. Srinivasan M (2011) Fifteen observations on the structure of energy-minimizing gaits in many simple biped models. *J R Soc Interface* 8: 74-98.
19. Krishnaswamy P, Brown EN, Herr HM (2011) Human leg model predicts ankle muscle-tendon morphology, state, roles and energetics in walking. *PLoS Comput Biol* 7: e1001107.

20. Arnold EM, Delp SL (2011) Fibre operating lengths of human lower limb muscles during walking. *Philos Trans R Soc Lond B Biol Sci* 366: 1530-1539.
21. Bobbert MF, Huijing PA, van Ingen Schenau GJ (1986) A model of the human triceps surae muscle-tendon complex applied to jumping. *J Biomech* 19: 887-898.
22. Neptune RR, McGowan CP (2011) Muscle contributions to whole-body sagittal plane angular momentum during walking. *J Biomech* 44: 6-12.
23. Neptune RR, McGowan CP, Kautz SA (2009) Forward dynamics simulations provide insight into muscle mechanical work during human locomotion. *Exerc Sport Sci Rev* 37: 203-210.
24. Umberger BR, Rubenson J (2011) Understanding muscle energetics in locomotion: new modeling and experimental approaches. *Exerc Sport Sci Rev* 39: 59-67.
25. Arnold EM, Hamner SR, Seth A, Millard M, Delp SL (2013) How muscle fiber lengths and velocities affect muscle force generation as humans walk and run at different speeds. *J Exp Biol* 216: 2150-2160.
26. Umberger BR, Gerritsen KG, Martin PE (2003) A model of human muscle energy expenditure. *Comput Methods Biomech Biomed Engin* 6: 99-111.
27. Ackermann M, van den Bogert AJ (2010) Optimality principles for model-based prediction of human gait. *J Biomech* 43: 1055-1060.
28. Carrier DR, Anders C, Schilling N (2011) The musculoskeletal system of humans is not tuned to maximize the economy of locomotion. *Proceedings of the National Academy of Sciences of the United States of America* 108: 18631-18636.
29. Monsch ED, Franz CO, Dean JC (2012) The effects of gait strategy on metabolic rate and indicators of stability during downhill walking. *Journal of biomechanics* 45: 1928-1933.

30. Snyder KL, Farley CT (2011) Energetically optimal stride frequency in running: the effects of incline and decline. *J Exp Biol* 214: 2089-2095.
31. Dean JC, Kuo AD (2011) Energetic costs of producing muscle work and force in a cyclical human bouncing task. *J Appl Physiol* 110: 873-880.
32. Raburn CE, Merritt KJ, Dean JC (2011) Preferred movement patterns during a simple bouncing task. *J Exp Biol* 214: 3768-3774.
33. Farris DJ, Sawicki GS (2012) Linking the mechanics and energetics of hopping with elastic ankle exoskeletons. *J Appl Physiol* 113: 1862-1872.
34. Minetti AE, Alexander RM (1997) A theory of metabolic costs for bipedal gaits. *J Theor Biol* 186: 467-476.
35. Farley CT, Blickhan R, Saito J, Taylor CR (1991) Hopping frequency in humans: a test of how springs set stride frequency in bouncing gaits. *J Appl Physiol* 71: 2127-2132.
36. Azizi E, Brainerd EL, Roberts TJ (2008) Variable gearing in pennate muscles. *Proc Natl Acad Sci U S A* 105: 1745-1750.
37. Carrier DR, Heglund NC, Earls KD (1994) Variable gearing during locomotion in the human musculoskeletal system. *Science* 265: 651-653.
38. Biewener AA, Farley CT, Roberts TJ, Temaner M (2004) Muscle mechanical advantage of human walking and running: implications for energy cost. *J Appl Physiol* 97: 2266-2274.
39. Maykranz D, Grimmer S, Seyfarth A (2013) A work-loop method for characterizing leg function during sagittal plane movements. *Journal of applied biomechanics* 29: 616-621.

40. Azizi E, Roberts TJ (2010) Muscle performance during frog jumping: influence of elasticity on muscle operating lengths. *Proc Biol Sci* 277: 1523-1530.
41. Otten E (1987) A myocybernetic model of the jaw system of the rat. *J Neurosci Methods* 21: 287-302.
42. Fung YC (1967) Elasticity of soft tissues in simple elongation. *Am J Physiol* 213: 1532-1544.
43. Rubenson J, Pires NJ, Loi HO, Pinniger GJ, Shannon DG (2012) On the ascent: the soleus operating length is conserved to the ascending limb of the force-length curve across gait mechanics in humans. *J Exp Biol*.
44. Hill AV (1938) The heat of shortening and the dynamic constants of muscle. *Proceedings of the Royal Society of London Series B-Biological Sciences* 126: 136-195.
45. Farris DJ, Robertson BD, Sawicki GS (2013) Passive elastic exoskeletons reduce soleus muscle force but not work in human hopping. *J Appl Phys*.
46. Ferris DP, Bohra ZA, Lukos JR, Kinnaird CR (2006) Neuromechanical adaptation to hopping with an elastic ankle-foot orthosis. *J Appl Physiol* 100: 163-170.
47. Zajac FE (1989) Muscle and tendon: properties, models, scaling, and application to biomechanics and motor control. *Crit Rev Biomed Eng* 17: 359-411.
48. Winters JM, Stark L (1988) Estimated mechanical properties of synergistic muscles involved in movements of a variety of human joints. *J Biomech* 21: 1027-1041.
49. Raasch CC, Zajac FE, Ma B, Levine WS (1997) Muscle coordination of maximum-speed pedaling. *J Biomech* 30: 595-602.

50. Fukunaga T, Roy RR, Shellock FG, Hodgson JA, Day MK, et al. (1992) Physiological cross-sectional area of human leg muscles based on magnetic resonance imaging. *J Orthop Res* 10: 928-934.
51. Lieber RL, Friden J (1993) Muscle damage is not a function of muscle force but active muscle strain. *J Appl Physiol* 74: 520-526.
52. Lieber RL, Leonard ME, Brown CG, Trestik CL (1991) Frog semitendinosus tendon load-strain and stress-strain properties during passive loading. *Am J Physiol* 261: C86-92.
53. Lieber RL, Woodburn TM, Friden J (1991) Muscle damage induced by eccentric contractions of 25% strain. *J Appl Physiol* 70: 2498-2507.
54. Brooks SV, Zerba E, Faulkner JA (1995) Injury to muscle fibres after single stretches of passive and maximally stimulated muscles in mice. *J Physiol* 488 (Pt 2): 459-469.
55. Morgan DL, Allen DG (1999) Early events in stretch-induced muscle damage. *J Appl Physiol* 87: 2007-2015.
56. Doke J, Kuo AD (2007) Energetic cost of producing cyclic muscle force, rather than work, to swing the human leg. *J Exp Biol* 210: 2390-2398.
57. Ma SP, Zahalak GI (1991) A distribution-moment model of energetics in skeletal muscle. *J Biomech* 24: 21-35.
58. Sawicki GS, Ferris DP (2008) Mechanics and energetics of level walking with powered ankle exoskeletons. *Journal of Experimental Biology* 211: 1402-1413.
59. Ogata K (2003) *System Dynamics*. Upper Saddle River, NJ: Prentice Hall.
60. Farahat WA, Herr HM (2010) Optimal workloop energetics of muscle-actuated systems: an impedance matching view. *PLoS Comput Biol* 6: e1000795.

61. Gutmann AK (2011) Human hopping: A model for understanding the mechanics and energetics of bouncing gaits. Calgary: University of Calgary.
62. Grabowski AM, Herr HM (2009) Leg exoskeleton reduces the metabolic cost of human hopping. *J Appl Physiol* 107: 670-678.
63. Chang YH, Roiz RA, Auyang AG (2008) Intralimb compensation strategy depends on the nature of joint perturbation in human hopping. *J Biomech* 41: 1832-1839.

CHAPTER 2: FREQUENCY-PHASE COUPLING IN CYCLICALLY DRIVEN BIOLOGICAL MUSCLE-TENDONS

2.1 Abstract

We present a bio-robotic platform that allowed us to systematically investigate the link between ‘form’, or configuration of muscle, tendon, moment arms, and inertial load, to ‘function’ in propulsive movement. A simulated mechanical/inertial system was coupled to a biological muscle-tendon unit (MTU) through a feedback controlled ergometer. This bio-robotic system was allowed to oscillate in the absence of muscle activation to determine its natural frequency of movement (ω_0). Next, the biological MTU was driven via direct nerve stimulation across a range of frequencies centered on ω_0 . Despite the fact that interaction with our simulated inertial system was not constrained in any way, steady state cyclic behavior was observed at all driving frequencies explored here. We found that, for a driving frequency of ω_0 , peak MTU force was maximized, the ratio of CE to MTU positive work was minimized, estimated metabolic cost was minimized, and apparent MTU efficiency was maximized relative to all other conditions. This is in agreement with previous studies of resonant ankle joint mechanics in humans. In our study, these beneficial outcomes were the result of emergent driving frequency-stimulation phasing dynamics beneficial to high active force production in muscle, and subsequent energy storage and return in series tendon. This study demonstrated that high level active control is not necessary for ‘tuned’ muscle tendon interactions if frequency of movement matches ω_0 of the passive biomechanical system.

2.2 Introduction

Elastic limb behavior is a hallmark of terrestrial locomotion and the mechanics can be described by the physics of spring-mass interaction [1-4]. Simple models that treat the entire leg as a spring loaded inverted pendulum (SLIP), and the body as a point mass can predict the mechanics of hopping [3], walking [4], and running [1,4], as well as the importance of more subtle features of stable gait such as response to perturbations [5,6]. With these insights in mind, the focus shifts to the links between form and function; and the role neural control plays in modulating the dynamic interaction between muscle-tendon architecture/limb morphology (i.e. form) and the environment that ultimately gives rise to cyclic locomotion (i.e. function).

Recent advances in functional imaging and instrumentation, combined with clever experimental design, have provided some insight into the role that muscle-tendon architecture (i.e. form) plays in observed elastic limb behavior (i.e. function). Perhaps due to the obvious compliance in the Achilles' tendon [7], much previous research has targeted the ankle plantarflexors as a potential source of overall limb elastic behavior [8-11]. Studies on mechanically simple behaviors (e.g. vertical hopping) that preserve the salient features of more dynamic gaits like running and walking, but minimize involvement of more proximal joints (i.e. knee and hip) have demonstrated that muscle-tendon interaction at the distal joints of the lower-limb (e.g. ankle) can be 'tuned' to cycle large amounts of energy in series elastic structures such as tendon and aponeurosis [12-14]. This not only results in spring-like joint and center of mass-level mechanics [3], but can also amplify the mechanical power output and improve the efficiency of muscle-tendon unit mechanical work beyond what would be possible for muscle alone [15-22].

Studies on isolated muscles using classical work-loop based approaches have provided a window into the influence of neural control on muscle function during cyclic contractions as might be observed during steady locomotion [23,24]. For example, this approach has been of great utility for understanding the role that frequency and phase of muscle activation play in governing elastic energy storage and return in series elastic tissues (i.e. tendon and aponeurosis) . In these experiments, cyclic limb/joint trajectories comparable to those observed in natural gait are imposed by an ergometer, and the timing of muscle activation onset is varied in a controlled manner with respect to the phase of the movement cycle [15,18,25-27].

‘Real-world’ movement kinematics are not constrained. Instead, cyclic patterns of muscle-tendon strain are the result of the dynamic interaction between biological actuators (i.e. the muscle-tendons), limb/joint architecture (i.e. the transmission), and inertial-gravitational load (i.e. the environment). Thus, due to the intricate dynamic coupling between form and function in the ‘real world’, it is difficult to gain detailed insight into how elastic limb behavior emerges under the tight kinematic constraints imposed by the classical work-loop approach [28]. Instead, we need an approach that is fully unconstrained, except for by the intrinsic properties of the muscles, the transmission and the environment themselves. Movement in our experiments should mirror terrestrial locomotion in the ‘real –world’, arising naturally as a result of the dynamic interaction between actively driven muscle-tendon units (MTU) comprised of contractile elements (i.e. muscle, CE) and series elastic elements (i.e. tendon, aponeurosis, (SEE)) acting through a transmission (i.e. skeletal lever system) to drive a inertial-gravitational load (i.e. body). There are a select few studies that do just this, and use actual inertial-gravitational loads to investigate dynamic actuation properties of skeletal muscle using isolated frog [29] and cat [30] muscle. While these studies provide an excellent basis for understanding active force generation in muscle, they do not address the role that

muscle-tendon/limb architecture (i.e. form) plays in force transmission from muscle to environment (i.e. function).

In recent years, advances in robotics, controls, and instrumentation have made it possible to explore the interplay of environmental dynamics and muscle-tendon architecture/limb geometry in isolated muscle experiments [31,32]. Farahat et. al. used a simulated mass-spring-damper with a known resonant frequency to explore how frequency and phase of cyclically activated single and antagonist muscle pairs influenced overall mechanical power output of the system. Their findings indicated that, in the case of antagonist muscle pairs, mechanical power output could be significantly amplified compared to a single agonist when driving contractions at frequencies well above the natural frequency of the system [33]. Clemente et. al. took a different approach to environment simulation, and used a hybrid bio-robotic system to drive rotation and translation of a 3D printed foot through a fluid using forces generated by skeletal muscle. They were able to elegantly demonstrate the role that initial limb configuration, as well as force-length/velocity actuator properties of muscle, play in governing mechanical power output in a single burst propulsive swimming stroke [34].

This goal of the present study was to extend the concepts put forth by previous studies simulating ‘real-world’ loads [29,30,33,34] in order to ask a fundamentally different question: Can the passive resonant frequency of a biological muscle-tendon unit connected to an inertial-gravitational load determine the neural control strategy that yields ‘tuned’ elastic behavior, similar to that observed at distal joints during steady terrestrial locomotion? To establish a framework for inquiry we invoke the concept of mechanical resonance tuning as a way to describe emergent elastic limb behavior observed during steady terrestrial locomotion. We start with a very conceptually simple model: the driven simple harmonic oscillator (SHO). This classic mechanical system consists of a

spring of known stiffness attached via rigid interface to a mass through a pulley with a fixed gearing ratio (**fig. 1**). In essence, this is the most simple representation of an ankle plantarflexor driving vertical movement of the center of mass of the body through a lever system with a fixed effective mechanical advantage (i.e. vertical hopping). For this system, a key factor governing emergent dynamics is the system natural frequency (ω_0), or the resonant frequency, where it will oscillate passively if perturbed in the absence of any external driving force. This frequency is determined by system parameters as follows:

$$\omega_0 = \frac{l_{in}}{l_{out}} \sqrt{\frac{k_{MTU}}{M}}$$

Where $\frac{l_{in}}{l_{out}}$ is the moment arm ratio of the spring (l_{in}) and inertial-gravitational load (l_{out}), k_{MTU} is whole MTU stiffness, and M is system mass (**fig. 1**). The value of k_{MTU} was assumed to adhere to the following relationship:

$$k_{MTU} = \left(1/k_{CE} + 1/k_{SEE}\right)^{-1}$$

Where k_{CE} and k_{SEE} are CE and SEE stiffness respectively.

When driving the compliant SHO system, the relationship between driving frequency (ω_{Drive}) and ω_0 is critical. If ω_{Drive} is considerably lower than ω_0 , the spring acts as a direct coupling between driving force and inertial-gravitational load and system/driving force are nearly perfectly in phase. As ω_{Drive} approaches and becomes coincident with ω_0 , this phasing of driving vs. system force shifts, and the spring decouples driving and system motions while simultaneously storing and returning large amounts of elastic energy. This not only maximizes force output from the system, but also amplifies input power from driving forces/motions. If ω_{Drive} is increased beyond

ω_0 , phasing of driving and system forces continues to shift, and system elastic components become a mechanical buffer that eliminates effective transmission of driving force to the inertial-gravitational load [35].

In the case of a biological MTU, driving force is applied internally via active muscle contraction as a function of its neural and mechanical state. Furthermore, the ‘spring’ in this case consists of contributions from the muscle via its non-linear passive stiffness [36], as well as through biological series elastic elements (tendon, aponeurosis (SEE)) that exhibit either linearly or non-linear stiffness depending on the magnitude of its strain [7]. In other words, k_{MTU} can be highly variable depending on CE active/mechanical state and SEE strain. Given all of these complicating factors, it seems unlikely that a biological MTU would exhibit similar frequency-phase coupling to that observed for a classic SHO.

In spite of these complications, a recent study that used a Hill-type muscle-tendon model with human plantarflexor parameters to drive vertical hopping indicated mechanical resonance of the muscle-tendon unit occurred when stimulating muscle contraction with a frequency very close to the passive resonant frequency ω_0 [37]. However, Hill-type muscle-tendon models cannot reliably capture history dependent effects like lengthening dependent force enhancement and work dependent deactivation in active biological muscle [23,38-41], or hysteresis in biological tendon [42].

To determine whether the passive natural frequency (i.e. resonant frequency) of a compliant muscle-tendon determines the neural control strategy that leads to tuned elastic behavior, even in the context of history dependent effects of active muscle and SEE force generation, we developed an experimental preparation which (1) replaced our modeled biological MTU with a real one, (2) simulated inertial-gravitational environment dynamics through a feedback controlled servo motor,

and (3) drove muscle contraction through direct nerve stimulation across a range of frequencies centered around the passive natural resonant frequency of the passive muscle-tendon unit coupled to its load (**fig. 1**). Based on our previous modeling study [37], we hypothesized that our system would exhibit mechanical resonance when stimulated at a frequency 10% above the passive natural frequency (i.e. $+10\%\omega_o$). In this resonant condition we would expect to observe ‘tuned’ elastic behavior whereby muscle-tendon forces are maximized, and the highest percentage of mechanical power comes from energy stored and returned in SEE [12,19]. We would also expect emergent shifts in stimulation phasing centered below ω_o that facilitate muscle activation during system lengthening (i.e. stimulation onset precedes peak force) [12,43]. In essence we expect that form drives function. That is, underlying muscle-tendon architecture (k_{CE} and k_{SEE}), transmission geometry (l_{in} , l_{out}) and the size of the load (M) (i.e. form) dictates the neural control strategy needed for elastic behavior of a compliant muscle-tendon unit and ultimately the lower-limb (i.e. function).

2.3 Results

2.3.1 Overview

All data presented here is taken from *in vitro* experiments using the Plantaris muscle-tendon unit from the American bullfrog *Rana Catesbeiana*. The Plantaris complex was freed from the limb, and removed still attached to fragments of tibia and fibula, which were mounted to a plexiglass plate in a chamber of circulating oxygenated ringers solution. The free tendon was attached via rigid aircraft cable to a feedback controlled servo motor programmed to simulate a mass in gravity across a pulley of constant gear ratio (**fig. 1**). The sciatic nerve was left intact, and muscle contraction was

driven via a bipolar stimulating electrode across a range of frequencies centered around a measured ω_0 (**fig. 1**). Muscle contractile element (CE), series elastic tissue (SEE) and whole muscle-tendon unit(MTU) mechanics were de-coupled using direct measurement of muscle length changes via implanted sonomicrometry crystals (**fig. 1**). Further details on experimental preparation and execution can be found in the Methods section of this text.

2.3.2 General System Dynamics and Periodic Behavior

System dynamics observed in this study were generally cyclic, and self stabilizing (**fig. 1Ci-ii**). A representative mean dataset the final 4 cycles of muscle stimulation for all driving frequency (ω_{Drive}) conditions from a single experimental preparation is shown in **figure 2**. MTU force and MTU/CE ΔL were measured directly, and SEE ΔL was assumed to adhere to the following relationship:

$$\Delta L_{SEE}(t) = \Delta L_{MTU}(t) - \Delta L_{CE}(t)$$

MTU and component (CE/SEE) mechanical power (P_{mech}) were also computed for this preparation as follows:

$$P_{mech}(t) = F(t) * \frac{d}{dt} \Delta L(t)$$

Where $F(t)$ is recorded force vs. time. We assumed that pennation effects were small, and that $F_{MTU} = F_{CE} = F_{SEE}$. By examining these dynamics, it can be seen that there were alternating phases of energy storage and return for system-level (i.e. MTU) and individual components (i.e. CE/SEE) of the biomechanical system over a stretch-shorten cycle (**fig. 2**). Also note that, for conditions plotted against normalized cycle time (**figs. 2A-E, ii-iv**), standard deviations in force, length change, and

power output were quite small across all conditions; and initial and final mean dynamic behavior appeared to coincident (i.e. behavior is cyclic and steady state) (**fig. 2**).

2.3.3 Peak Force and Phasing Dynamics

The global maximum in observed mean peak force (F_{peak}) occurred for a driving frequency of $-10\%\omega_0$, and minimums were observed for the $\pm 20\%\omega_0$ conditions (**fig.3A**). This is reinforced by a significant 2nd order polynomial fit to experimental data ($p = 0.037, R^2 = 0.26$), which predicted that peak force would occur at or just below $\sim\omega_{Drive} = \omega_0$ (**fig. 3A, table 2**). The phasing of peak force consistently occurred $\sim 50\%$ of a cycle after minimum MTU length, or “bottom dead center” (BDC), across all conditions (**fig. 3B**). In general, phasing of peak force decreased slightly but significantly with increased ω_{Drive} ($p = 0.0002, R^2 = 0.47$) (**table 2**). The phasing of stimulation onset relative to BDC, however, varied significantly across frequencies ($p = 0.012, R^2 = 0.46$) (**fig. 3B, table 2**). For the $-20\%\omega_0$ condition, stimulation onset was coincident with peak force (50%), and transitioned to a global minimum of 25% in the ω_0 condition (**fig. 3B**). For driving frequencies $> \omega_0$, phasing of stimulation onset began to rise again, while phasing of peak force dropped slightly (**fig. 3B**). While it is difficult to say where shifts in stimulation phasing is *centered* relative to the minimum at ω_0 , there is no doubt that it occurs below the system’s passive ω_0 (**fig. 3B**).

2.3.4 Muscle Mechanical State at Peak Force

The ability for the CE to actively generate force is intrinsically coupled to its mechanical state, and this CE strain and velocity at the time of peak force were of great interest in this study. In general, higher driving frequencies resulted in lower normalized strains at peak force (**fig. 3C**). Normalized CE velocity, however, shifted from shortening at peak force, to lengthening between

driving frequencies of $-10\%\omega_0$ and ω_0 (**fig. 3D**). Of these two metrics, only trends in v_{CE} could be verified statistically ($p = 0.0021, R^2 = 0.34$) (**table 2**)

2.3.5 Power Output and Sharing

Average positive mechanical power (\bar{P}_{mech}) for MTU and CE/SEE was computed by integrating instantaneous mechanical power over a cycle and dividing by stimulation cycle period ($T_{Drive} = \omega_{Drive}^{-1}$) as follows:

$$\bar{P}_{mech} = \frac{1}{T_{Drive}} \int_{t=0}^{t=T_{Drive}} P_{mech}(t) dt$$

To get average positive and negative powers (\bar{P}_{mech}^+ and \bar{P}_{mech}^- respectively), the same calculation was made for only positive or negative values of instantaneous power.

A \bar{P}_{mech}^{net} output of ~ 0 was observed across all frequencies at both the MTU (**fig. 4A**) and component (CE/SEE) (**fig. 4B-C**) level, indicating steady cyclic behavior (i.e. locomotion on level ground at constant speed) and equal amounts of both \bar{P}_{mech}^+ and \bar{P}_{mech}^- output from MTU and CE/SEE over a given stimulation cycle (**fig. 2, 4**). The only metrics with statistically significant regression fits, however, were MTU \bar{P}_{mech}^- ($p = 0.030, R^2 = 0.28$) (**fig. 4A, table 2**), and both SEE \bar{P}_{mech}^- ($p = 0.0043, R^2 = 0.39$) and \bar{P}_{mech}^+ ($p = 0.035, R^2 = 0.26$) (**fig. 4C, table 2**). For these metrics, all fits predict maximal absolute values for ω_{Drive} slightly above ω_0 . A similar trend emerges in \bar{P}_{mech}^+ sharing between CE and SEE components, and we found maximal %SEE/minimal %CE contribution to overall system \bar{P}_{mech}^+ ω_{Drive} between ω_0 and $+10\%\omega_0$ ($p < 0.0001, R^2 = 0.71$) (**fig. 4D, table 2**).

2.3.6 Modeled Metabolic Rate and Apparent Efficiency

Modeled average metabolic power and estimated apparent efficiency of CE and whole MTU positive mechanical work are shown in **figure 5**. Modeled dimensionless metabolic rate was computed as a function of normalized velocity [44], where maximal shortening velocity (v_{max}) was assumed to adhere to the relationship [45]:

$$v_{max} = -13.8l_0 \cdot s^{-1}$$

and s is the unit of time ‘seconds’. Instantaneous dimensionless metabolic cost ($p_{met}(t)$) was scaled by physiological constant F_{max} and modeled muscle active state α [46], which was computed using our experimentally applied stimulus pattern $u(t)$, and estimated $\tau_{act} / \tau_{deact}$ values [47](**table 1**) to model instantaneous rate of metabolic power as follows:

$$P_{met}(t) = F_{max} \cdot \alpha(t, u(t), \tau_{act}, \tau_{deact}) \cdot p_{met}(t)$$

Average metabolic power (\bar{P}_{met}) was calculated using the same approach as for average mechanical power (\bar{P}_{mech}). Maximum modeled metabolic energy consumption occurred for a driving frequency of $-20\%\omega_0$, and the minimum was observed at $\omega_{Drive} = \omega_0$ (**fig. 5A**). In general, driving frequencies $< \omega_0$ consumed the most metabolic energy, and the metabolic demand of operating at frequencies $\geq \omega_0$ was generally low (**fig. 5A**). That being said, polynomial fits to this data were not significant, and no definitive conclusions can be drawn based on modeled outcomes (**table 2**).

To estimate CE and MTU apparent efficiency (ε_{app}) of positive mechanical work for input unit of metabolic energy, the following equation was used:

$$\varepsilon_{app} = \bar{P}_{mech}^+ / \bar{P}_{met}$$

Mean values of CE ε_{app} were generally low ($<.10$), subject to large standard error (**fig. 5B**), and did not vary significantly as a function of driving frequency (**fig. 5B, table 2**). Mean MTU ε_{app} , on the other hand, exhibited more pronounced variation relative to ω_{Drive} . Although 2nd order polynomial regression fits were not significant, they were close ($p = 0.064, R^2 = 0.22$) (**table 2**); and predicted maximums aligned well with predicted maximums in F_{peak} (**fig. 3A**), SEE $\bar{P}_{mech}^{+/-}$ (**fig. 4C**), and $\%SEE\bar{P}_{mech}^+$ (**fig. 4D**).

2.4 Discussion and Conclusions

2.4.1 General System Dynamics

The overarching hypothesis in this study was that peak mechanical tuning of biological CE/SEE interactions was intrinsically tied to the relationship between driving frequency ω_{Drive} , and system passive resonant frequency ω_0 . In other words, we hypothesized that system ‘form’, or mechanical properties governing ω_0 (i.e. k_{MTU}, l_{in}, l_{out} , and M), would ultimately govern system ‘function’ (i.e. ‘tuned’ MTU mechanics) relative to ω_{Drive} . We initially predicted that peak tuning would be observed at a driving frequency of $+10\%\omega_0$ based on previous modeling studies.

Our main hypothesis was partially supported by experimental data and subsequent regression fits (**table 2**). Behavior characteristic of resonant tuning would exhibit peak system force and maximal contributions to overall system \bar{P}_{mech} from SEE energy storage and return. Trends in peak

force predicted by statistically significant regression trends are maximized at a frequency at or *just* below $\omega_{Drive} = \omega_0$ (**fig. 3A, table 2**), while statistically significant maximums in regression trends of percent contribution to overall power output from energy stored/returned in SEE were predicted for a ω_{Drive} at or *just* above ω_0 (**fig. 4D, table 2**). In general, maximums in both of these characteristic outcomes of a ‘tuned’ MTU system appear to be centered around $\omega_{Drive} = \omega_0$, and not our initially predicted value of $+10\%\omega_0$.

A secondary aspect of this main hypothesis was that emergent stimulation phasing dynamics would undergo a shift centered on a $\omega_{Drive} < \omega_0$, ultimately resulting muscle activation during MTU lengthening to better facilitate SEE energy storage and return [37]. This expected outcome was verified by experimental data as well as statistically significant regression trends (**fig. 2Aiii-Eiii, 3B, 3D, table 2**). The phase of stimulation onset shifted from $\sim 55\%$ in the $-20\%\omega_0$ condition, to a global minimum $\sim 25\%$ in the $\omega_{Drive} = \omega_0$ condition, while the phasing of peak force remained, occurring $\sim 50\%$ of a cycle following minimum MTU length in all conditions (**fig. 3B**).

2.4.2 From De-tuned to Tuned and Back Again: Frequency-Phase

Coupling in Biological MTU

To provide context for the idea of resonance tuning in a biological MTU, we used the classical simple harmonic oscillator (SHO) as an example. This is, in the mechanical sense, a grossly oversimplified representation of tuned interaction between muscle, tendon, transmission, load, and environment; but there are several fundamental features that each of these systems share.

For the classic SHO oscillator, driving it well below its resonant frequency will result in the elastic component effectively operating as a rigid coupling between mass and driving force. By

examining the time-course dynamics of the $\omega_{Drive} = -20\%\omega_0$ condition early in a stimulation cycle (first 10-15% of a cycle following stimulation onset), it can be seen that $\Delta L_{CE} = \Delta L_{MTU}$, with the pre-loaded tendon acting as connector between CE and environment (**fig. 2Aiii**). This is not an uncommon role for tendon to play in general, but is energetically non-ideal for a distal MTU known to supplying the majority of mechanical power output during steady locomotion from a relatively small volume of muscle (e.g. ankle plantarflexors) [17,48]. Driving the MTU at $-20\%\omega_0$ ultimately resulted in minimal values of F_{peak} (**fig. 4A**), minimums in SEE energy storage and return (**fig. 4C**), minimum SEE contributions to overall \bar{P}_{mech}^+ (**fig. 4D**), as well as maximal predicted metabolic demand (**fig. 5A**) and minimal MTU apparent efficiency (**fig. 5C**).

As ω_{Drive} is increased towards ω_0 for our biological MTU, the system began to ‘tune’ itself much the way a SHO might, and stimulation onset shifted phasing to precede peak system length/force, reaching a global minimum at $\omega_{Drive} = \omega_0$ (**fig. 3B**). Under these conditions, the SEE effectively decoupled CE and whole MTU mechanics, allowing CE to shorten internally against a lengthening SEE and MTU (**fig. 2B-E**). Following an initial shortening phase, the interaction of muscle mechanical state and system inertial demands was such that muscle lengthened approaching peak system length/force (**fig. 3D**), further amplifying its active force generation capabilities [23]. This facilitated significant energy storage and return in the SEE (**figs. 2, 4C, D**), amplified system power output (**fig. 4A**), drove down predicted metabolic demand (**fig. 5A**), and ultimately maximized MTU ε_{app} for the $\omega_{Drive} = \omega_0$ condition (**fig. 5C**).

These highly favorable dynamics only persist for a narrow range of frequencies, though, and phasing of stimulation onset begins to increase again for $\omega_{Drive} > \omega_0$ conditions. For the highest driving frequency examined here ($\omega_{Drive} = +20\%\omega_0$), there is still effective decoupling of CE and

MTU mechanics via SEE energy storage/return, but very little of this internal energy exchange is ultimately transmitted to the environment (**fig. 2E, 4A**). This is also consistent with SHO behavior, and the net result is reduced mechanical performance (i.e. $F_{peak}, P_{mech}^{+/-}$) (**figs. 2E, 3A, 4**), increased predicted metabolic cost (**fig. 5A**), and decreased MTU ε_{app} (**fig. 5C**).

2.4.3 Form, Function, and the Energetics of Resonance

Previous studies of human bouncing have used indirect approaches for identifying [12,19,49], and even imposing [43] the resonant frequency of the human ankle plantar flexor muscle tendon complex. These studies collectively identify several key features of human bouncing at resonance, including minimal ratio of CE to whole MTU work [12,19], maximized gains between muscle activation and peak force [43], minimized metabolic demand [19,49], and maximized apparent efficiency [19]. Our own data exhibits all of these outcomes, with our most ‘tuned’ condition (i.e. $\omega_{Drive} = \omega_0$) resulting in maximal peak forces (**fig. 3A**), a minimized percentage of total MTU \bar{P}_{mech}^+ from the CE (**fig. 4D**), minimized estimated metabolic cost (**fig. 5A**), and maximized MTU apparent efficiency (**fig. 5C**).

To our knowledge, we are the first to directly link form and function in a driven biological MTU by measuring ω_0 , and showing that resonant behavior of the actively driven system is explicitly tied to *passive* muscle tendon properties (i.e. passive ω_0). In so doing, this study also demonstrated that high level active control was not required to properly time muscle activation for elastic energy storage and return. There was an inherent frequency-phase coupling in a cyclically activated MTU, and by proper selection of movement frequency, effective phasing of activation for elastic energy storage and return occurred naturally. We hope that identifying these underlying principles

governing elastic muscle-tendon behavior will provide the basis for physiology-based framework for understanding how mechanically simple elastic limb behavior may emerge from a complex biological system-comprised of many simultaneously ‘tuned’ muscle-tendons within the lower-limb [50].

2.5 Future Directions

The bio-robotic platform we have demonstrated here is a potentially powerful tool for linking form and function in terrestrial gait. In future work, we hope to further develop environment simulator controls to inject or remove kinetic energy from our virtual mass during the ‘flight’ phase of the stimulation cycle. By applying this on a cycle by cycle basis, we hope to simulate steady state uphill/downhill locomotion, and explore if/how the interplay of environment and muscle actuator properties lead to net work production or dissipation over the course of a gait cycle. We also hope to inject/remove kinetic energy within a single stimulation cycle to simulate an unexpected perturbation to steady state behavior. In doing so, we hope to identify the role that neuromechanical ‘preflex’ plays in perturbation rejection and re-stabilization of system mechanics.

2.6 Materials and Methods

2.6.1 Animal Subjects

All experiments shown here were approved by the North Carolina State University Institutional Animal Care and Use Committee. Five adult American bullfrogs (*Rana Catesbeiana*)

(mean body mass = $374.3\text{g} \pm 50.3\text{g}$) (**table 1**) were purchased from a licensed vendor (Rana Ranch, Twin Falls, ID) and housed in the NC State University Biological Resources Facility. Upon arrival, there was a one week adaptation period prior to use in experiments. Animals were fed crickets *ad libitum*, and housed in an aquatic environment with free access to a terrestrial platform. Prior to use in experiments, animals were cold-anesthetized and sacrificed using the double-pith technique.

2.6.2 Surgical Protocol and Instrumentation

A single limb was detached from the sacrificed animal at the hip joint, and skin was removed. The limb was then submerged in a bath of oxygenated ringers solution (100 mM NaCl, 2.5 mM KCl, 2.5 mM NaHCO_3 , 1.6 mM CaCl, 10.5 mM Dextrose) at room temperature ($\sim 22^\circ\text{C}$) for the duration of surgery. All muscles proximal to the knee, as well as the tibialis anterior, were removed with great care was taken to keep the sciatic nerve intact. The plantaris longus muscle tendon unit was separated from the calf shank but left intact at its proximal insertion point at the knee joint. Free tendon and aponeurosis carefully removed and preserved up to the distal insertion point at the toes. Muscles were instrumented with two sonomicrometry crystals (1mm diameter, Sonometrics Inc., London, Ontario, CA) implanted along a proximal muscle fascicle. A bipolar stimulating electrode cuff (Microprobes for Life Science, Gaithersburg, MD, USA) was placed around the intact sciatic nerve and connected to an Aurora 701C stimulator (Aurora Scientific, Aurora, Ontario, Canada). The animal's foot was removed proximal to the ankle joint, and intact portions of femur and tibia were mounted to a plexiglass plate. A custom friction clamp was placed over distal portions of the free tendon, and the whole prep was inserted into a plexiglass chamber with continuously circulating oxygenated ringers solution at 27°C . The tendon clamp was then attached to a feedback controlled

ergometer (Aurora 310B-LR, Aurora Scientific, Aurora, Ontario, CA) for the duration of the experiment.

2.6.3 Ergometer Motor Controller

The ergometer used in all experimental conditions was connected to a dSpace DS1103 control board (dSpace, Paderborn, DE) running custom controllers written in Simulink (Mathworks Inc., Natick, MA, USA). Controllers were designed to take force measure on the ergometer, and simulate a virtual interaction with a mass in gravity with a fixed moment arm ratio ($M = 0.085kg, l_{in} = 1, l_{out} = 21$, **fig. 1**). These parameters were selected assuming a passive MTU stiffness of 7,000 N/m to impose a system passive resonant frequency ~ 2 Hz. Other factors driving the selection of these parameters in particular included limitations on ergometer range of motion (± 20 mm), and desired mean passive force during passive oscillation that were unlikely to damage the muscle (mean force = 17N ($\sim 30\% F_{max}$)), **fig. 1**).

To determine motor arm displacement at each time-step, we used a 4th order Runge-Kutta fixed step solver with a sampling rate of 1kHz. Forces generated in by the biological MTU adhered to the following relationship:

$$F_{MTU}l_{in} = F_{load}l_{out}$$

Where F_{load} is the force being applied to our virtual mass. Net force on the virtual load at each time-step was computed as follows:

$$F_{load}^{net} = M\ddot{x}_{load} = F_{MTU} \left(\frac{l_{in}}{l_{out}} \right) - Mg$$

Where \ddot{x}_{load} is the acceleration of the load, and g is gravitational acceleration (9.8m/s^2), and $F_{MTU} \left(\frac{l_{in}}{l_{out}} \right) = F_{load}$. With F_{net} computed, we next solve for \ddot{x}_{load} , integrate twice to compute a time-step displacement (dx_{load}), and apply the following equation to determine MTU time-step displacement:

$$dx_{MTU} = - \left(\frac{l_{out}}{l_{in}} \right) dx_{load}$$

Inertial parameters were selected for an assumed a passive k_{MTU} of 7,000 N/m to impose a system passive resonant frequency $\sim 2.2\text{Hz}$ [37]. Other factors driving the selection of these parameters in particular included limitations on ergometer range of motion ($\pm 20\text{mm}$), and desired mean passive force during passive oscillation that were unlikely to damage the muscle (mean force = 17N, or $\sim 30\%$ F_{max} for a typical prep) (**fig. 1**).

2.6.4 Determination of Muscle Properties

To determine maximal muscle isometric force (F_{max}), the sciatic nerve was supramaximally stimulated with 0.2ms pulses at a pulse rate of 100s^{-1} for 300ms under various amounts of passive tension. The same rate and duration of stimulus pulses was used in all subsequent conditions requiring muscle activation. The condition for which F_{max} was observed was also used to approximate muscle τ_{act} and τ_{deact} values. Using an equation from Zajac, we performed a brute force least squared error fit by sweeping a parameter space consisting of reasonable values for each parameter, and determined subject-specific values for use in estimating metabolic cost ($\tau_{act} = 0.066 \pm 0.011, \tau_{deact} = 0.100 \pm 0.020$) [47].

To determine the system passive resonant frequency (ω_0) we allowed the inactive MTU to oscillate against our simulated inertial system until steady-state behavior was reached (**fig. 1B**). This observed frequency of oscillation was ω_0 ($\bar{\omega}_0 = 2.34 \pm .11Hz$), and all dynamic stimulation frequencies were centered on this value.

Prior to dynamic conditions, three fixed end contractions (FEC) were performed at a stimulation frequency of ω_0 , a stimulation duty of 10% as a means of determining a base line force for estimating muscle fatigue. This same pattern of stimulus was applied following all dynamic conditions, and if the peak force achieved was $\geq 60\%$ of the initial value, the experiment was ruled a success (average %*Fatigue* = $76 \pm 16.9\%$) (**table 1**).

2.6.5 Dynamic Conditions

For conditions where there was dynamic interaction between the active MTU and simulated inertial load, the driving frequency was varied between $\pm 20\% \omega_0$ in 10% intervals. The order of driving frequency conditions was randomized to counteract fatigue effects, and each frequency condition consisted of 8 cycles of stimulation (**fig. 1C**). Each trial began with the biological MTU under 1N of passive tension, and the inertial load resting on a virtual ‘table’. In order to disengage the table, MTU force must exceed that of the gravitational load, i.e.:

$$F_{MTU} > \left(l_{out} / l_{in} \right) Mg$$

Once this condition is satisfied ($F_{MTU} > 17.5N$ for parameters used here), the ‘table’ is removed, and there is no constraint placed on system dynamics from that point on (**fig. 1**). The system was allowed four stimulation cycles to reach steady-state behavior (**fig. 1C**), and the last four cycles were used in all subsequent analysis.

2.6.6 Statistical Analysis

To address our hypotheses we performed polynomial regression analyses to test for significant trends in key outcome variables as a function of muscle stimulation frequency (ω_{Drive}). Each dependent variable was subjected to stepwise 1st and 2nd order polynomial fits to all data from each experimental preparation (n=5) to determine whether or not statistically significant trends were present ($p < 0.05$). In the event that a fit was non-significant, the ‘best’ fit based on lowest p-value was used to represent observed trends. We evaluated ‘goodness of fit’ using the R^2 statistic (**table 2**).

2.7 Tables

Table 1, Measured and Estimated Parameters: Mean \pm 1STD values of measured and predicted physiological constants from all experimental subjects.

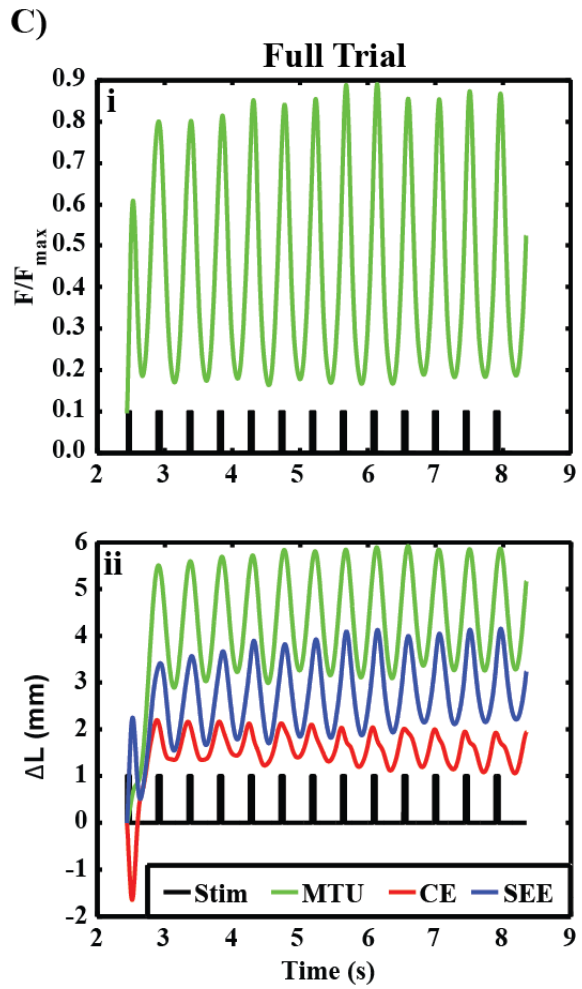
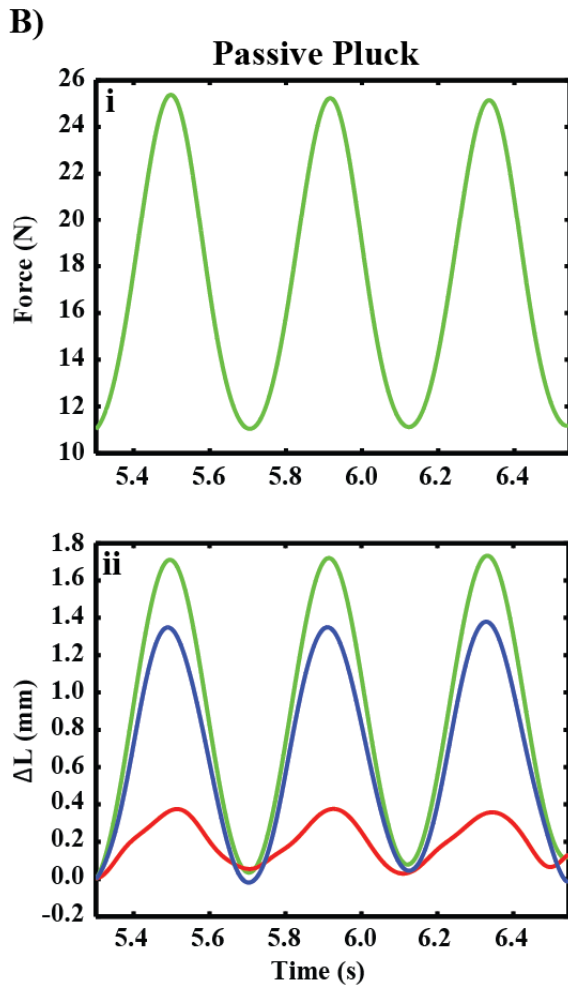
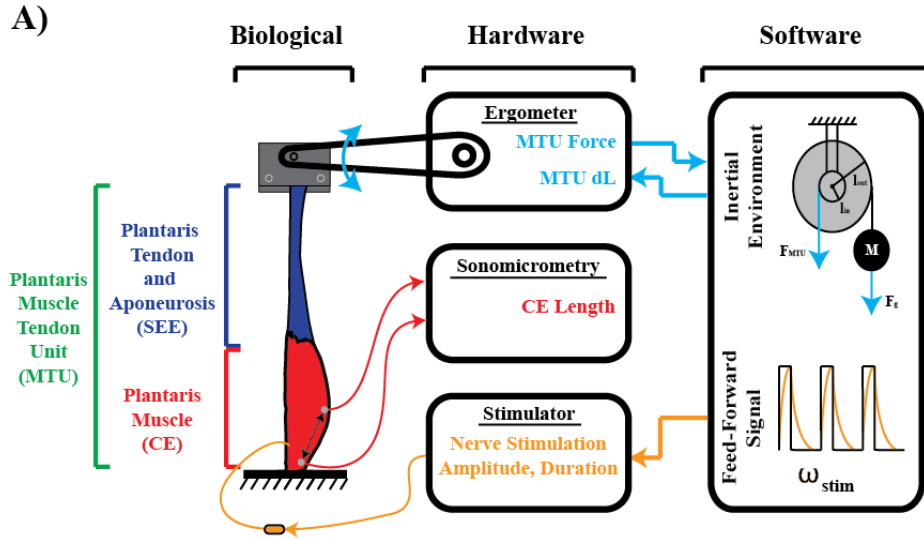
Physiological Parameter	Mean \pm 1STD
ω_0	2.34 ± 0.11 Hz
l_{in}	1
l_{out}	21
M	0.085 kg
F_{max}	43.41 ± 10.31 N
τ_{act}	0.066 ± 0.011 s
τ_{deact}	0.100 ± 0.02 s
l_0	10.74 ± 2.89
v_{max}	-148 ± 40 mm/s
Muscle mass	4.79 ± 0.98 g
Animal mass	374.3 ± 50.3
Fatigue %	$76 \pm 16.9\%$

Table 2, Regression Fits: Table of regression fit order, equation, R^2 , and p values for all reported metrics. A p value with red text indicates a non-significant trend.

Metric	Fit Order	Fit Equation	R^2	p-value	Figure
F_{peak}/F_{max}	2nd	$0.90 - 0.14\omega - 4.73\omega^2$	0.26	0.037	3A
%Phase F_{peak}	1st	$48.10 - 18.47\omega$	0.47	0.0002	3B
%Phase Stim	2nd	$26.60 - 48.80\omega + 479.19\omega^2$	0.46	0.012	3B
CE Strain @ F_{peak}	1st	$1.33 - 0.54\omega + 1.48\omega^2$	0.12	0.084	3C
CE v @ F_{max}	2nd	$-0.02 - .16\omega + .51\omega^2$	0.40	0.0039	3D
MTU \bar{P}_{mech}^+	2nd	$35.80 - 16.24\omega - 270.66\omega^2$	0.20	0.085	4A
MTU \bar{P}_{mech}^-	2nd	$-43.76 - 41.52\omega + 272.31\omega^2$	0.28	0.030	4A
MTU \bar{P}_{mech}^{net}	1st	$2.48 - 3.54\omega$	0.03	0.43	4A
CE \bar{P}_{mech}^+	1st	$11.87 - 5.49\omega$	0.02	0.56	4B
CE \bar{P}_{mech}^-	1st	$-12.01 - 18.00\omega$	0.12	0.078	4B
CE \bar{P}_{mech}^{net}	1st	$2.89 - 10.41\omega$	0.11	0.11	4B
SEE \bar{P}_{mech}^+	2nd	$36.10 + 29.76\omega - 348.35\omega^2$	0.26	0.035	4C
SEE \bar{P}_{mech}^-	2nd	$-43.66 - 64.03\omega + 337.27\omega^2$	0.39	0.0043	4C
SEE \bar{P}_{mech}^{net}	1st	$-0.41 + 6.87\omega$	0.08	0.168	4C
% P_{mech}^+ CE	2nd	$21.65 - 41.78\omega + 390.49\omega^2$	0.71	<0.0001	4D
% P_{mech}^+ SEE	2nd	$78.35 + 41.78\omega - 390.49\omega^2$	0.71	<0.0001	4D
\bar{P}_{met}	1st	$113.56 - 64.46\omega + 472.46\omega^2$	0.09	0.36	5A
CE ε_{app}	1st	$0.09 - 0.03\omega$	0.01	0.62	5B
MTU ε_{app}	2nd	$0.33 - 0.09\omega - 4.03\omega^2$	0.22	0.064	5C

2.8 Figures

Figure 1, Experimental Schematic and Sample Data: **A)** Schematic of biological (left), hardware (middle) and software (right) components used in experimental execution. **B)** A 3 cycle ample of steady state **i)** force and **ii)** length change data from a “passive pluck” condition used to experimentally determine ω_0 . The absolute time between peaks in force/length (T_{peak}) was assumed to adhere to the relationship $T_{peak} = \omega_0^{-1}$. **C)** Experimental **i)** force and **ii)** length data from a trial where the biological MTU was [accidentally] driven for 14 cycles of stimulation at $\omega_{Drive} = -5\% \omega_0$. This data is shown because it was longer than a typical 8 cycle experimental trial, and nicely demonstrated rapid stabilization and periodic behavior present across experimental conditions.



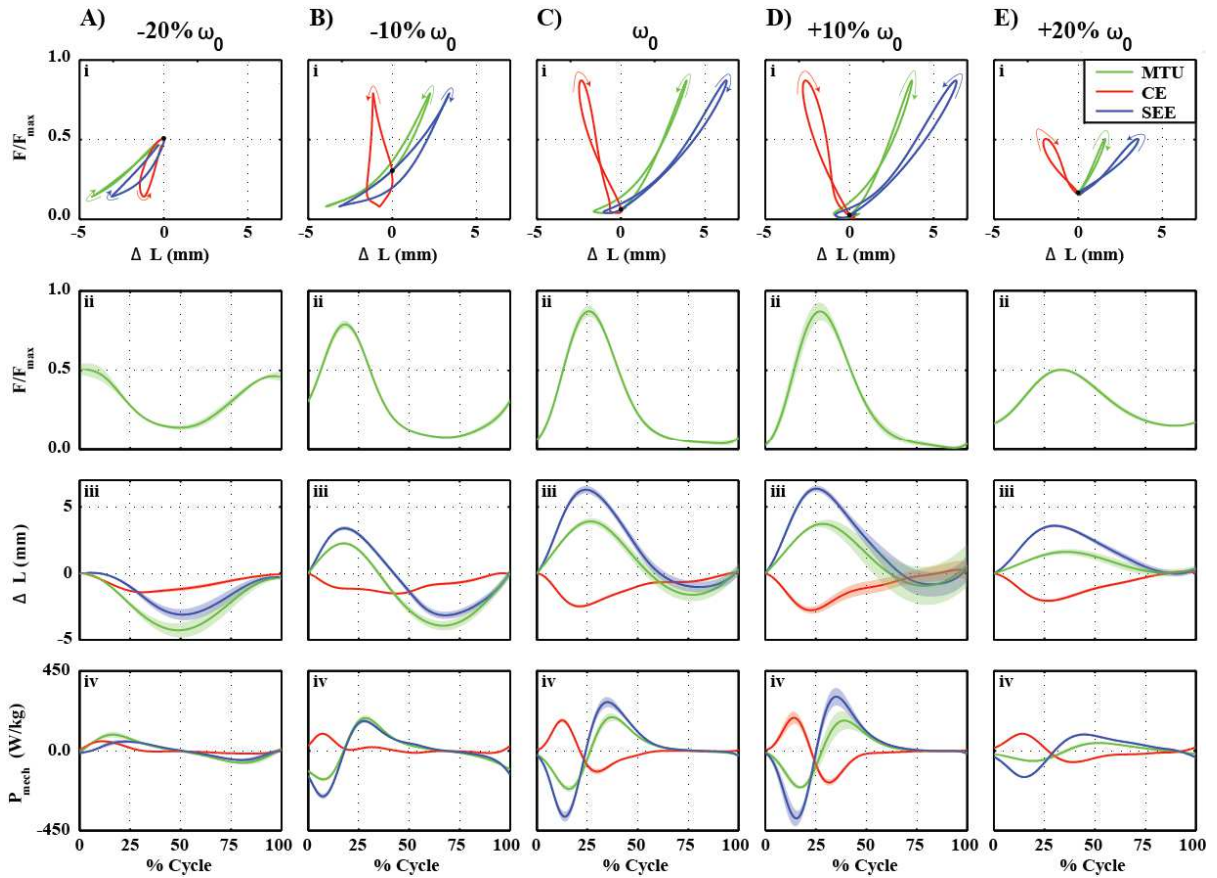


Figure 2, Cycle Dynamics: A representative dataset from a single subject showing **i)** mean workloop **ii)** force ± 1 SE, **iii)** $\Delta L \pm 1$ SE, and **iv)** power ± 1 SE output dynamics for the **A)** $-20\% \omega_0$, **B)** $-10\% \omega_0$, **C)** ω_0 , **D)** $+10\% \omega_0$, and **E)** $+20\% \omega_0$ conditions. All mean/SE data is based on the last 4 stimulation cycles from each condition. Note that SE bounds are generally small, indicating steady state behavior from cycle to cycle. Also note progression from ‘detuned’ to ‘tuned’ between ω_{Drive} of $-20\% \omega_0$ and ω_0 (**Ai-iv** to **Ci-iv**), and back to ‘detuned’ again in the -20% condition (**Ci-iv** to **Ei-iv**).

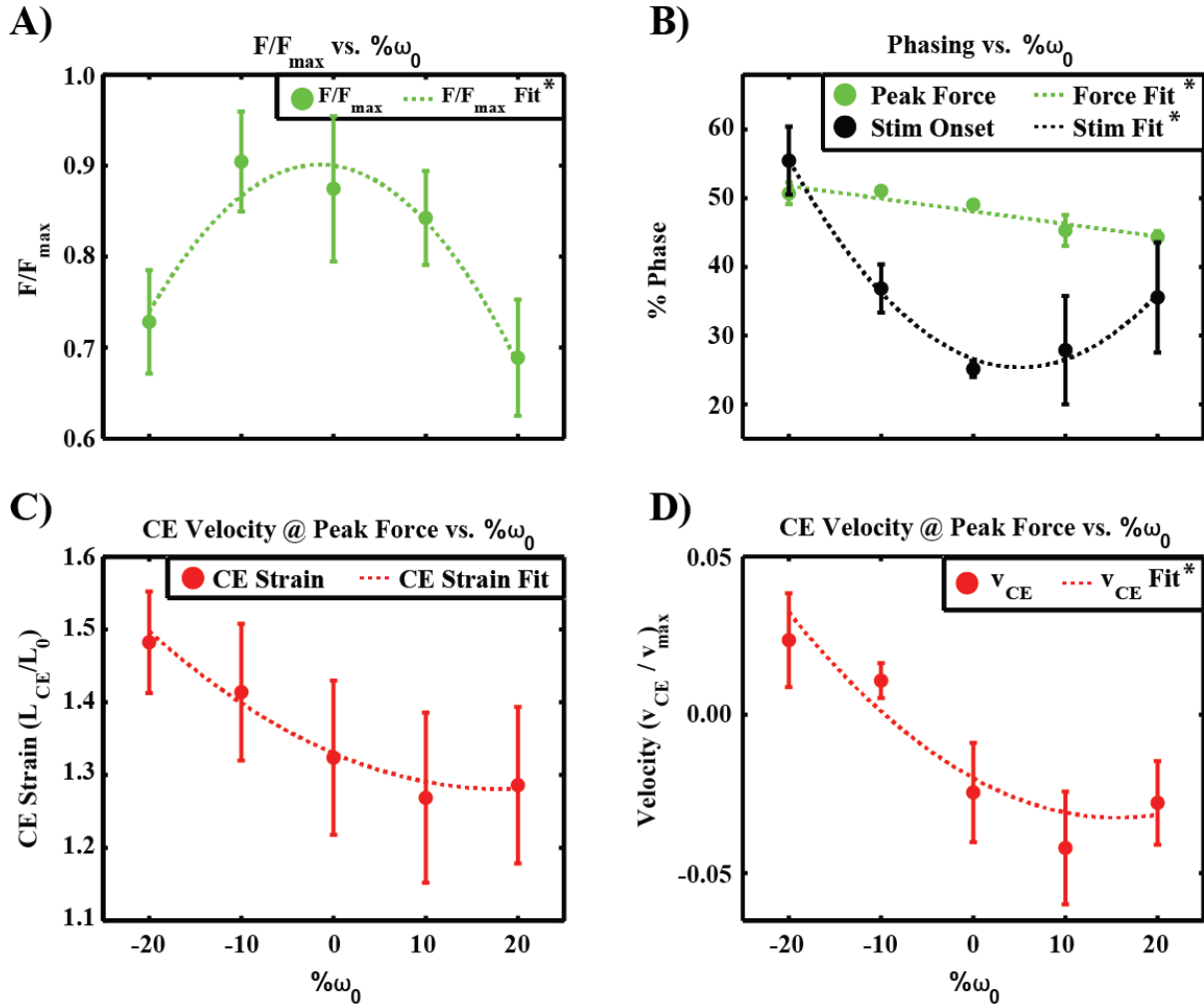


Figure 3, Peak Force, Phasing, and CE Operating Point: Plots of mean \pm 1SE **A)** Peak force (normalized to F_{max}), **B)** Phasing of peak force (green) and stimulation onset (black) relative to minimum MTU length expressed as percentage of a stimulation cycle, **C)** CE strain at peak force (normalized l_0), and **D)** CE velocity at peak force (normalized to v_{max}). In all figures, significant fits are indicated by a * in their respective plot legends (**table 2**). Note that peak force (**A**), minimum stimulation phasing (**B**), and the transition from lengthening to shortening at peak force (**D**) are all coincident with $\omega_{Drive} = \omega_0$.

Figure 4, Average Power Output and Sharing: Plots of mean ± 1 SE of average positive, negative and net power output (\bar{P}_{mech}^+ , \bar{P}_{mech}^- , and \bar{P}_{mech}^{net} respectively) for the **A)** MTU, **B)** CE, and **C)** SEE, as well as **D)** the percentage of total positive power generated in CE and SEE. In all plots, significant regression trends are bracketed and marked with a * (**table 2**). Note that $\bar{P}_{mech}^{net} = 0$ for all conditions in all components (**A-C**), and that maximums in MTU (**A**), SEE (**C**), and %SEE (**D**) are all maximized at or just above $\omega_{Drive} = \omega_0$.

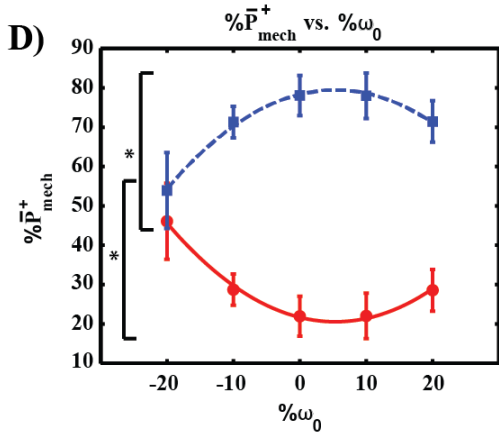
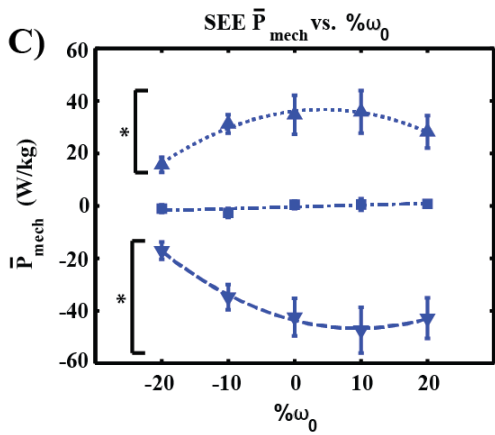
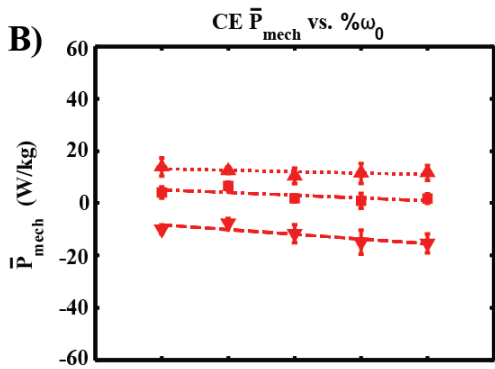
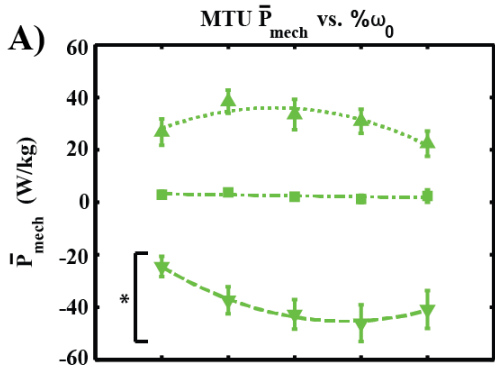
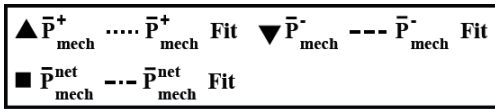
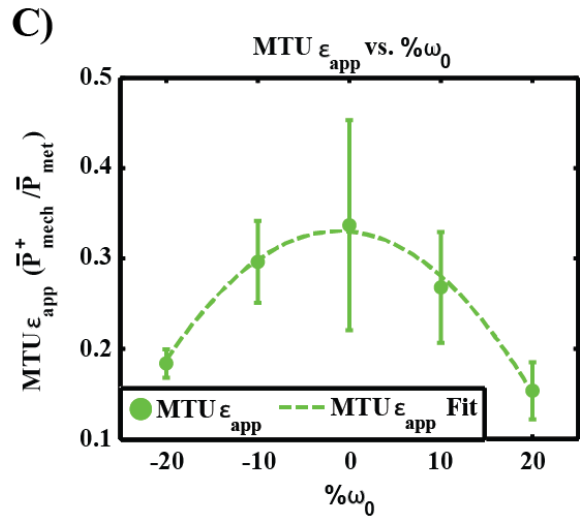
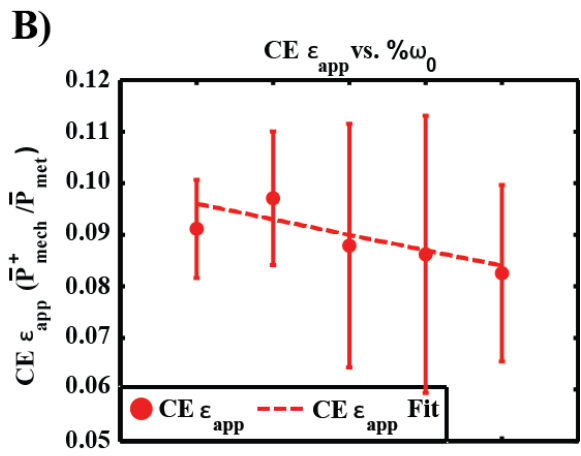
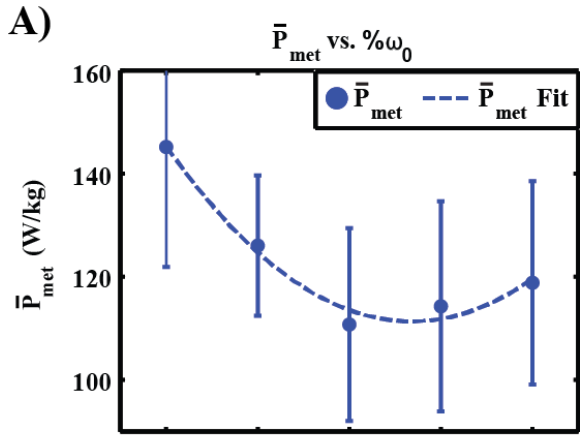


Figure 5, Estimated Metabolic Cost and Apparent Efficiency:
Plots of mean ± 1 SE of **A)** estimated average metabolic rate (\bar{P}_{met}), and apparent efficiency (ϵ_{app}) of the **B)** CE and **C)** MTU. None of the regression trends fit here were significant (**table 2**). Note that minimums in \bar{P}_{met} (**A**) and maximums in MTU ϵ_{app} (**C**) are coincident with $\omega_{Drive} = \omega_0$.



References

1. Farley CT, Glasheen J, McMahon TA (1993) Running springs: speed and animal size. *J Exp Biol* 185: 71-86.
2. Farley CT, Gonzalez O (1996) Leg stiffness and stride frequency in human running. *J Biomech* 29: 181-186.
3. Blickhan R (1989) The spring-mass model for running and hopping. *J Biomech* 22: 1217-1227.
4. Geyer H, Seyfarth A, Blickhan R (2006) Compliant leg behaviour explains basic dynamics of walking and running. *Proc Biol Sci* 273: 2861-2867.
5. Daley MA, Biewener AA (2006) Running over rough terrain reveals limb control for intrinsic stability. *Proc Natl Acad Sci U S A* 103: 15681-15686.
6. Seyfarth A, Geyer H, Herr H (2003) Swing-leg retraction: a simple control model for stable running. *J Exp Biol* 206: 2547-2555.
7. Lichtwark GA, Wilson AM (2007) Is Achilles tendon compliance optimised for maximum muscle efficiency during locomotion? *Journal of Biomechanics* 40: 1768-1775.
8. Ferris DP, Farley CT (1997) Interaction of leg stiffness and surfaces stiffness during human hopping. *J Appl Physiol* (1985) 82: 15-22; discussion 13-14.
9. Chang YH, Roiz RA, Auyang AG (2008) Intralimb compensation strategy depends on the nature of joint perturbation in human hopping. *J Biomech* 41: 1832-1839.
10. Farley CT, Morgenroth DC (1999) Leg stiffness primarily depends on ankle stiffness during human hopping. *J Biomech* 32: 267-273.

11. van der Krogt MM, de Graaf WW, Farley CT, Moritz CT, Richard Casius LJ, et al. (2009) Robust passive dynamics of the musculoskeletal system compensate for unexpected surface changes during human hopping. *J Appl Physiol* 107: 801-808.
12. Takeshita D, Shibayama A, Muraoka T, Muramatsu T, Nagano A, et al. (2006) Resonance in the human medial gastrocnemius muscle during cyclic ankle bending exercise. *J Appl Physiol* 101: 111-118.
13. Farris DJ, Robertson BD, Sawicki GS (2013) Passive elastic exoskeletons reduce soleus muscle force but not work in human hopping. *J Appl Phys.*
14. Lichtwark GA, Wilson AM (2005) In vivo mechanical properties of the human Achilles tendon during one-legged hopping. *J Exp Biol* 208: 4715-4725.
15. Lichtwark GA, Barclay CJ (2010) The influence of tendon compliance on muscle power output and efficiency during cyclic contractions. *J Exp Biol* 213: 707-714.
16. Roberts TJ, Azizi E (2011) Flexible mechanisms: the diverse roles of biological springs in vertebrate movement. *J Exp Biol* 214: 353-361.
17. Roberts TJ, Marsh RL, Weyand PG, Taylor CR (1997) Muscular force in running turkeys: the economy of minimizing work. *Science* 275: 1113-1115.
18. Lichtwark GA, Barclay CJ (2012) A compliant tendon increases fatigue resistance and net efficiency during fatiguing cyclic contractions of mouse soleus muscle. *Acta Physiol (Oxf)* 204: 533-543.
19. Dean JC, Kuo AD (2011) Energetic costs of producing muscle work and force in a cyclical human bouncing task. *J Appl Physiol* 110: 873-880.
20. Biewener AA, Konieczynski DD, Baudinette RV (1998) In vivo muscle force-length behavior during steady-speed hopping in tammar wallabies. *J Exp Biol* 201: 1681-1694.

21. Biewener AA, McGowan C, Card GM, Baudinette RV (2004) Dynamics of leg muscle function in tammar wallabies (*M. eugenii*) during level versus incline hopping. *J Exp Biol* 207: 211-223.
22. Biewener AA, Daley MA (2007) Unsteady locomotion: integrating muscle function with whole body dynamics and neuromuscular control. *J Exp Biol* 210: 2949-2960.
23. Josephson RK (1999) Dissecting muscle power output. *J Exp Biol* 202: 3369-3375.
24. Ahn AN (2012) How muscles function--the work loop technique. *J Exp Biol* 215: 1051-1052.
25. Barclay CJ, Lichtwark GA (2007) The mechanics of mouse skeletal muscle when shortening during relaxation. *J Biomech* 40: 3121-3129.
26. Ettema GJ (1996) Mechanical efficiency and efficiency of storage and release of series elastic energy in skeletal muscle during stretch-shorten cycles. *J Exp Biol* 199: 1983-1997.
27. Ettema GJ (2001) Muscle efficiency: the controversial role of elasticity and mechanical energy conversion in stretch-shortening cycles. *Eur J Appl Physiol* 85: 457-465.
28. Marsh RL (1999) How muscles deal with real-world loads: the influence of length trajectory on muscle performance. *J Exp Biol* 202: 3377-3385.
29. Pennycuik CJ (1964) Frog Fast Muscle. 3. Twitches with Isometric and Inertial Load. *J Exp Biol* 41: 273-289.
30. Baratta RV, Solomonow M, Zhou BH (1998) Frequency domain-based models of skeletal muscle. *J Electromyogr Kinesiol* 8: 79-91.

31. Richards CT, Clemente CJ (2012) A bio-robotic platform for integrating internal and external mechanics during muscle-powered swimming. *Bioinspir Biomim* 7: 016010.
32. Farahat W, Herr H (2005) An apparatus for characterization and control of isolated muscle. *IEEE Trans Neural Syst Rehabil Eng* 13: 473-481.
33. Farahat WA, Herr HM (2010) Optimal workloop energetics of muscle-actuated systems: an impedance matching view. *PLoS Comput Biol* 6: e1000795.
34. Clemente CJ, Richards C (2012) Determining the influence of muscle operating length on muscle performance during frog swimming using a bio-robotic model. *Bioinspir Biomim* 7: 036018.
35. Ogata K (2003) *System Dynamics*. Upper Saddle River, NJ: Prentice Hall.
36. Azizi E, Roberts TJ (2010) Muscle performance during frog jumping: influence of elasticity on muscle operating lengths. *Proc Biol Sci* 277: 1523-1530.
37. Robertson BD, Sawicki GS (2014) Exploiting elasticity: Modeling the influence of neural control on mechanics and energetics of ankle muscle-tendons during human hopping. *J Theor Biol* 353C: 121-132.
38. Josephson RK, Stokes DR (1999) Work-dependent deactivation of a crustacean muscle. *J Exp Biol* 202: 2551-2565.
39. Caiozzo VJ, Baldwin KM (1997) Determinants of work produced by skeletal muscle: potential limitations of activation and relaxation. *Am J Physiol* 273: C1049-1056.
40. Sandercock TG, Heckman CJ (1997) Force from cat soleus muscle during imposed locomotor-like movements: experimental data versus Hill-type model predictions. *J Neurophysiol* 77: 1538-1552.

41. Curtin NA, Gardner-Medwin AR, Woledge RC (1998) Predictions of the time course of force and power output by dogfish white muscle fibres during brief tetani. *J Exp Biol* 201: 103-114.
42. Maganaris CN, Paul JP (2000) Hysteresis measurements in intact human tendon. *J Biomech* 33: 1723-1727.
43. Raburn CE, Merritt KJ, Dean JC (2011) Preferred movement patterns during a simple bouncing task. *J Exp Biol* 214: 3768-3774.
44. Alexander RM (1997) Optimum Muscle Design for Oscillatory Movements. *Journal of Theoretical Biology* 184: 253-259.
45. Sheppard P, Sawicki GS, Roberts TJ. Power Augmentation in a Compliant Muscle-Tendon System; 2009 2009; State College, Pennsylvania.
46. Krishnaswamy P, Brown EN, Herr HM (2011) Human leg model predicts ankle muscle-tendon morphology, state, roles and energetics in walking. *PLoS Comput Biol* 7: e1001107.
47. Zajac FE (1989) Muscle and tendon: properties, models, scaling, and application to biomechanics and motor control. *Crit Rev Biomed Eng* 17: 359-411.
48. Farris DJ, Sawicki GS (2012) The mechanics and energetics of human walking and running: a joint level perspective. *J R Soc Interface* 9: 110-118.
49. Merritt KJ, Raburn CE, Dean JC (2012) Adaptation of the preferred human bouncing pattern toward the metabolically optimal frequency. *J Neurophysiol* 107: 2244-2249.
50. NICHOLS T (1992) STIFFNESS REGULATION REVISITED. *Behavioral and brain sciences* 15: 783-784.

CHAPTER 3: MORE IS NOT ALWAYS BETTER: MODELING THE EFFECTS OF ELASTIC EXOSKELETON ASSISTANCE ON UNDERLYING MUSCLE-TENDON DYNAMICS

Benjamin D. Robertson, Dominic J. Farris, Gregory S. Sawicki

As accepted for publication in Bioinspiration and Biomimetics

3.1 Abstract

Development of robotic exoskeletons to assist/enhance human locomotor performance involves lengthy prototyping, testing, and analysis. This process is further convoluted by variability in limb/body morphology and preferred gait patterns between individuals. In an attempt to expedite this process, and establish a physiological basis for actuator prescription, we developed a simple, predictive model of human neuromechanical adaptation to a passive elastic exoskeleton applied at the ankle joint during a functional task. We modeled the human triceps surea-Achilles tendon muscle tendon unit (MTU) as a single Hill-type muscle, or contractile element (CE), and series tendon, or series elastic element (SEE). This modeled system was placed under gravitational load and underwent cyclic stimulation at a regular frequency (i.e. hopping) with and without exoskeleton (Exo) assistance. We explored the effect that both Exo stiffness (k_{Exo}) and muscle activation (A_{stim}) had on combined MTU and Exo (MTU+Exo), MTU, and CE/SEE mechanics and energetics. Model accuracy was verified via qualitative and quantitative comparisons

between modeled and prior experimental outcomes. We demonstrated that reduced A_{stim} can be traded for increased k_{Exo} to maintain consistent MTU+Exo mechanics (i.e. average positive power (\bar{P}_{mech}^+) output) from an unassisted condition (i.e. $k_{Exo} = 0kN/m$). For these regions of parameter space, our model predicted a reduction in MTU force, SEE energy cycling, and metabolic rate (\bar{P}_{met}), as well as constant CE \bar{P}_{mech}^+ output compared to unassisted conditions. This agreed with previous experimental observations, demonstrating our model's predictive ability. Model predictions also provided insight into mechanisms of metabolic cost minimization, and/or enhanced mechanical performance, and we concluded that both of these outcomes cannot be achieved simultaneously, and that one must come at the detriment of the other in a spring-assisted compliant MTU.

3.2 Introduction

In the last two decades, significant progress has been made towards developing functional wearable robotic devices to assist/enhance human locomotion [2]. The majority of these devices rely on powered actuation to effectively assist the wearer through a conventional rigid [3-8] or (more recently) soft/elastic [9] robotic interface. Unfortunately, powered devices are either restricted to a laboratory setting [5,7,8], or carry a significant added mass penalty [3,4,6,9], which offsets most, if not all, of the mechanical/energetic benefit the device may provide. Recently, however, there has been a shift towards

development of unpowered passive (i.e. spring driven) exoskeletons, as these devices can provide increased limb/joint stiffness/torque with minimal added mass penalty [10-12].

The rationale underlying application of springy actuators for locomotion assistance is not limited to decreasing device weight and power consumption, it also makes sense from a mechanical perspective. Humans employ “bouncing” gait patterns during walking, running, and hopping; and it has been demonstrated that the center of mass mechanics in each of these modes of gait can be predicted by treating the leg as a simple spring-loaded inverted pendulum [13-16]. Elastic mechanics are not exclusive to the whole limb to whole limb behavior, and there are multiple reports of muscle level mechanics that facilitate energy storage and return in series compliant tissues (e.g. tendon and aponeurosis) spanning the ankle joint during walking [17-21], running [17-20], hopping [1,22], and bouncing [23,24]. Given the “spring-like” behavior at the whole limb and joint level, passive exoskeleton actuation is uniquely well-suited to integration with existing limb mechanics.

There have been several studies that illustrate the effectiveness of springy actuators for assisting functional movement [1,22,25-27]. Grabowski and Herr [2] demonstrated that a spring-actuated exoskeleton spanning all three joints of the lower limb could reduce the metabolic demands of hopping in place. Their study participants achieved this by reducing biological contributions to limb stiffness and utilizing the parallel springs for energy storage and return; all while keeping center of mass and whole-limb plus exoskeleton mechanics consistent with limb mechanics observed during unassisted hopping [26].

Similar studies conducted with springy exoskeletons spanning only the ankle demonstrated that this effect scales, and that humans modulate muscle activation and biological stiffness to maintain joint-level and whole limb stiffness [27]. Plantar-flexor muscle groups generally decrease activation levels when assistance is provided by a wearable device, thereby reducing force production [1,22,25,27]. This ultimately affects the function of series compliant tissues (e.g. tendon, aponeurosis) known to cycle large amounts of energy during bouncing gait [13,17-21,23,28,29].

A recent muscle-level ultrasound study demonstrated that a spring assisted exoskeleton facilitated decreased soleus muscle force production in conjunction with increases in soleus fascicle excursion [1]. This had a net effect of maintaining a constant level of muscle average positive mechanical power (\bar{P}_{mech}^+) output. The Achilles tendon, however, experienced a large decrease in energy cycling which ultimately resulted in reduced MTU \bar{P}_{mech}^+ [1]. Despite this, it has been demonstrated that these “detuned” mechanics can result in reduced metabolic rates [1,22]. These reductions only hold to a point, though. As Grabowski et. al. demonstrated, more exoskeleton stiffness can decrease (or even eliminate) the metabolic benefits of a spring-actuated exoskeleton [26].

While it is clear that some exoskeleton assistance can be beneficial [1,22,26], and too much can be counterproductive or even detrimental [26], very little has been done to examine how muscle architecture and system mechanics can be *optimally* assisted by a springy actuator. For this to be possible, a broader understanding of how exoskeleton stiffness (k_{Exo}) impacts neuromechanical and energetic function at the muscle level is required. With this in

mind we present a simplified model of the triceps surae-Achilles tendon complex with parallel spring-actuated assistance during simulated human hopping. Based on previous findings from human studies, we predicted our model would **(1)** be able to trade reduced muscle activation for increased k_{Exo} to maintain system (i.e. MTU+Exo) level stiffness and \bar{P}_{mech}^+ production [27]. Given constant MTU+Exo \bar{P}_{mech}^+ output but increasing spring stiffness, we predicted **(2)** increased \bar{P}_{mech}^+ output from the Exo component, as well as decreased output from the MTU and SEE components of the biological system would occur with increasing k_{Exo} [1,22,25,26]. Despite reductions in loading of biological components with increasing k_{Exo} , we hypothesized that **(3)** the CE would maintain constant \bar{P}_{mech}^+ output by increasing its excursion in conjunction with reduced force [1]. Finally, we predicted that **(4)** these changes in system and component level mechanics would ultimately result in a reduced metabolic burden when springy assistance is provided [1,22,26].

3.3 Methods

3.3.1 Hopping as a Model of Functional Ankle Mechanics

We chose to model hopping in this study because it is a primarily ankle driven mode of bouncing gait that is simple both mechanically, and from a neural control perspective [22,30]. Despite its inherent simplicity, however, hopping captures one of the critical features of all bouncing gait: the ability to store and return energy in series tendon at distal joints [1,23]. Using hopping as a model of functional ankle joint mechanics allows us to ask

fundamental questions concerning the impact of passive exoskeleton assistance on the mechanics and energetics of biological muscle-tendon unit in a simple, straightforward way. Finally, hopping comes with a wealth of experimental whole limb [26,27], joint-level [22,25-27], muscle level [1], electromyographic [1,22,25], and metabolic [1,22,26] data to compare model predictions against.

3.3.2 Biological Muscle Tendon Unit Model

Our modeled Muscle-Tendon Unit (MTU) consisted of a single Hill-type contractile element (CE) subject to non-linear force-length (F-L) and –velocity (F-V) actuation dynamics (**fig. 1**); as well as first order activation dynamics. It also had a parallel elastic element (PEE) capable of generating passive force at lengths greater than l_0 , the length at which active muscle produces its peak isometric force [31] (**fig. 1**). Parameterization of normalized F-L characteristics was based on experimental observation in Rubenson et. al. [32]. Normalized F-V and first order activation dynamics were based on parameterized equations from Haeufle et. al [33]. Tendon/series elastic element (SEE) dynamics were modeled based on observations from Lichtwark et. al. [19], and exhibited a non-linear “toe” region, after which dynamics can be approximated as linear. All model equations and parameter values used here are detailed in supplementary text.

3.3.3 Inertial Environment

System inertial mechanics were modeled by assuming a single rigid attachment point of the biological MTU and exoskeleton (Exo) system to lever arm acting with a fixed mechanical advantage (EMA) on a point mass under constant gravitational load. This was

meant to reflect loading experienced by the triceps-surae-Achilles tendon complex at the ankle joint during human hopping (**fig. 1**). Rationale and justification for using this simplified inertial environment are discussed further in Robertson et. al. [34].

3.3.4 Model Simplifications

Several key simplifications were made to facilitate implementation of this modeling framework. First, the gastrocnemii and soleus muscle of the triceps surae-Achilles tendon complex were lumped into a single, mono-articular, fusiform muscle. This facilitated use of a simplified limb geometry, and disregards complications that arise from having biarticular and bipennate, (i.e. non-fusiform) gastrocnemii muscles (**fig. 1**). While, based on physiological cross-sectional area, soleus is the primary force producer within the triceps surae muscle group, these simplifications likely diminished the potential impact that gastrocnemii operating point and architecture played in governing adaptation at the ankle and knee in humans during spring assisted hopping [1,22]. Secondly, our system operates with a fixed mechanical advantage, disregarding shifts in biological moment arm length that can occur in-vivo [35,36]. Finally, all muscle fibers were assumed to have identical activation/deactivation time constants (τ_{act} and τ_{deact} respectively), and values used in first order activation dynamics are a weighted average of observed values based on muscle physiological cross-sectional area (PCSA) in cadavers [37-39]. Further justification of model simplifications can be found in Robertson et. al. [34].

3.3.5 Modeled Exoskeleton

Our model of human hopping with exoskeleton assistance had a linear tension spring in parallel with the biological MTU (**fig. 1**). The slack length of our modeled exoskeleton was the combined length at which the inactive CE develops passive force (l_0), and slack length of SEE complex (l_{slack}). The exoskeleton moment arm length is the same as that of the biological MTU ($l_{in} = 0.04m$) [37]. This was done to simplify scaling of relative Exo/MTU stiffness relationships explored in this study. We note that stiffness comparisons can be extended to systems where exoskeleton and biological moment arms are not equal by converting linear stiffness (N/m) to rotational stiffness ($N * m/rad$) using the following relationship:

$$k_{\theta} = k_x * (l_{in})^2$$

Where k_{θ} is rotational stiffness, k_x is linear stiffness, and l_{in} is the distance from the point where force is applied to the center of joint rotation (i.e. moment arm) (**fig. 1**). Finally, transmission of assistive forces was presumed to be ideal, and no attempt was made to model interaction of rigid exoskeleton with soft tissue.

3.3.6 Experimental Protocol

The model stimulation frequency (ω_{stim}) was 2.5 Hz, a frequency at which metabolic cost was consistently reduced in human experiments examining exoskeleton assisted hopping [1,22,26]. k_{Exo} was varied in 4.5 kN/m (2.5% k_{SEE}) increments from unassisted ($k_{Exo} = 0 N/m$) to that of biological tendon ($k_{SEE} = 180 kN/m$), corresponding to joint level stiffness during perfectly isometric unassisted hopping (i.e. $k_{MTU} = k_{SEE}$). Stimulation was

provided as a square wave pulse 10% duty relative to ω_{stim} (i.e. $T_{pulse} = .1 * \omega_{stim}^{-1}$). This pulse was subject to first order activation dynamics exhibited by biological muscle [31]. Stimulation amplitude (A_{stim}) ranged from 10-100% of maximum possible. All modeled conditions were run for 15 seconds (~37 hops) to allow time for the system to become stable and cyclic. For each A_{stim}/k_{Exo} combination, the final 4 complete hopping cycles were used in all subsequent analysis. Parameter values and equations used in model implementation are detailed in supplementary material.

3.3.7 Experimental Metrics

The major criterion for a simulation to successfully “hop” included having a flight phase where the MTU+Exo system went slack, and the only force applied to our virtual mass was gravity (i.e. $F_{net} = F_g$). Potential risk of injury was also taken into account as part of determining a successful hop, and normalized peak CE strains (ϵ_{peak}) $> .3$ were assumed to pose significant risk of injury based on reports from literature [40-42]. ϵ_{peak} was computed as follows:

$$\epsilon_{peak} = \frac{\left(\max_{t=0 \rightarrow T_{stim}} (l_{CE}(t)) - l_0 \right)}{l_0}$$

Where the cycle period $T_{stim} = \omega_{stim}^{-1}$ and $l_{CE}(t)$ is CE length as a function of time. Finally, successful hopping was required to be cyclic with stimulation, and show no variance when subjected to the integrated return map method detailed in [34].

Once it had been determined that a given condition meets the criterion for hopping in a safe and effective manner, system and component level analysis of mechanics and

energetics was performed. First, we determined average positive power over a cycle of hopping for the system (i.e. MTU+Exo) and its respective mechanical components (i.e. MTU, active/passive CE, SEE, Exo) as follows:

$$\bar{P}_{mech}^+ = \frac{1}{T_{stim}} * \int_{t=0}^{T_{stim}} P_{mech}^+(t) dt$$

Where

$$P_{mech}^+(t) = \begin{cases} 0 & \text{when } v(t) > 0 \\ P_{mech}(t) & \text{when } v(t) < 0 \end{cases}$$

In other words, power output was positive for shortening (i.e. work done against gravity).

Next, we explored system peak force (F_{peak}) over a cycle of hopping:

$$F_{peak} = \max_{t=0 \rightarrow T_{stim}} (F_{MTU+Exo}(t)) = F_{MTU+Exo}(t_{peak})$$

Where $F_{MTU+Exo}(t)$ is MTU+Exo force as a function of time, and t_{peak} is the time point within a cycle where peak system (MTU+Exo) force occurs. We were also interested in how the MTU, Exo, and active/passive CE components are shared loads at t_{peak} and computed their respective forces as well.

We were also concerned with how CE F-L and F-V dynamics influenced system mechanics, so we computed the range and average operating strains/velocities from stimulation onset (muscle activation, $\alpha(t) > 0$) to the initiation of flight ($F_{MTU+Exo}(t) = F_g$). Note that this does not include any passive stretch prior to stimulation onset, and only encompassed portions of ground contact where *active* muscle was likely to make significant contributions.

We were also interested in system energetics, and calculated average metabolic rate (\bar{P}_{met}) using a dimensionless model of metabolic cost [43,44] as a function of muscle velocity scaled by physiological constants F_{max} (the maximum active isometric CE force), v_{max} (maximum CE shortening velocity), (supplemental text **table 1**), and normalized muscle active state $\alpha(t)$ [45]. \bar{P}_{met} was computed as follows:

$$\bar{P}_{met} = \frac{1}{T_{stim}} * F_{max} * v_{max} * \int_{t=0}^{T_{stim}} [\alpha(t) * p_{met}(v_{CE}(t))] dt$$

where $p_{met}(v_{CE}(t))$ is dimensionless metabolic cost at time t from [43] (supplemental text **table 2**). MTU+Exo, MTU, and CE apparent efficiency (e_{app}) were also a focus of this study, and were computed as follows based on their respective \bar{P}_{mech}^+ output:

$$e_{app} = \bar{P}_{mech}^+ / \bar{P}_{met}$$

Further details on equations, metrics, and constants used as part of model implementation and subsequent analysis can be found in supplementary text.

3.3.8 Comparison to Experimental Data

Experimental data used in all quantitative comparisons made here was taken from Farris et. al. [22]. Exoskeleton rotational stiffness used in experimental conditions was $91N * m/rad$ which, when scaled by our modeled biological “in” moment arm ($0.04m$) [37] and converted to kN/m yields $\sim 56kN/m$. We constrained our selection of points based on experimental conditions (i.e. unassisted/ $k_{Exo} = 0kN/m$ and assisted/ $k_{Exo} \approx 54000kN/m$), and matched MTU+Exo and MTU average positive power to experimental data for the whole ankle joint with and without an exoskeleton [22]. We selected these two metrics as a basis

for comparison because our simplified model does not have the necessary geometric/physiological complexity for quantitative comparisons to muscle level data observed in [1].

3.4 Results

3.4.1 Stability, Injury Risk, and Flight Phase

For all modeled conditions, stable and cyclic mechanics were easily achieved within the time allotted, and the final 4 cycles used in analysis are all representative of steady-state behavior. Significant risk of injury was observed for low A_{stim} , low k_{Exo} combinations. These regions exhibited CE peak eccentric strains > 0.3 at some point in their hopping cycle (**fig. 2A**) [40-42].

A flight phase was achieved for the majority of the parameter space, with notable exceptions for low A_{stim} ($< 20\%$ of max) low k_{Exo} ($< 20\%k_{SEE}$) combinations, as well as low-to-medium A_{stim} ($\sim 50\%$ of max) and high k_{Exo} ($> \sim 50\%k_{SEE}$) conditions. The greatest flight amplitude was observed at 70% A_{stim} and high k_{Exo} ($> 70\%k_{SEE}$) conditions (**fig. 2B**). Regions where elevated injury risk or no flight phase was achieved are indicated by opaque regions labeled “Injury Risk” and “No Flight” in **figure 2A** and **2B** respectively and all subsequent contour plots (**fig. 3A,C, 6A-C**).

3.4.2 Average Positive Power

Maximal MTU+Exo \bar{P}_{mech}^+ was generated for high A_{stim} , high k_{Exo} conditions (**fig. 3A**). Minimums in MTU+Exo \bar{P}_{mech}^+ were generally observed for low stimulation amplitudes regardless of k_{Exo} (**fig. 3A**). Data points from a contour of constant Exo+MTU \bar{P}_{mech}^+ spanning 100% A_{stim} with no exoskeleton (i.e. $k_{Exo} = 0kN/m$) through 50% A_{stim} and an $k_{Exo} = 90 kN/m$ (i.e. $k_{Exo} = 50\%k_{SEE}$) were selected for further analysis, and are indicated by white dots in all subsequent contours (**fig. 3A**). MTU + Exo workloops from data during ground contact were generated for these selected points and are visualized in **figure 3B**.

In general, CE \bar{P}_{mech}^+ was highest for low A_{stim} /high k_{Exo} combinations along the border of the “no flight” region (**fig. 3C**), and lowest for high A_{stim}/k_{Exo} conditions where a flight phase was safely achieved (**fig. 3C**). Ground contact CE workloops for selected points from **figure 3A** are visualized in **figure 3D**.

3.4.3 Force and Power Sharing

Selected points of constant MTU+Exo \bar{P}_{mech}^+ (**fig. 3A**) traded energy cycled in biological tendon for energy cycled in the modeled exoskeleton, dramatically reducing $F_{MTU}(t_{peak})$ and \bar{P}_{mech}^+ from the biological MTU (**fig. 4**). Maintaining constant MTU+Exo \bar{P}_{mech}^+ as in **figure 3A** required a slight increase in MTU+Exo F_{peak} while simultaneously decreasing the force burden on the biological MTU (**fig. 4A**). Despite reduced $F_{MTU}(t_{peak})$ with increased k_{Exo} for selected data points, there was a small increase in contributions to

F_{peak} from passive CE components (**fig. 4A**). This had little effect on CE \bar{P}_{mech}^+ , which remained nearly constant for these same points in parameter space. CE power actually *increased* slightly from baseline (unassisted, $k_{Exo} = 0 \text{ kN/m}$) to high k_{Exo} , low A_{stim} conditions for selected points of constant MTU+Exo \bar{P}_{mech}^+ (**fig. 4B**).

3.4.4 Force-Length and Force-Velocity Dynamics

Force-length (F-L) and -velocity (F-V) operating points during active force production for data points selected in **3A** can be seen in **figure 5**. As A_{stim} decreased and k_{Exo} increased, the modeled CE increased its range of operating lengths as well as average values of both operating length and velocity (bars, **fig. 5**). Average operating strain increased from approximately $-.10$ to $.15l_0$ ($\sim 4.9\text{-}6.3 \text{ cm}$) (markers, **fig. 5A**), while average operating velocity more than doubled from $\sim 0.7 - 0.16 v_{max}$ ($\sim 3\text{-}7 \text{ cm/s}$) (markers, **fig. 5B**).

3.4.5 Metabolic Rate and Efficiency

Average metabolic rate scaled almost directly with A_{stim} /integrated muscle activation (**fig. 6A**), but there was a slight increase in \bar{P}_{met} when A_{stim} was held constant and k_{Exo} was increased (**fig. 6A**). For the data points of constant MTU+Exo \bar{P}_{mech}^+ selected in **figure 3A**, \bar{P}_{met} decreased with decreasing A_{stim} and increasing k_{Exo} (**fig. 6A**).

MTU e_{app} decreased with decreasing A_{stim} except in low-to-no k_{Exo} conditions (**fig. 6B**). MTU e_{app} also decreased as k_{Exo} increased unless A_{stim} was $\geq 90\%$ of maximum, at which point it increased slightly from unassisted (**fig. 6B**). For the data points selected in **figure 3A**, MTU e_{app} declined rapidly with decreasing A_{stim} and increasing k_{Exo} (**fig. 6B**).

CE e_{app} (active + passive components) generally decreased with increasing k_{Exo} , and increased with decreasing A_{stim} (**fig 6C**). For the data points selected in **figure 3A**, CE e_{app} increased with decreased A_{stim} and increased k_{Exo} (**fig. 6C**).

3.4.6 Experimental Comparison

An MTU \bar{P}_{mech}^+ of ~ 2.4 W/kg was observed for the 60% A_{stim} , $k_{Exo} = 0$ condition, and output ~ 1.7 W/kg was observed for the 50% A_{stim} , 30% k_{SEE} (i.e. $k_{Exo} = 54kN/m$) condition, matching findings for whole ankle \bar{P}_{mech}^+ in previous human studies [22] (**fig. 7A**). These conditions are highlighted on most contour plots by a white star (**fig. 3A,C, 6A-C**), and compared directly in **figure 7**. Similarities between experimental and modeled conditions include little to no change in P_{mech}^+ for the CE, large reductions in \bar{P}_{mech}^+ for both the SEE and whole MTU, with a considerably greater fraction of MTU \bar{P}_{mech}^+ coming from the CE (**fig. 7A**), and a reduction in \bar{P}_{met} (**fig. 6A**) when springy assistance was provided. There are also strong qualitative similarities in the time-course of MTU/MTU+Exo force production and MTU/CE excursion dynamics during ground contact (**fig. 7B,C**). The major difference between modeled/experimental data had to do with rate of force onset/offset (**fig. 7B**) and CE excursion (**fig. 7C**) in late/early stance.

3.5 Discussion and Conclusions

The intention of this study was to use a simple neuromechanical model to understand the impact of springy exoskeleton assistance at the ankle joint. Model predictions agreed

well with observation from experimental studies, and provided ample insight into muscle-level mechanisms of neuromechanical and energetic adaptation during spring-assisted hopping [1,22,25-27]. Based on model results, we were able to provide general insight into factors influencing system performance, as well as limitations on the benefits a passive device can ultimately provide.

3.5.1 MTU+Exo Mechanics

Based on observations from previous experimental studies we hypothesized that by increasing exoskeleton stiffness and reducing stimulation amplitude, our model system (MTU+Exo) would be able to maintain a constant \bar{P}_{mech}^+ output and “stiffness” from an unassisted condition [22,25-27]. Model findings agreed with this hypothesis, and it was possible to start at any stimulation level $\geq 60\%$ without exoskeleton assistance, and maintain \bar{P}_{mech}^+ production by decreasing A_{stim} and increasing k_{Exo} (**fig. 3A**). By following any one of these contours, it was observed that there were nearly identical force-displacement (e.g. “stiffness”) dynamics during stance as demonstrated by MTU+Exo workloops from selected points in **figure 3A (fig. 3B)**.

3.5.2 MTU and SEE Mechanics

Our second hypothesis was that, by following a contour of constant MTU+Exo \bar{P}_{mech}^+ , there should be a reduced MTU forces at t_{peak} as well as a decrease in SEE and MTU contribution to MTU+Exo \bar{P}_{mech}^+ [1,22,25-27]. By examining **figure 4**, it can be seen that this is indeed the case. As k_{Exo} is increased and A_{stim} decreased, contributions to peak MTU+Exo force from MTU were reduced, while those from Exo increased (**fig. 4A**). A

similar trend emerges for power sharing, where reductions in MTU/SEE \bar{P}_{mech}^+ are offset by increased output from the Exo (**fig. 4B**). Given that the ankle plantar flexor muscle groups depend primarily on inertial dynamics and elastic energy cycling as a means for joint level \bar{P}_{mech}^+ generation [1,17,23], it follows that reduced loading results in reduced \bar{P}_{mech}^+ production in the SEE and MTU as a whole.

3.5.3 Muscle Mechanics

Our third hypothesis predicted that, in spite of reduced biological loading, average positive power in the CE would remain constant. The predicted mechanism by which this would occur was increased excursions in conjunction with reduced CE forces, which would result in nearly constant CE average positive power production [1]. By examining **figure 4B**, it can be seen that, as A_{stim} was decreased and k_{Exo} increased, CE \bar{P}_{mech}^+ remained nearly constant, and even increased slightly for $k_{Exo} > \sim 20\%k_{SEE}$ ($\sim 36kN/m$) conditions (**fig. 3C, 4B**). Our model also predicted that this occurred in conjunction with reduced biological loading (**fig. 4A**) as well as increased CE excursion (**fig. 3D, 5A**) and average operating velocity (**fig. 5B**) in full agreement with hypothesis (3). Increased excursions also occurred in conjunction with greater values of ϵ_{peak} , many of which were > 0 (i.e. $l_{CE} > l_0$) (**fig. 2A, 5A**), resulting in passive CE force generation (**fig. 4A**). This coupling of force generation to CE length also played a role in keeping CE \bar{P}_{mech}^+ at near constant levels (**fig. 4B**).

3.5.4 Energetics of Assisted Hopping

For our fourth and final hypothesis, we predicted that by following a contour of constant MTU+Exo \bar{P}_{mech}^+ it would be possible to reduce \bar{P}_{met} from the unassisted condition

[22,26]. Following the contour of white dots from **figure 3A**, increasing k_{Exo} required a reduction in A_{stim} , which was the primary determinant of \bar{P}_{met} for our modeled data (**fig. 6A**). This was in spite of greater average operating velocities (**fig. 5B**), and no reduction in \bar{P}_{mech}^+ output from the CE (**fig. 3B, 4B**).

Contours of constant MTU+Exo \bar{P}_{mech}^+ in **figure 3A** all ran into the same problem as k_{Exo} increased and A_{stim} decreased: there came a point where the system was no longer capable of hopping. In these conditions, the mechanical response of biological and exoskeleton model components to cyclic stimulation was such that they counteracted each other, resulting in force and power production dynamics that did not facilitate a flight phase (**fig. 2B**). In order to achieve hopping behavior at higher values of k_{Exo} it became necessary to raise A_{stim} , and ultimately increase \bar{P}_{met} (**fig. 3A, 6A**). This outcome was in line with observations from Grabowski et. al. (2009), which demonstrated that a more compliant exoskeleton achieved greater reductions in \bar{P}_{met} than a stiffer one [26]. Unfortunately, Grabowski et. al. did not record EMG as part of their study, so there is no way of knowing whether or not reduced metabolic benefit in stiffer exoskeletons was accompanied by increased muscle activation as predicted here [26].

Even though there were significant reductions in metabolic rate when A_{stim} was reduced in conjunction with increasing k_{Exo} , it did not make the biological system as a whole more efficient. In fact, it had the exact opposite effect (**fig. 6B**). By applying mechanical assistance and reducing the force burden on the MTU, the ability for an SEE to effectively cycle energy was reduced considerably (**fig. 4**). The ultimate result was a large decrease in

MTU apparent efficiency (**fig. 6B**) despite concomitant reductions in metabolic rate (**fig. 6A**).

This system level trend did not hold at the muscle level, and CE \bar{P}_{mech}^+ output remained constant as \bar{P}_{met} declined with increasing k_{Exo} (**fig. 4A**). This resulted in muscle e_{app} rising from $\sim 25\%$ in the unassisted condition to $\sim 40\%$ at the highest level of assistance for the data point in **figure 3A** ($50\%A_{stim}$, $k_{Exo} = 90kN/m$) (**fig. 6C**). This increased CE apparent efficiency, however, comes with greater ϵ_{peak} values/risk of injury (**fig. 2A**) and increased energy cycling in passive CE elements (**fig. 4B**).

3.5.5 Comparison of Modeled and Experimental Data

Despite the simplicity of the model implemented here, it can be compared rather nicely to human joint level data observed in Farris et. al. [1,22]. By constraining our k_{Exo} values based on those used in experimental studies, and sweeping our A_{stim} for values of MTU \bar{P}_{mech}^+ observed experimentally, we can identify a point of best fit for the exo with no spring ($A_{stim} = 70\%$ of max, $k_{Exo} = 0\%k_{SEE}$) and exo with spring ($A_{stim} = 50\%$ of max, $k_{Exo} = 30\%k_{SEE}$) conditions from [1,22] for hopping at 2.5 Hz (**fig. 7A**, stars in **fig. 3A,C, 6**). These points have a constant MTU+Exo \bar{P}_{mech}^+ (**fig. 3A**), reduced A_{stim} and \bar{P}_{met} requirements from unassisted (**fig. 6A**), and traded reduced CE force (**fig. 7B**) for increased excursion (**fig. 7C**) to keep \bar{P}_{mech}^+ constant (**fig. 3C**). Direct comparisons of muscle/tendon mechanics are difficult, since experimental data in *only* for the soleus MTU, and our model has all three plantarflexors lumped into a single monoarticular MTU. We do, however,

directly compare % of total \bar{P}_{mech}^+ from CE/SEE in both studies, and find a quantitative match easily within ± 1 Standard Error Measurement (SEM) of experimental data (**fig. 7A**).

There are, however, some shortcomings of model findings as well. Most notably, our model predicted significant passive CE stretch in early stance (**fig. 7C**). This was not observed in human studies, where the ability to actively modulate MTU position with antagonist muscles (i.e. tibialis anterior) and knee flexion likely work together to limit CE lengthening in early stance (**fig. 7C**). Secondly, while qualitative trends in metabolic demand agreed (i.e. \bar{P}_{met} reduced with Exo, **fig. 6A**), the model underestimated values of reductions in whole body metabolic cost attributed to reduced plantar-flexor loads from [1]. Again, this is likely attributable to model simplifications, which do not allow for bi-articular plantar flexors (i.e. medial and lateral gastrocnemii) that reduce knee joint mechanical demands in humans [22].

3.5.6 Conclusions and the Case for Optimal Exoskeleton Stiffness for Bouncing Gait

With all of these model predictions and simplifications in mind, the question now becomes one of optimization. How can metabolic benefits, MTU and CE efficiency, and risk of injury all be balanced to best assist a compliant MTU? Is there a point or region in parameter space where detrimental and beneficial aspects can be balanced to achieve an idealized outcome? We are confident that humans would follow a path through our parameter space that keeps Exo+MTU stiffness and average positive power nearly constant [27](**fig. 3A-B, 4A**), maintains near constant CE positive power [1] (**fig. 3C-D, 4A**), reduces

muscle activation [1,22,25], and allows for reduced metabolic energy consumption [1,22,26] (**fig. 6A**). A significant region of parameter space remains accessible even with these restrictive criteria in place, and all of these regions terminated at a point where flight is no longer achieved or injury risk is too great beyond some terminal increase in k_{Exo} /reduction in A_{stim} (**fig. 3A**). In every case, the only way to sustain hopping beyond this point was to increase A_{stim} in conjunction with increasing k_{Exo} , ultimately resulting in increased metabolic cost (**fig. 6A**) and average positive power from the MTU+Exo system (i.e. enhanced performance) (**fig. 3A**). This, again, agrees with observed trends in human data [26], and leads us to the conclusion that springy assistance will be optimized for metabolic benefit when muscle activation is minimized and MTU+Exo power/stiffness remains consistent with the baseline/unassisted condition.

This model also made a second interesting prediction: by increasing assistance beyond the point of optimal metabolic benefit, it was possible to obtain better mechanical performance (i.e. hop height, Exo+MTU positive power) than the biological system alone (**fig. 2B, 3A**). These regions of enhanced performance were also coincident with reduced CE positive power (**fig. 3C**) and injury risk (**fig. 2A**), as well as an increased metabolic cost relative to conditions where expenditure is minimized (**fig. 6A**). This agrees with observations from Grabowski et. al., where increased performance/hop height was also accompanied by greater variability in touchdown position, indicating that greater performance may come at the cost of reduced stability [26]. In conclusion, our model does

predict that metabolic and performance benefits can be achieved simultaneously, but that neither is likely to be optimal while the other persists in a compliant MTU.

3.6 Future Directions

Future modeling work will integrate simulated spinal cord reflex in conjunction with feed-forward control to further explore the possibilities and limitations of spring-based assistive exoskeletons. Given the variability of length, velocity, and biological force present in this study when assistance is applied, it is likely that at least one of these reflex pathways serves to govern unconscious neuromechanical adaptation to a wearable robotic device. By examining the interplay of reflex feedback, feed-forward control, and a wearable device, we hope to better understand how design of assistive devices may be optimized to achieve a desired outcome, be it reduced metabolic cost or enhanced performance. Future experimental work will include studies of human hopping for a range of exoskeleton stiffness' with instrumentation similar to Farris et. al. [1,22] to better understand neural and metabolic adaptation to springy exoskeletons, and either verify or refute predictions made here regarding tradeoffs between reductions in metabolic cost and enhanced mechanical performance.

3.7 Tables

Table 1, Model Parameters: Parameter values used in model implementation. *indicates half body mass.

Muscle Parameters (CE)	Value
F_{max}	6000 N [20,28,45]
v_{max}	-0.45 m/s [20,28]
l_0	0.055 m [19,20,46]
k_m	90,000 N/m [19]
Tendon Parameters (SEE)	Value
l_{slack}	.237 m [19,20]
k_t	180,000 N/m [19]
Activation Parameters	Value
τ_{act}	0.033 s [37,38]
τ_{deact}	0.091 s [37,38]
Pulse Duty	10.0%
Environment Dynamics	Value
g	9.8 m/s ²
$EMA (l_{in}/l_{out})$	0.33 [20]
M	35 kg*

Table 2, Model Equations: Equations and parameter values used in model implementation

Muscle Force Length	Equation	Values
$F_l \text{ active}$	$e^{- ((l_m/l_0)^b - 1)/s ^a}$ [47,48]	$b = .8698, s = .3914, a = 3.1108$
$F_l \text{ passive}$	$A * e^{(b*((l_m/l_0)-1))}$ [47,48]	$A = 2.38 * 10^{-2}, b = 5.31$
Muscle Force Velocity	Equation	Values
$F_v \text{ when } v_m > 0$	$(1 - (v_{CE}/v_{max}))/((1 + (v_{CE}/(k * v_{max}))))$ [33,49]	$k = .17$
$F_v \text{ when } v_m < 0$	$1.8 - 0.8 * ((1 + v_{CE}/v_{max})/(1 - 7.56 * (v_{CE}/(k * v_{max}))))$ [33,49]	$k = .17$
Tendon Stiffness	Equation	Values
k_{SEE}	$k_t * (1 + (0.9/-e^{((Q * F_{CE})/F_{max})}))$ [19]	$Q = 20$
Activation Dynamics	Equation	Values
$\alpha(t)$	$\int [(u(t)/\tau_{act}) - (1/\tau_{act}) * (\beta + (1 - \beta) * u(t))] dt$ [31]	$\beta = \tau_{act}/\tau_{deact}$
Metabolic Rate	Equation	Values
$p(v_{CE}) \text{ for } v_{CE} > 1$	$0.01 - 0.11(v_{CE}/v_{max}) + 0.06e^{(-8v_{CE}/v_{max})}$ [43]	-
$p(v_{CE}) \text{ for } v_{CE} > 1$	$.23 - .16e^{(-8v_{CE}/v_{max})}$ [43]	-

3.8 Figures

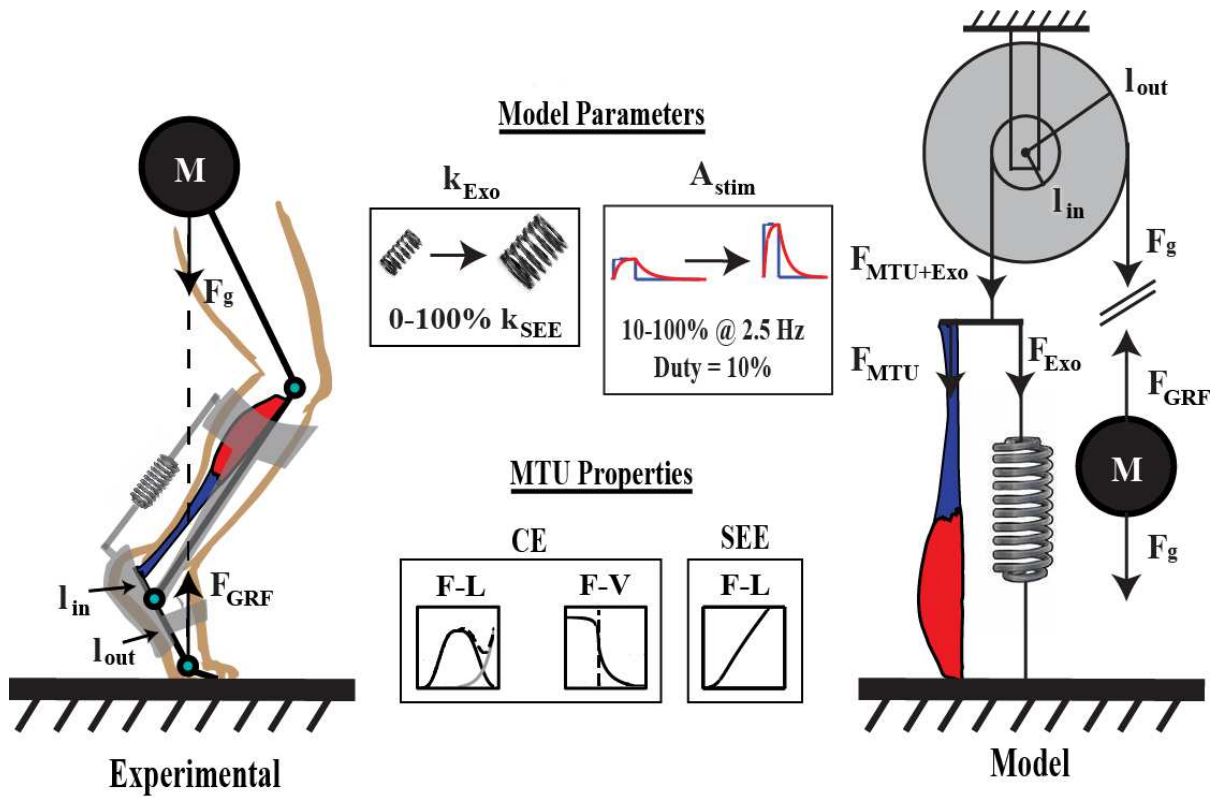


Figure 1, Model Schematic: Experimental (left) and modeled (right) exoskeleton assisted human hopping. Range of stimulation and exoskeleton parameters explored here, as well as CE/SEE actuation properties are indicated in boxes. The stim parameter acts on biological muscle, and k_{Exo} is the stiffness of the modeled parallel passive exoskeleton.

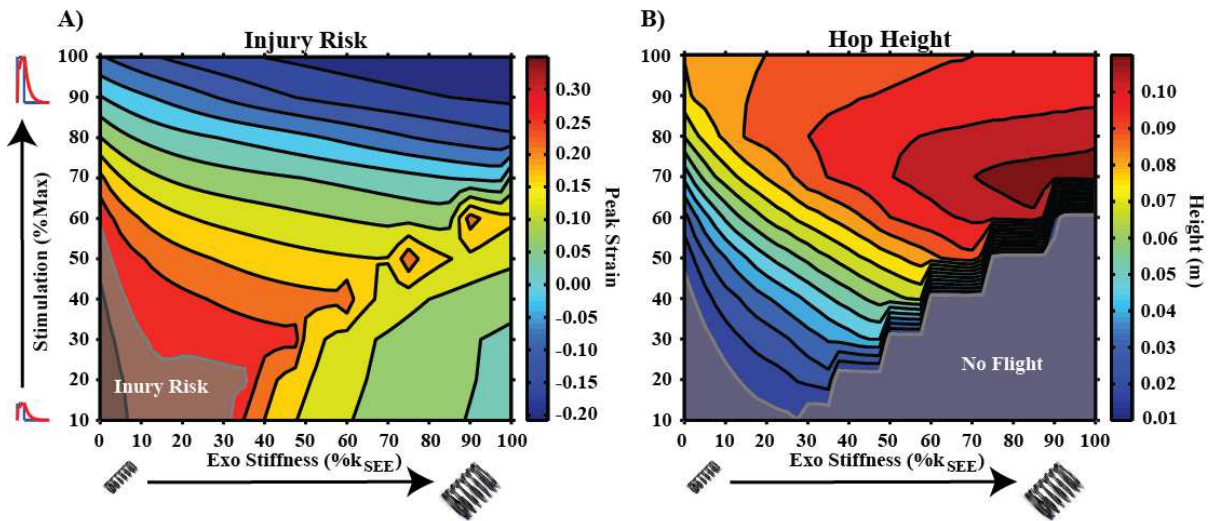


Figure 2, Injury Risk and Hop Height: A) Contour of peak eccentric strain over a cycle of hopping. Regions exceeding a value of 0.3 or greater were indicated by opaque region labeled “injury risk.” B) Contour of peak height achieved over a cycle of hopping. Regions where flight height ≈ 0 were indicated by the opaque region labeled “no flight.”

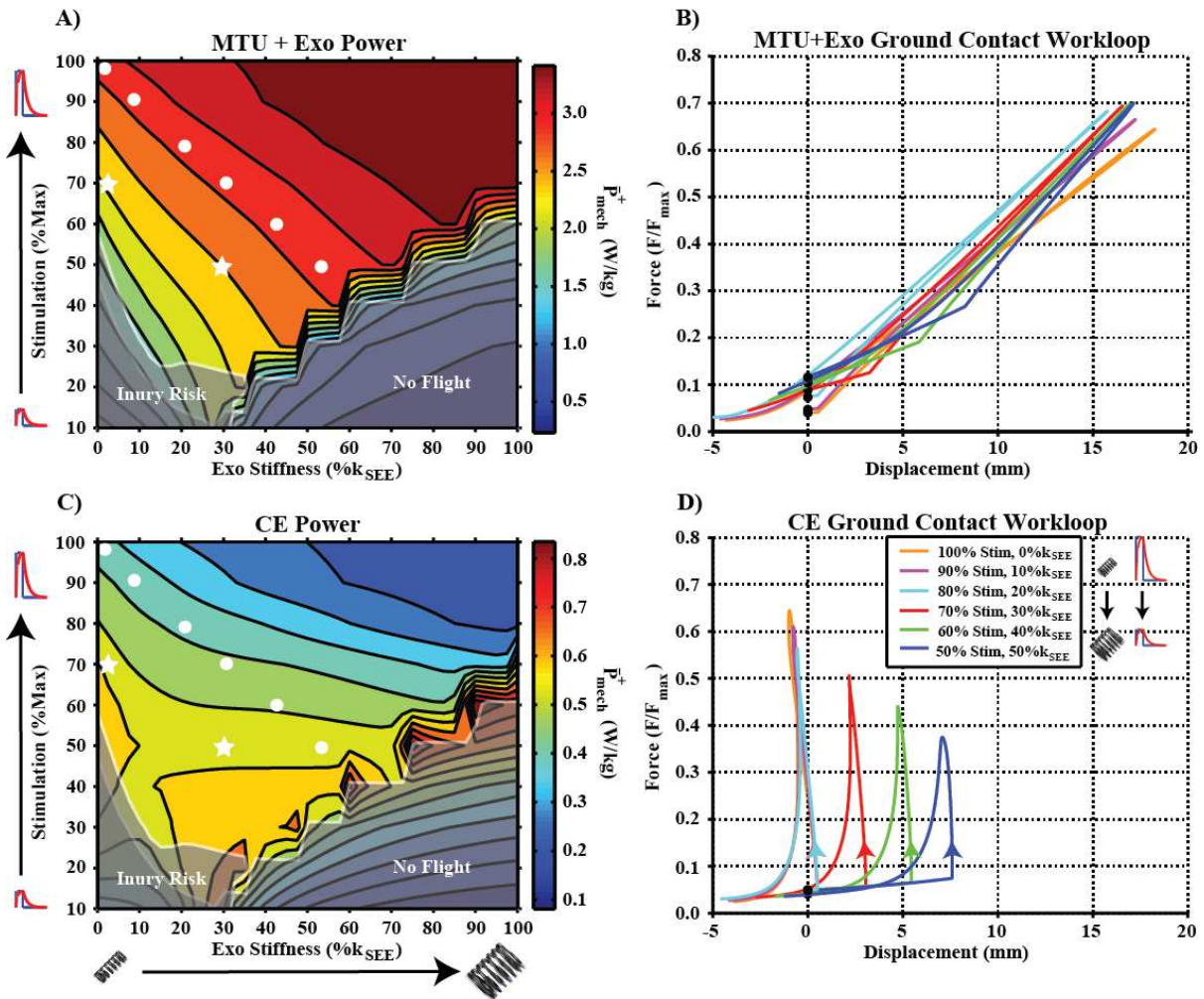


Figure 3, Average Power and Workloop Dynamics: **A)** Average positive power output for the combined MTU+Exo system. White dots in this and all subsequent contour plots indicate points in parameter space of equivalent MTU+Exo positive power. Stars represent points that correspond to joint level mechanics observed in [22].

Note that there were several contours which trade stimulation amplitude for Exo stiffness to achieve constant MTU+Exo positive power output. **B)** Workloops during ground contact (i.e. $F_{MTU+Exo} > 0$) for points in parameter space indicated by white dots in **3A**. The force-displacement profile (i.e. “stiffness”) in each case was nearly identical. **C)** Contour plot of average positive power produced by the CE (active + passive). **D)** CE workloops during ground contact for points in parameter space indicated by white dots. Positive power remained nearly constant by trading decreased force output for increased excursion.

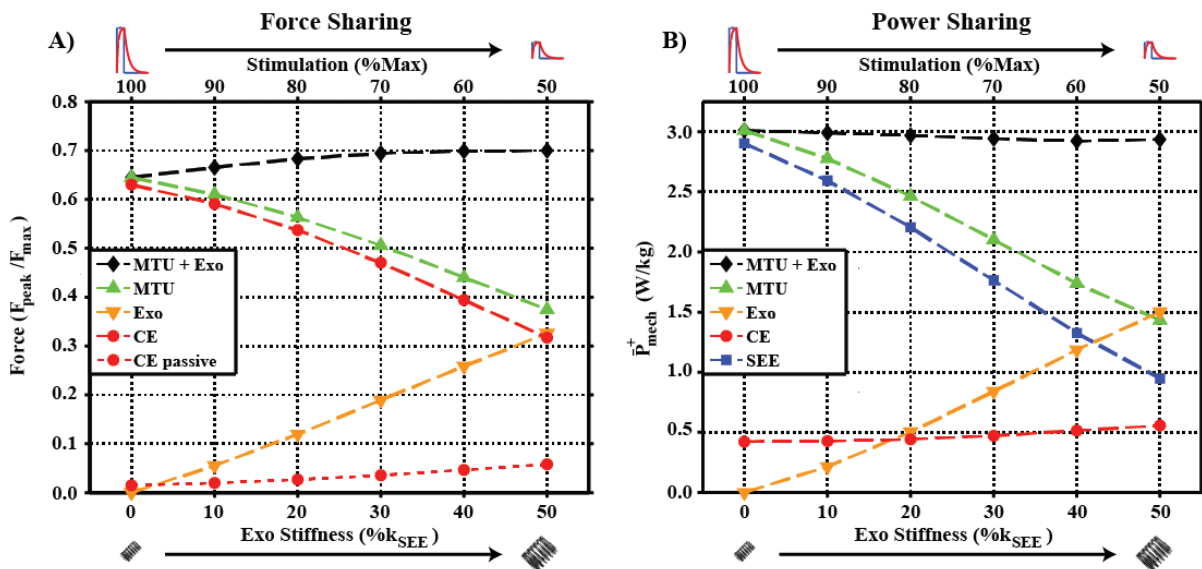


Figure 4, Force and Power Sharing: **A)** MTU+Exo peak force and system component contributions for points indicated by white dots in **figure 3A**. Biological components are unloaded as Exo contributions rise in conjunction with increased passive contributions from CE. **B)** Average positive power output from MTU+Exo and its components for the same points as in **4A**. System level power remains constant by trading MTU/SEE power output for energy cycled in Exo, while CE positive power remains nearly constant.

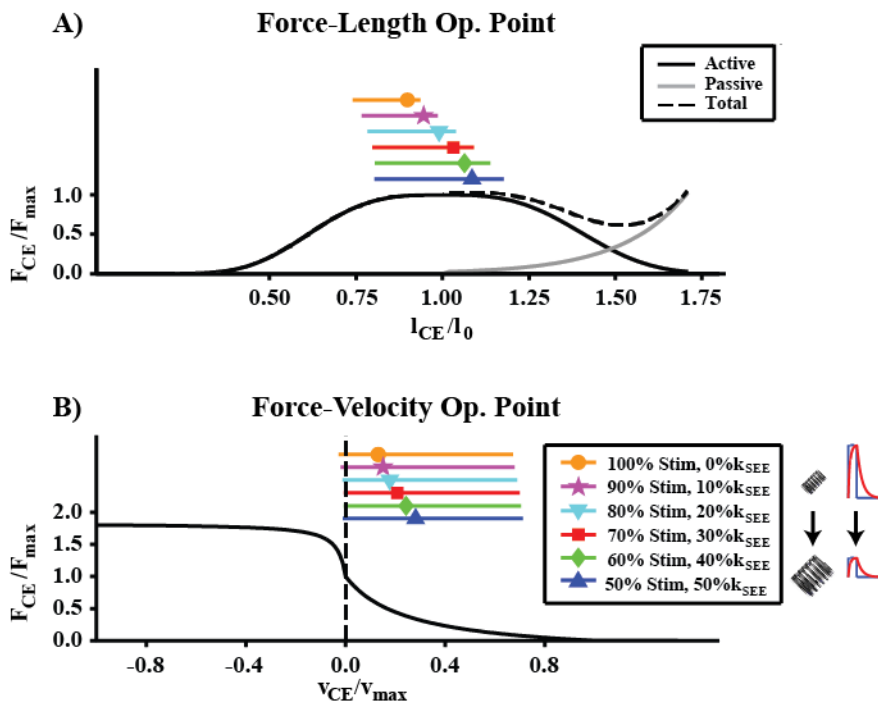


Figure 5, CE Operating Point: A) CE force-length operating point for points in parameter space indicated by white dots in **figure 3A**. B) CE force-velocity operating point for white dot points in **figure 3A**. In both figures, markers indicate average operating point, and bar indicates range of operating points. Both average and range of force-length and -velocity operating points increases as stimulation amplitude is decreased and Exo stiffness is increased to maintain constant MTU+Exo average positive power output.

Figure 6, Metabolic Rate and Apparent Efficiency: A)

Average metabolic rate for the modeled CE. Stimulation amplitude is primary factor governing metabolic cost, as indicated by horizontal contours.

B) Contour plot of MTU apparent efficiency. Note that any application of exoskeleton assistance results in reduced apparent efficiency except for stimulation amplitudes $\geq 90\%$.

C) Contour plot of CE apparent efficiency (passive + active). In general, decreasing stimulation amplitude increases CE apparent efficiency, and adding exoskeleton stiffness decreases CE apparent efficiency.

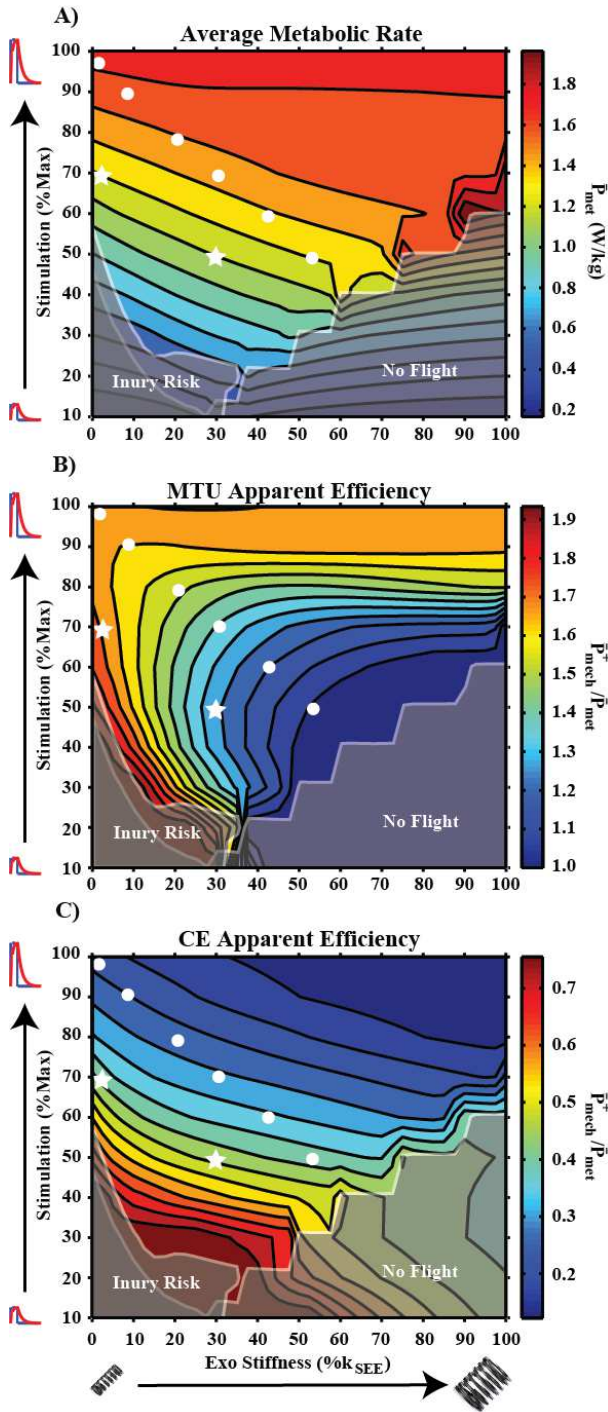
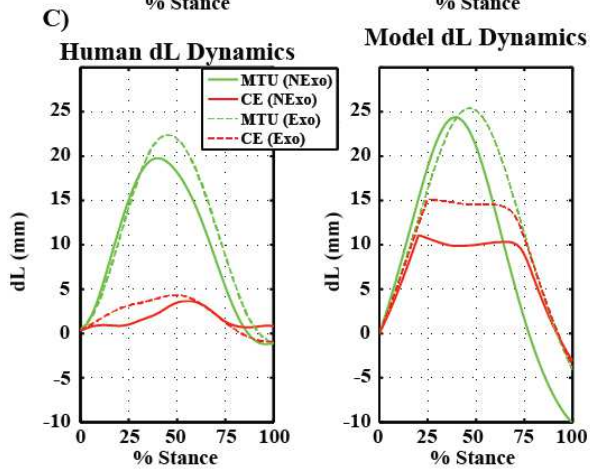
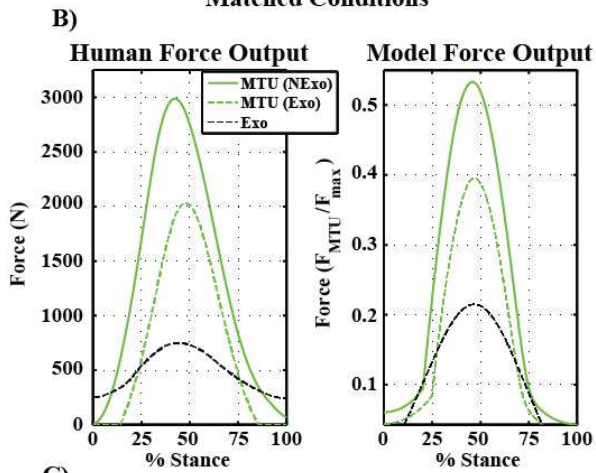
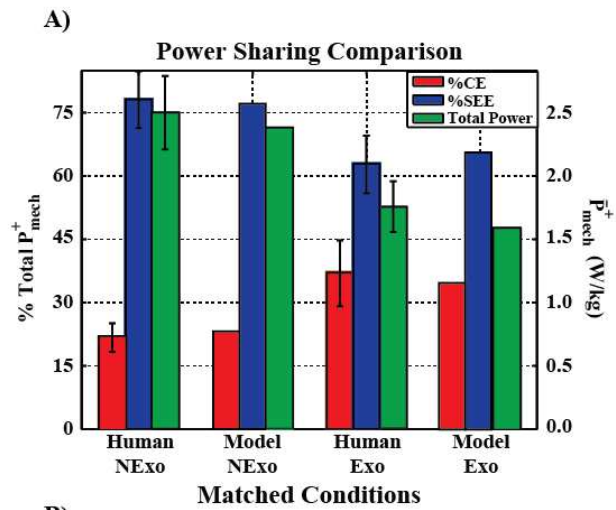


Figure 7, Comparison to Human Data: **A)** Comparison of Exoskeleton (Exo) and No Exoskeleton (NExo) conditions from [1] with appropriately matched model conditions (stars in **fig. 3A,C, 6A-C**). The left axis indicates percent contribution from CE/SEE to total MTU \bar{P}_{mech}^+ . The right axis is total ankle joint/MTU \bar{P}_{mech}^+ for experimental and model studies respectively. Note that an error bar indicating ± 1 SEM is on all experimental data, and that matched model data falls easily within this range of values. **B)** Human (left) and model (right) force vs. % stance for matched (star) conditions. Note comparable timecourse of force production for NExo and Exo conditions, as well as reductions in peak MTU force when exoskeleton assistance is applied. **C)** MTU and CE Excursion during stance for experimental (left) and matched model (right) Exo and NExo conditions. Note that both show increased MTU and CE excursion for the Exo condition due to increase CE excursion in early stance, as well as a shift in the timing of peak MTU length relative to stance time.



References

1. Farris DJ, Robertson BD, Sawicki GS (2013) Passive elastic exoskeletons reduce soleus muscle force but not work in human hopping. *J Appl Phys*.
2. Ferris DP (2009) The exoskeletons are here. *J Neuroeng Rehabil* 6: 17.
3. Kawamoto H, Lee S, Kanbe S, Sankai Y. Power Assist Method for HAL-3 using EMG-based Feedback Controller; 2003. pp. 1648-1653.
4. Zoss AB, Kazerooni H, Chu A (2006) Biomechanical design of the Berkley lower extremity exoskeleton (BLEEX). *IEEE/ASME Transaction on Mechatronics* 11: 128-138.
5. Ferris DP, Lewis CL (2009) Robotic lower limb exoskeletons using proportional myoelectric control. *Conf Proc IEEE Eng Med Biol Soc* 2009: 2119-2124.
6. Mooney LM, Rouse EJ, Herr HM (2014) Autonomous exoskeleton reduces metabolic cost of human walking during load carriage. *J Neuroeng Rehabil* 11: 80.
7. Hocoma.
8. Malcolm P, Derave W, Galle S, De Clercq D (2013) A simple exoskeleton that assists plantarflexion can reduce the metabolic cost of human walking. *PLoS One* 8: e56137.
9. Wehner M, Quinlivan B, Aubin PM, Martinez-Villalpando E, Baumann M, et al. A Lightweight Soft Exosuit for Gait Assistance; 2013 May 6-10, 2013; Karlsruhe, Germany.
10. Wiggins MB, Sawicki GS, Collins SH. An exoskeleton using controlled energy storage and release to aid ankle propulsion; 2011. pp. 1-5.

11. Hasegawa Y, Ogura K. First report on passive exoskeleton for easy running: PEXER IV; 2013; Nagoya. IEEE. pp. 1-6.
12. Elliot G, G.S. S, A. M, Herr H. The biomechanics and energetics of human running using an elastic knee exoskeleton; 2013.
13. Geyer H, Seyfarth A, Blickhan R (2006) Compliant leg behaviour explains basic dynamics of walking and running. *Proc Biol Sci* 273: 2861-2867.
14. Holt KG, Hamill J, Andres RO (1990) The Force-Driven Harmonic-Oscillator as a Model for Human Locomotion. *Human Movement Science* 9: 55-68.
15. Blickhan R (1989) The spring-mass model for running and hopping. *J Biomech* 22: 1217-1227.
16. Srinivasan M (2011) Fifteen observations on the structure of energy-minimizing gaits in many simple biped models. *J R Soc Interface* 8: 74-98.
17. Farris DJ, Sawicki GS (2012) Human medial gastrocnemius force-velocity behavior shifts with locomotion speed and gait. *Proc Natl Acad Sci U S A* 109: 977-982.
18. Lichtwark GA, Bougoulas K, Wilson AM (2007) Muscle fascicle and series elastic element length changes along the length of the human gastrocnemius during walking and running. *J Biomech* 40: 157-164.
19. Lichtwark GA, Wilson AM (2008) Optimal muscle fascicle length and tendon stiffness for maximising gastrocnemius efficiency during human walking and running. *J Theor Biol* 252: 662-673.
20. Lichtwark GA, Wilson AM (2007) Is Achilles tendon compliance optimised for maximum muscle efficiency during locomotion? *Journal of Biomechanics* 40: 1768-1775.

21. Fukunaga T, Kubo K, Kawakami Y, Fukashiro S, Kanehisa H, et al. (2001) In vivo behaviour of human muscle tendon during walking. *Proc Biol Sci* 268: 229-233.
22. Farris DJ, Sawicki GS (2012) Linking the mechanics and energetics of hopping with elastic ankle exoskeletons. *J Appl Physiol* 113: 1862-1872.
23. Takeshita D, Shibayama A, Muraoka T, Muramatsu T, Nagano A, et al. (2006) Resonance in the human medial gastrocnemius muscle during cyclic ankle bending exercise. *J Appl Physiol* 101: 111-118.
24. Dean JC, Kuo AD (2011) Energetic costs of producing muscle work and force in a cyclical human bouncing task. *J Appl Physiol* 110: 873-880.
25. Ferris DP, Bohra ZA, Lukos JR, Kinnaird CR (2006) Neuromechanical adaptation to hopping with an elastic ankle-foot orthosis. *J Appl Physiol* 100: 163-170.
26. Grabowski AM, Herr HM (2009) Leg exoskeleton reduces the metabolic cost of human hopping. *J Appl Physiol* 107: 670-678.
27. Chang YH, Roiz RA, Auyang AG (2008) Intralimb compensation strategy depends on the nature of joint perturbation in human hopping. *J Biomech* 41: 1832-1839.
28. Hof AL, Van Zandwijk JP, Bobbert MF (2002) Mechanics of human triceps surae muscle in walking, running and jumping. *Acta Physiol Scand* 174: 17-30.
29. Alexander RM (2002) Tendon elasticity and muscle function. *Comp Biochem Physiol A Mol Integr Physiol* 133: 1001-1011.
30. Farley CT, Morgenroth DC (1999) Leg stiffness primarily depends on ankle stiffness during human hopping. *J Biomech* 32: 267-273.
31. Zajac FE (1989) Muscle and tendon: properties, models, scaling, and application to biomechanics and motor control. *Crit Rev Biomed Eng* 17: 359-411.

32. Rubenson J, Pires NJ, Loi HO, Pinniger GJ, Shannon DG (2012) On the ascent: the soleus operating length is conserved to the ascending limb of the force-length curve across gait mechanics in humans. *J Exp Biol*.
33. Haeufle DF, Grimmer S, Seyfarth A (2010) The role of intrinsic muscle properties for stable hopping--stability is achieved by the force-velocity relation. *Bioinspir Biomim* 5: 16004.
34. Robertson BD, G.S. S (2013) Exploiting Elasticity: Modeling the Influence of Neural Control on Mechanics and Energetics of Ankle Muscle-Tendons During Human Hopping. *Journal of Theoretical Biology In Review*.
35. Carrier DR, Heglund NC, Earls KD (1994) Variable gearing during locomotion in the human musculoskeletal system. *Science* 265: 651-653.
36. Biewener AA, Farley CT, Roberts TJ, Temaner M (2004) Muscle mechanical advantage of human walking and running: implications for energy cost. *J Appl Physiol* 97: 2266-2274.
37. Winters JM, Stark L (1988) Estimated mechanical properties of synergistic muscles involved in movements of a variety of human joints. *J Biomech* 21: 1027-1041.
38. Raasch CC, Zajac FE, Ma B, Levine WS (1997) Muscle coordination of maximum-speed pedaling. *J Biomech* 30: 595-602.
39. Fukunaga T, Roy RR, Shellock FG, Hodgson JA, Day MK, et al. (1992) Physiological cross-sectional area of human leg muscles based on magnetic resonance imaging. *J Orthop Res* 10: 928-934.
40. Lieber RL, Friden J (1999) Mechanisms of muscle injury after eccentric contraction. *J Sci Med Sport* 2: 253-265.

41. Lieber RL, Friden J (1993) Muscle damage is not a function of muscle force but active muscle strain. *J Appl Physiol* 74: 520-526.
42. Morgan DL, Allen DG (1999) Early events in stretch-induced muscle damage. *J Appl Physiol* 87: 2007-2015.
43. Alexander RM (1997) Optimum Muscle Design for Oscillatory Movements. *Journal of Theoretical Biology* 184: 253-259.
44. Ma SP, Zahalak GI (1991) A distribution-moment model of energetics in skeletal muscle. *J Biomech* 24: 21-35.
45. Krishnaswamy P, Brown EN, Herr HM (2011) Human leg model predicts ankle muscle-tendon morphology, state, roles and energetics in walking. *PLoS Comput Biol* 7: e1001107.
46. Bobbert MF, Huijing PA, Schenau GJV (1986) An Estimation of Power Output and Work Done by the Human Triceps Surae Muscle Tendon Complex in Jumping. *Journal of Biomechanics* 19: 899-906.
47. Azizi E, Roberts TJ (2010) Muscle performance during frog jumping: influence of elasticity on muscle operating lengths. *Proc Biol Sci* 277: 1523-1530.
48. Otten E (1987) A myocybernetic model of the jaw system of the rat. *J Neurosci Methods* 21: 287-302.
49. Hill AV (1938) The heat of shortening and the dynamic constants of muscle. *Proceedings of the Royal Society of London Series B-Biological Sciences* 126: 136-195.

CHAPTER 4: A BIO-ROBOTIC FRAMEWORK FOR EVALUATING MUSCLE-LEVEL EFFECTS OF EXOSKELETON ASSISTANCE IN A COMPLIANT MUSCLE-TENDON UNIT

4.1 Abstract

We present an *in-vitro* muscle-tendon unit (MTU) preparation that effectively mimics human neuromechanical response to an assistive passive exoskeleton (Exo) during hopping. Model based predictions were used to estimate combinations of reduced muscle activation and passive Exo stiffness that would result in human like behavior. We also explored the influence of reduced muscle activation in the absence of an assistive Exo, and the addition of an assistive Exo without reductions in muscle activation. Muscle activation/Exo stiffness combinations meant to mimic human behavior did just that, and displayed consistent system level force-length dynamics (i.e. stiffness), along with reduced biological loads, increased muscle excursion, and constant muscle average positive power output. This led to reduced estimated metabolic cost and MTU apparent efficiency, as well as increased apparent efficiency for the MTU+Exo system as a whole. Conditions where activation was reduced without an Exo did not exhibit dramatic shifts in mechanical behavior, as subtle changes in muscle level mechanics favorable to increased force production compensated for reduced activation. Conditions with Exo assistance and without reduced muscle activation exhibited lower muscle strains, lower MTU+Exo apparent efficiency, and equivalent mechanical performance when compared to Exo conditions with reduced activation. Finally, we suggest

that the increased natural resonant frequency of the artificially stiffened MTU+Exo system, along with invariant movement frequencies, may be critical factors limiting beneficial response to springy assistance.

4.2 Introduction

Thanks to rapid advancement of battery, actuator, and human instrumentation technology, the promise of wearable robotic exoskeletons to assist and/or enhance human locomotion is coming to fruition [1]. Recent years have seen the development of powered devices for use within [2-4] and beyond [5-11] a clinical/laboratory setting. While significant time and effort has been invested in development of these exoskeletons, there is ultimately little to show in terms of real user benefit.

One of the major underlying issues in exoskeleton (Exo) design is developing a system that is lightweight, powerful, and does not restrict movement. To circumvent concerns about power and weight, engineers have begun to design passive (i.e. spring loaded) exoskeletons [9-11]. Not only are springy actuators lightweight and potentially powerful, they may also be ideal for facilitating natural movement. Modeling a human leg as a spring-loaded inverted pendulum (SLIP) recovers various modes of bouncing gait (i.e. walking, running, hopping) [12,13], as well as mechanical subtleties critical to stable and efficient walking (i.e. swing leg retraction [14], perturbation response [15]). Because leg mechanics

of bouncing gait are inherently “spring-like,” they are also well suited to integration with springy actuators for locomotion assistance [7,9,11,16].

Another critical issue in Exo design is wearer response, and how integrated control of the underlying biological neuromuscular systems change behavior in the context of applied external assistance. It is well documented that observed “springy” limb mechanics in humans scale down to the joint level as well [17-19]. For the ankle in particular, spring-like joint level mechanics are the result of ‘tuned’ interaction between active contractile elements (CE) (i.e. triceps surae muscles) and compliant series elastic elements (SEE) (i.e. aponeurosis, Achilles tendon) [20-22]. By properly timing muscle activation relative to body inertial dynamics, humans can store and return the majority of energy required for propulsion in series tendon [23]. This drives down mechanical work demands on active tissue, and amplifies its power production capabilities beyond what would be possible for muscle alone [24-26]. This utilization of series elastic tissues for propulsive gait is also dependent high forces that facilitate elastic energy storage and return. By unloading a compliant muscle-tendon unit (MTU) system with an Exo, biological forces will be reduced, and SEE will be less effective as an energy harvester and power amplifier [27].

To better understand how elastic joint and limb mechanics are influenced by springy assistance, researchers have relied on hopping as an experimental model. Hopping is a mechanically simple pattern of movement effectively preserves the salient features of compliant limb behavior observed across all modes of gait [28], while simultaneously relying exclusively on the ankle joint as a source of whole-limb stiffness [29]. Previous work

exploring the influence of a spring-loaded exoskeleton on ankle and limb mechanics during hopping has identified four major features of preference driven adaptation to a springy device. 1) Humans reduce CE activation in response to reduced force demands when hopping in an assistive ankle Exo [27,30,31]. 2) Joint level mechanical adaptation is such that the ankle (and knee) maintain constant stiffness (force versus center of mass height) with an assistive *or* resistive device [16,32]. 3) In response to reduced loads, SEE energy storage and return is reduced, and CE lengthening/shortening over a hopping cycle is increased. The net result is constant CE positive power output [27]. Finally, 4) a springy assistive device can reduce the metabolic demands of hopping *to a point*. Beyond some terminal device stiffness, the metabolic demands of spring assisted hopping are eliminated [33].

A recent modeling study by Robertson et. al. predicted these experimentally observed trends, and provided a physiological basis for understanding the limits of neuromechanical adaptation to a springy assistive device [34]. By sweeping a parameter space of Exo stiffness and muscle activation values (normalized to SEE stiffness and maximal activation respectively), we predicted combinations of reduced CE activation and increased Exo stiffness that maintained overall system (MTU+Exo) stiffness relative to an unassisted baseline condition [34]. Unfortunately, however, muscle models used in these studies are known to be flawed, and fail to capture history dependent dynamics of active muscle force production (i.e. lengthening dependent force enhancement, work dependent deactivation) [35-38]. This shortcoming is further exacerbated by increased muscle excursions during Exo assisted hopping [27], which likely enhance history dependent effects.

To circumvent issues with muscle and tendon models, we developed a hybrid bio-robotic system which implements inertial environment/Exo simulations from previous modeling work on a feedback controlled ergometer, and uses actual biological muscle and tendon in place of a modeled one [34,39]. The in-silico inertial environment in this study consisted of a mass (M) in gravity with a fixed mechanical advantage (l_{in}/l_{out}) and a parallel spring of user-defined stiffness (k_{Exo}), functioning as a modeled elastic Exo (**fig. 1a**). To control relative levels of muscle activation, we used a ‘pulsed’ rate coding approach detailed further in methods below. By experimentally controlling both muscle activation and relative Exo stiffness, we were able to test model findings from [34].

Based on previous modeling and experimental outcomes we predicted that, for realistic combinations of muscle activation/Exo stiffness, we would observe the following trends: **1)** Constant MTU+Exo stiffness [32]. **2)** Constant CE average positive power (\bar{P}_{mech}^+) output due to decreased loading and increased excursion [20], as well as **3)** reductions in modeled metabolic demand [20,33,40] and **4)** MTU efficiency. We further hypothesized that, **5)** despite reductions in MTU efficiency, we would observe increases in overall MTU+Exo apparent efficiency in assisted conditions [34].

4.3 Materials and Methods

4.3.1 Animal Subjects

The five adult American Bullfrogs (*Rana Catesbeiana*) (mean subject mass = 406 ± 42.6 g) used in this study were purchased from a licensed vendor (Rana Ranch, Twin Falls, ID), and housed at the NC State University Biological Resources Facility. Following delivery, and prior to any use in experimental procedures, animals were allowed a one week adaptation period during which they lived in an aquatic environment with ad-libitum access to a terrestrial platform and crickets. Prior to any surgical procedures conducted as part of this work, animals were cold anesthetized and sacrificed using the double-pith technique.

4.3.2 Surgical Preparation

Surgical procedures used as part of this work have been described previously, the details of which can be found in [39]. In brief, following animal sacrifice, a hind limb was removed and placed in a bath of oxygenated ringers solution (100 mM NaCl, 2.5 mM KCl, 2.5 mM NaHCO₃, 1.6 mM CaCl, 10.5 mM Dextrose) at room temperature (~22°C). The plantaris-Achilles tendon MTU was isolated from surrounding muscle with great care taken to preserve the sciatic nerve. The MTU was left intact at its insertion point at the knee, and free muscle/tendon was carefully separated from bone up to the series tendon's distal insertion point at the toes. The plantaris muscle was instrumented with sonomicrometry crystals (1mm diameter, Sonometrics Inc., London, Ontario, CA), and a bipolar stimulating

electrode cuff (Microprobes for Life Science, Gaithersburg, MD, USA) was wrapped around the intact sciatic nerve and connected to an Aurora 701C stimulator (Aurora Scientific, Aurora, Ontario, CA). The MTU preparation was mounted to a rigid plexiglass plate via intact portions of femur and tibia, and the distal portion of free tendon was inserted into a custom friction clamp. The entire preparation was then mounted into a plexiglass chamber of circulating oxygenated ringers solution, and the friction clamp was attached via rigid aircraft cable to a feedback controlled ergometer (Aurora 310B-LR, Aurora Scientific, Aurora, Ontario, CA).

4.3.3 Motor Controllers

Motor controllers used in this study were programmed in Simulink (Mathworks, Natick, MA, USA), and simultaneously controlled muscle stimulation and environment dynamics while recording MTU and CE force/displacement using a dSpace DS1103 control board (dSpace, Paderborn, DE). SEE displacement was assumed to adhere to the following relationship:

$$\Delta L_{SEE} = \Delta L_{MTU} - \Delta L_{CE}$$

Controllers used direct measurements of biological MTU force as an input, and simulated interaction with a virtual environment consisting of a modeled extension spring in parallel with biological MTU interacting with mass in gravity across a fixed mechanical advantage (**fig. 1**). Motor controllers were programmed to adhere to the following relationship:

$$(F_{Exo} + F_{MTU})l_{in} = F_{load}l_{out}$$

Where F_{Exo} is simulated Exo force, F_{MTU} is measured MTU force, F_{load} is force applied to the virtual mass, and l_{in}/l_{out} are moment arm lengths for the MTU+Exo and mass respectively. By rearranging this equation, we can express net force on the virtual mass (F_{net}) as follows:

$$F_{net} = M\ddot{x}_{load} = \left(l_{in}/l_{out} \right) (F_{Exo} + F_{MTU}) - Mg$$

Where M is our virtual inertial load mass, \ddot{x}_{load} is the acceleration of our mass, and g is gravitational acceleration (9.8m/s^2). By solving for \ddot{x}_{load} , and integrating twice, we can compute a time-step displacement for the mass (dx_{load}). Motor arm displacement at each time-step (dx_{MTU}), adheres to the following relationship:

$$l_{in}dx_{MTU} = l_{out}dx_{load}$$

Motor simulation programs were written in Simulink (Mathworks Inc., Natick, MA, USA) used a fixed-step 4th order runge-kutta solver with a sampling rate of 1kHz (**fig. 1A**).

4.3.4 Stimulator Controllers

To investigate the role that both CE activation and Exo stiffness play in MTU adaptation to an external device, we developed a ‘pulsed’ rate coding approach for modulating force output similar to that in Stevens [41]. Using an assumed experimental driving frequency (ω_{Drive}) of 2 Hz (discussed in detail below), and a set stimulation duty of

10% of a driving cycle period (i.e. $T_{stim} = 10\% \omega_{Drive}^{-1} = 50\text{ms}$), we performed a small study (n=3) to determine the influence of ω_{spike} on peak force (F_{peak}) output (**Fig. 1Bi**).

The muscle preparation was the same as those detailed above, except the free tendon was clamped off at the muscle tendon junction to minimize internal shortening against series compliant tissues. The ergometer arm was set to a fixed position for which passive muscle force was $\sim 1\text{N}$, and the muscle was subjected 5 experimental conditions consisting of 3 consecutive contractions ($\omega_{Drive} = 2\text{Hz}$, $T_{stim} = 50\text{ms}$) with ω_{spike} values of 20, 40, 60, 80, and 100 Hz (i.e. # spikes/pulse = 1, 2, 3, 4, and 5 respectively). Based on previous research, we assumed that a ω_{spike} of 100Hz resulted in maximal muscle activation [41-43]. The order of the ω_{spike} conditions was randomized to counteract fatigue effects, and the peak force achieved in each of the 3 contractions was averaged and subsequently normalized to the peak force achieved in the 100Hz condition.

4.3.5 Environment and Exoskeleton Parameter Selection

Controlling system passive resonant frequency (ω_0) was necessary to insure uniform stimulation patterns and subsequent normalized peak muscle activation/force output for all conditions and experimental preparations. System passive resonant frequency was assumed to adhere to the following equation:

$$\omega_0 = \frac{l_{in}}{l_{out}} \sqrt{\frac{k_{MTU}}{M}}$$

Where k_{MTU} is effective passive MTU stiffness, or the total stiffness of passive CE (k_{CE}) and SEE (k_{SEE}) in series, i.e.:

$$k_{MTU} = \left(\frac{1}{k_{CE}} + \frac{1}{k_{SEE}} \right)^{-1}$$

To initially determine ω_0 and k_{MTU} for a given experimental preparation, the MTU was allowed to oscillate passively against a simulated inertial load previously used in [39] ($l_{in} = 1$, $l_{out} = 21$, $M = 0.085kg$).

Once k_{MTU} was determined, l_{out} and M were varied to approximate $\omega_0 = 2\text{Hz}$ for each preparation (**Table 1**). Simulated exoskeleton stiffness' used in subsequent dynamic conditions were set as a percentage of measured k_{MTU} values from the initial passive pluck condition in each prep. In previous modeling work used to guide parameter selection here, k_{Exo} was normalized to SEE stiffness. For the muscle-tendon models used as part of that study, $k_{MTU} = \frac{1}{3}k_{SEE}$ [34,44]. As a result, model predictions used here were scaled accordingly for k_{Exo} normalized to k_{MTU} (e.g. $k_{Exo} = 60\%k_{MTU}$ here is equivalent to $k_{Exo} = 20\%k_{SEE}$ from [34]).

Following all experimental conditions requiring active muscle contractions, a second passive pluck was performed to measure ω_0 under the adjusted inertial parameters used to approximate an $\omega_0 \sim 2\text{Hz}$. This was done last because increased mass and lever arm ratios required to drive ω_0 down to 2.0Hz posed greater injury risk than inertial parameters used in the initial passive pluck (**fig. 1Bii**).

4.3.6 Modeled Exoskeleton

Every experimental condition receiving springy assistance was assigned an Exo ‘slack length’ (l_{slack}), or a length below which there was no tension in the virtual spring. Springs were also modeled so as to not generate compressive loads for lengths $< l_{slack}$. Each trial began with the biological MTU under 1N of passive tension, and this initial absolute motor position (l_{slack}) was stored at the onset of the first stimulus pulse. Force from the virtual Exo was computed as follows:

$$F_{Exo}(l_{Exo}) = \begin{cases} -k_{Exo}(l_{Exo} - l_{slack}), & l_{Exo} > l_{slack} \\ 0, & l_{Exo} \leq l_{slack} \end{cases}$$

Where l_{Exo} is absolute exoskeleton length, and F_{Exo} is exoskeleton force.

4.3.7 Experimental Execution

For each preparation shown here, an initial 300ms fixed end contraction was performed under an initial passive load ($\sim 10\text{N}$, based on previous experience) to determine an approximate value of peak isometric force (F_{max}) for active muscle. After this, an initial passive pluck was performed, k_{MTU} was determined, and system inertial parameters were adjusted to approximate an $\omega_0 \sim 2\text{Hz}$. Next, 3 consecutive fixed end contractions ($\omega_{Drive} = 2.0\text{ Hz}$, $T_{stim} = 50\text{ms}$, $\omega_{spike} = 100\text{Hz}$) were performed to determine a baseline average peak force for a later fatigue assessment.

Following initial identification of system parameters, five combinations of normalized exoskeleton stiffness and muscle activation were explored. Three of these combinations were selected based parameter values from a previous modeling study [34], and were as follows: **1)** 100%*Stim* ($\omega_{spike} = 100\text{Hz}$), 0% k_{MTU} ($k_{Exo} = 0$), **2)** 80%*Stim* ($\omega_{spike} = 60\text{Hz}$), 60% k_{MTU} ($k_{Exo} = 60\%k_{MTU}$), and **3)** 60%*Stim* ($\omega_{spike} = 40\text{Hz}$), 120% k_{MTU} ($k_{Exo} = 120\%k_{MTU}$) (**fig. 1Bi**). Two other combinations of stimulation and exoskeleton stiffness were also used to explore the effects of added stiffness with no change in neural control (100%*Stim*, 60% k_{MTU}), and the effects of reduced muscle activation in the absence of any exoskeleton (80%*Stim*, 0% k_{MTU}). The order of these trials was randomized to counteract fatigue effects.

Each set of dynamic contractions consisted of 10 stimulus pulses. The first five were used to allow the system to reach a steady state, and the last five were used in all subsequent analysis (**fig. 1Ci-ii**). Each experimental condition began with the mass sitting on a virtual ‘table’ which supported its weight. Once MTU force exceeded a set threshold following the initial stimulation pulse of each condition, the ‘table’ was removed, and the mass-exoskeleton-MTU system interacted dynamically. In previous experiments [39], the table force threshold (F_{table}) was computed as follows:

$$F_{table} = \left(l_{out} / l_{in} \right) Mg$$

Where g is gravitational acceleration (9.8m/s^2). Because of increased loads required to drive ω_0 into the 2Hz range, as well as reduced activation in several conditions, this constraint was

relaxed. Table thresholds for all 100% (100 Hz), 80% (60 Hz), and 60% (40 Hz) *Stim* conditions were $80\%F_{table}$, $50\%F_{table}$, and $25\%F_{table}$ respectively.

Following all dynamic experimental conditions, a second set of 3 fixed end contractions was performed with the same stimulus pattern used for the initial set. The average peak force achieved for each of the three stimulus cycles was recorded to quantify relative levels of fatigue. If the percentage of peak force achieved in the final set of fixed end contractions was $<50\%$ of that achieved initially, the experiment was considered a success (mean $\%Fatigue = 66.8 \pm 14.5\%$) Finally, a second passive pluck to measure adjusted ω_0 was performed following all conditions requiring active force generation in muscle.

4.3.8 Experimental Metrics

4.3.8.1 Muscle Properties for Normalization

All values of peak force (F_{peak}) reported here are normalized to a measured F_{max} for each muscle preparation. Once F_{max} was determined for each prep, this value was used in conjunction with absolute CE length data from passive pluck conditions to estimate l_0 . This was done using equations from [45] to perform a least-squared error fit to experimental data. To estimate maximum muscle shortening velocity (v_{max}), the following relationship was assumed [46]:

$$v_{max} = -13.8l_0 \cdot s^{-1}$$

Where s is the unit of time seconds.

4.3.8.2 Length/Velocity Metrics

To determine how muscle mechanical state (i.e. length and velocity, l_{CE} and v_{CE} respectively) influenced force production capability, we report normalized strain and velocity at F_{peak} . We also report peak CE shortening velocity over a cycle of stimulation, as this (along with force) heavily influenced the amount of positive muscle work performed over a cycle of stimulation.

4.3.8.3 Muscle Activation/Deactivation Time Constants

To estimate muscle active state and metabolic demand from a known stimulus pulse, it is necessary to determine muscle activation/deactivation time constants (τ_{act} and τ_{deact} respectively). Values reported here are based on a brute-force least squared error fit of equations describing stimulation/activation coupling from Zajac [47] to stimulation/force data from our initial 300ms maximal contraction. To do this, we swept a range of possible τ_{act} and τ_{deact} values (0-0.2s), modeled resultant activation from our known stimulus pulse, and identified the combination which minimized mean-squared error between observed normalized force and modeled normalized active state.

4.3.8.4 Instantaneous and Average Positive Mechanical Power

Instantaneous mechanical power ($P_{mech}(t)$) for all components was computed as follows:

$$P_{mech}(t) = -F(t) * v(t)$$

Where $F(t)$ and $v(t)$ are instantaneous force and velocity of whatever system component power is being computed for. $F(t)$ was made negative here to insure muscle shortening corresponded to positive power output per convention from previous work [48].

To compute average net mechanical power (\bar{P}_{mech}^{net}), or the average rate of work over a stimulation cycle, we integrated instantaneous power and normalized by cycle period ($T_{Drive} = \omega_{Drive}^{-1}$) as follows:

$$\bar{P}_{mech}^{net} = \frac{1}{T_{Drive}} \int_{t=0}^{T_{Drive}} P_{mech}(t) dt$$

To determine average rates of positive and negative work (\bar{P}_{mech}^{+} and \bar{P}_{mech}^{-} respectively) we use this same approach but only integrate values during shortening (positive) or lengthening (negative), with values of opposite sign set to zero. All mechanical power output data reported here is scaled by subject muscle mass for between-prep comparisons (**table 1**)

4.3.8.5 Estimates of Metabolic Cost and Apparent Efficiency

To estimate instantaneous metabolic cost we used a non-dimensionalized model parameterized in terms of normalized CE velocity ($p_{met}(v_{CE}/v_{max})$) [49]. To provide values of instantaneous metabolic cost in Watts ($P_{met}(t)$), p_{met} is scaled by the physiological constant F_{max} , and muscle active state $\alpha(t)$ as follows [50]:

$$P_{met}(t) = F_{max} * \alpha(t) * p_{met}(t)$$

To determine average metabolic rate (\bar{P}_{met}), we took the same approach to integrating P_{met} that was used for mechanical power. All reported values of \bar{P}_{met} are scaled by subject muscle mass for between-prep comparisons. $\alpha(t)$ was modeled using our stimulus pulse of known duration, previously determined τ_{act} and τ_{deact} time constants, and equations from Zajac [47]. The magnitude of our normalized stimulus pulse was scaled by the relative activation level in each condition. Activation dynamics for 100%, 80%, and 60%*Stim* trials were modeled using stimulus pulses of magnitude 1, 0.8, and 0.6 respectively.

To estimate CE, MTU, and MTU+Exo apparent efficiency (ϵ_{app}) we simply divide \bar{P}_{met} by \bar{P}_{mech} from whichever system component is of interest. Because dynamics observed here were generally cyclic (i.e. $\bar{P}_{mech}^{net} \sim 0$), positive power was used in all efficiency calculations as follows:

$$\epsilon_{app} = \bar{P}_{mech}^+ / \bar{P}_{met}$$

4.3.9 Statistical Analyses

For data that includes all subjects, outcomes over the last five stimulation cycles for each condition and prep were averaged. These averages were then used as individual data points in statistical analysis to determine mean and standard error values reported in this study.

4.3.9.1 Modeled Human Response Data

For combinations of reduced activation and increased stiffness meant to reflect model-predicted trends in human neuromechanical response to Exo assisted hopping from [34], regression fits were used to assess emerging trends in in system dynamic behavior. To fit trends in observed outcomes , we transformed combinations of muscle activation and exoskeleton stiffness to a single descriptive independent variable called the “compensation index” (*CI*) computed as follows:

$$CI = \frac{(100 - \%Stim)}{100} + \frac{\%k_{MTU}}{100}$$

CI values for the (100%*Stim*, 0%*k_{MTU}*), (80%*Stim*, 60%*k_{MTU}*), and (60% *Stim*, 120%*k_{MTU}*) conditions were 0, 0.8, and 1.6 respectively. Observed trends were assumed to be significant for $p < 0.05$. Regression fit equations, p values, and R^2 values for all reported data can be found in **table 2**.

4.3.9.2 Non-Human Response Data

To assess the results of reducing %*Stim* only (i.e. (80%*Stim*, 0%*k_{MTU}*)) and adding an Exo only (i.e. (100%*Stim*, 60%*k_{MTU}*)), paired t-tests were performed between these conditions and the baseline $CI = 0$ condition (i.e. 100%*Stim*, 0%*k_{MTU}*). p values for these comparisons between these conditions are reported in **table 3**.

4.4 Results

4.4.1 Pulsed Rate Coding and Activation/Force Modulation

Based on outcomes from this small study of fixed end contractions in the absence of series tendon, we determined that activation levels of 100%, 80%, and 60% could be reliably achieved for ω_{spike} values of 100Hz, 60Hz, and 40Hz respectively ($p < 0.0001$, $R^2 = 0.86$) (**fig. 1Bi**).

4.4.2 Physiological Constants

Mean and standard deviation values for all measured/estimated physiological constants are shown in **table 1**. This table also includes initial measured ω_0 (2.40 ± 0.11 Hz) and k_{MTU} (8559 ± 919 N/m) using set inertial parameters ($l_{in} = 1$, $l_{out} = 21$, $M = 0.085$ kg), as well adjustments made to these parameters ($l_{out} = 23.6 \pm 0.89$, $M = 0.095 \pm 0.004$ kg), and a final measured ω_0 (2.25 ± 0.05 Hz), and k_{MTU} ($11,241 \pm 681$ N) values (**fig. 1Bii**). There was no preparation for which the target ω_0 of 2Hz was achieved, and in all cases k_{MTU} increased substantially under modified load conditions. This was primarily due to non-linear contributions of passive CE stiffness to overall k_{MTU} . While the system was typically driven slightly below its natural ω_0 in dynamic conditions, we observed phasing dynamics and high levels of SEE energy cycling characteristic of a ‘tuned’ MTU interaction [39].

4.4.3 Work loop Dynamics

For experimental parameters designed to mimic human neuromechanical response to an external device, as well as all others, MTU and/or MTU+Exo stiffness was generally constant, and net work was ~ 0 in all conditions (**fig. 2Ai**). This was facilitated by reduced MTU/CE/SEE force (**fig. 2Aii-iv**), as well as increased CE displacement (**fig. 2Aiii**), resulting from significant Exo contributions to overall force (**fig. 2Av**) in assisted conditions (i.e. $k_{Exo} \neq 0$).

4.4.4 System Dynamics vs. Time

All experimental conditions shown here resulted in symmetric and alternating phases of lengthening/negative power and shortening/positive power (**fig. 2B-F**). Within-subject standard deviations in in force, length, and power vs. time were generally low, with the exception of the (60% *Stim*, 120% k_{MTU}) condition (**fig. 2D**). While this condition did show greater variability relative to all others, it was not enough to warrant exclusion for being non-periodic based on time-series data (**fig. 2D**).

4.4.5 Peak Forces and Phasing

For conditions meant to reflect human neuromechanical response to Exo assistance, MTU force decreased significantly ($p = 0.0015$, $R^2 = 0.55$), while Exo and MTU+Exo increased significantly ($p < 0.0001$, $R^2 = 0.86$ and $p = 0.035$, $R^2 = 0.43$ respectively) with increasing k_{Exo} and decreasing %*Stim* (**fig. 3A**, **table 2**). Peak MTU forces observed in the

(80%*Stim*, 0%*k_{MTU}*) and (100%*Stim*, 60%*k_{MTU}*) conditions were not significantly different than those observed for the baseline (100%*Stim*, 0%*k_{MTU}*) condition. However, peak MTU+Exo forces observed for the (100%*Stim*, 60%*k_{MTU}*) condition were significantly increased relative to the unassisted baseline ($p = 0.015$) (**fig. 3A**, **table 3**).

All phasings reported here are relative to minimum MTU length from the previous cycle. The phasing of peak force was consistent across all conditions, and occurred at almost exactly 50% of a cycle (**fig. 3B**). The phasing of stimulation onset, however, varied significantly ($p = 0.034$, $R^2 = 0.43$) for conditions meant to be reflective of human behavior; and increased from ~30% in the (100%*Stim*, 0%*k_{MTU}*) condition, to ~50% in the (60%*Stim*, 120%*k_{MTU}*) condition (**fig. 3B**, **table 2**). No significant variation was observed in in force or stim phasing dynamics for the (100%*Stim*, 60%*k_{MTU}*) or (80%*Stim*, 0%*k_{MTU}*) conditions (**fig. 3B**).

4.4.6 Muscle Mechanical State

No significant trends were observed in either CE strain (**fig. 3C**) or CE velocity (**fig. 3D**) at the time of peak force for human response or the (80%*Stim*, 0%*k_{MTU}*) conditions (**tables 2, 3**). There was, however, a significant reduction in CE strain at peak force observed between the (100%*Stim*, 60%*k_{MTU}*) and (100%*Stim*, 0%*k_{MTU}*) conditions (**fig. 3C**, **table 3**).

Despite non-significant changes in CE strain or velocity at F_{peak} for human response conditions, there were significant increases in peak shortening velocity ($p = 0.04$, $R^2 = 0.42$) (**fig. 3E**, **table 2**). A significant increase in peak shortening velocity relative to (100%*Stim*, 0% k_{MTU}) was also observed for the (100%*Stim*, 60% k_{MTU}) condition ($p = 0.046$) (**fig. 3E**, **table 3**).

4.4.7 Power Output Dynamics

For all conditions examined here, MTU+Exo $\bar{P}_{mech}^{net} \sim 0$, indicating mechanical behavior that was cyclic on average (**fig. 4A**). For conditions meant to approximate human behavior during non- and exo-assisted hopping, significant increases in MTU+Exo \bar{P}_{mech}^+ ($p = 0.046$, $R^2 = 0.27$) (**fig. 4A**) occurred concomitantly with statistically significant decreases in MTU \bar{P}_{mech}^+ ($p = 0.013$, $R^2 = 0.39$) and \bar{P}_{mech}^- ($p = 0.0017$, $R^2 = 0.55$) (**fig. 4B**) (**table 2**). We also observed statistically significant decreases in CE \bar{P}_{mech}^- ($p = 0.025$, $R^2 = 0.33$) (**fig. 4C**), and SEE \bar{P}_{mech}^+ ($p = 0.031$, $R^2 = 0.31$) (**fig. 4D**), as well as near constant CE \bar{P}_{mech}^+ in these conditions (**fig. 4D**) (**table 2**). Finally, all of this coincided with statistically significant increases in Exo \bar{P}_{mech}^+ ($p = 0.0008$, $R^2 = 0.70$) and \bar{P}_{mech}^- ($p = 0.0003$, $R^2 = 0.74$) (**fig. 4E**, **table 2**). When power production was broken down into percent contribution of each system component to overall \bar{P}_{mech}^+ , we saw statistically significant decreases in both %CE ($p = 0.001$, $R^2 = 0.68$) and %SEE ($p < 0.0001$, $R^2 = 0.81$) \bar{P}_{mech}^+ occurring concomitantly with significant increases %Exo \bar{P}_{mech}^+ ($p < 0.0001$, $R^2 = 0.91$) (**fig. 4F**, **table 2**).

For experimental conditions not meant to mimic human Exo response, statistically significant increases in MTU+Exo \bar{P}_{mech}^+ ($p = 0.0075$) and \bar{P}_{mech}^- ($p = 0.0011$) (**fig. 4A-E**), as well as significant decreases in percent contribution to overall \bar{P}_{mech}^+ from CE ($p = 0.044$) and SEE ($p = 0.0002$) (**fig. 4F**) were observed between (100%*Stim*, 0% k_{Exo}) and (100%*Stim*, 60% k_{Exo}) conditions (**table 3**). No significant differences were observed in terms of power output between the (100%*Stim*, 0% k_{Exo}) and (60%*Stim*, 0% k_{Exo}) conditions.

4.4.8 Estimated Metabolic Cost and Apparent Efficiency

For conditions trading-off biological muscle activation and elastic exoskeleton stiffness (reduced %*Stim* and increased k_{Exo}), we generally observed decreased metabolic demand (**fig 5A**) and MTU ϵ_{app} (**fig. 5C**), increased MTU+Exo ϵ_{app} (**fig. 5B**), and a relatively constant CE ϵ_{app} (**fig. 5D**) with. The only one of these trends that was significant, however, was MTU+Exo ϵ_{app} ($p = 0.024$, $R^2 = 0.46$) (**table 2**).

For the (80%*Stim*, 0% k_{MTU}) condition, metabolic demand was generally reduced (**fig. 5A**), while neither MTU nor CE ϵ_{app} showed any difference from (100%*Stim*, 0% k_{Exo}) condition (**fig.5C-D**). In the (100%*Stim*, 60% k_{MTU}) condition, however, there were observed increases in metabolic demand and MTU+Exo ϵ_{app} (**fig.5A-B**), reductions in MTU ϵ_{app} (**fig. 5C**), and no change in CE ϵ_{app} (**fig. 5D**). The only

statistically significant outcome, however, was increased MTU+Exo ε_{app} between the (100%*Stim*, 0%*k_{Exo}*) and (100%*Stim*, 60%*k_{Exo}*) conditions ($p = 0.032$) (**fig. 5B, table 3**).

4.5 Discussion and Conclusions

Using a previous predictive model of Exo assisted hopping in humans as a guide [34], we hypothesized that **1)** MTU+Exo stiffness would remain constant for conditions meant to mimic human response to a springy device [32]. This prediction was confirmed by experimental outcomes (**fig. 2Ai**), where near constant stiffness was observed in *all* conditions, not just those meant to mimic human behavior. In experimental conditions with Exo assistance, constant MTU+Exo stiffness was the result of reduced biological forces (**fig. 2Aii, 4B**), as well as increased CE and SEE excursions (**fig. 2Aiii-iv**). While increased SEE excursion and reduced forces are not typically something that go hand in hand, it should be noted that the tendon appears to be operating in its non-linear “toe” region during assisted conditions, and in a linear region of stiffness in unassisted conditions (**fig. 2Aiv**).

Our second prediction that **2)** increased CE excursions combined with decreased forces in Exo assisted conditions would result in constant CE power output was partially confirmed. We did see generally constant \bar{P}_{mech}^+ output, but observed trends in decreased \bar{P}_{mech}^- output were found to be significant (**fig. 4C, table 2**). Constant CE \bar{P}_{mech}^+ coincided with decreased biological force output (**fig. 3A**) and increased peak shortening

velocities/excursions (**fig. 3E, 2Aiii, 2Bii-Dii**), as predicted. While it is likely that environmental force demands were lower on the MTU with exo assistance, it is also plausible that this was compounded by increased muscle shortening velocities that reduced force production capability within the muscle and caused work dependent deactivation [51]. Either way, the end result was near constant CE \bar{P}_{mech}^+ in all Exo assisted conditions (**fig. 4C**). Reductions in CE \bar{P}_{mech}^- were made possible by reduced loads, which eliminated the need for active CE lengthening to meet environmental force demands, and drove down the amount of negative CE work performed (**fig. 4C**).

Our final hypotheses stated that there would be **3**) reductions in \bar{P}_{met} and **4**) MTU ε_{app} , but that **5**) MTU+Exo ε_{app} would ultimately increase. While observed trends in both \bar{P}_{met} and MTU ε_{app} verify these hypotheses, regression fits to data were not significant (**fig. 5A,C table 2**). There was, however a significant trend for increased MTU+Exo ε_{app} with decreasing %*Stim* and increasing k_{Exo} , verifying our final prediction (**fig. 5B, table 2**).

4.5.1 Potential Benefits of ‘De-tuned’ MTU Mechanics

There is obvious mechanical and energetic benefit to ‘tuned’ muscle tendon interaction in terrestrial locomotion [24]. There is also emerging evidence to show that, when using a elastic exoskeleton device, ‘tuned’ CE-SEE interactions are disrupted by reduced force demands on biological tissue [27,34]. Even though elastic (and likely any) assistive ankle exoskeleton will augment CE-SEE interactions, metabolic [27,33,40] and mechanical [27,30-33] benefit can still be derived from these sorts of devices under the right conditions.

In the present study, combinations of $\%Stim$ and k_{Exo} designed to mimic human physiological response to exoskeleton-assisted hopping did just that, resulting reduced modeled \bar{P}_{met} (**fig. 5A**) and increased MTU+Exo ε_{app} (**fig. 5B**). Another interesting outcome observed here and during Exo assisted hopping in humans [27], but not predicted by previous modeling studies [34], was reduced absolute CE/fascicle length (**fig. 3C**) and tendon strain (**fig. 1A, 4D**). This generally reduces risk of injury, which is a common goal in exoskeleton design in general, and for load carriage in particular [7].

4.5.2 Frequency-Phase Coupling as a Factor Limiting Human Performance with Elastic Exoskeletons

Previous experimental work from Grabowski et. al. nicely demonstrates that, while some Exo assistance can be beneficial in hopping, too much added stiffness can eliminate device metabolic benefit [33]. This same outcome was predicted in a previous modeling study, which indicated that Exo stiffness can be increased in conjunction with reduced muscle activation up to some terminal stiffness. Once this terminal stiffness is exceeded, model predictions indicate that increased muscle activation/metabolic energy is required to meet task demands of hopping (i.e. alternating phases of ground contact and flight) [34]. While this effect is observable and predictable, the factors governing its emergence are still unclear based on the results of previous studies.

Results presented here, as well as previous work exploring the coupling of driving frequency and phase as a function of passive MTU stiffness may be able to provide some

insight into this phenomena [39]. In general, driving a compliant system well below its passive resonant frequency (ω_0) will result in coincident phasing of peak force and muscle activation, and eliminate many of the benefits of a compliant series tendon [39]. By adding exoskeleton stiffness via environment simulation in this study, we have effectively increased system stiffness and ω_0 without varying ω_{Drive} . This resulted in a shift in stimulation phasing from $\sim 30\%$ in the (100%*Stim*, 0% k_{MTU}) condition to $\sim 50\%$ in (60%*Stim*, 120% k_{MTU}) condition (**fig. 3B**), as would be expected for a biological MTU driven well below ω_0 [39]. While there are certainly other factors governing the limits of neuromechanical response to an assistive device, our results highlight that the relationship between k_{MTU} , k_{Exo} , and their influence on ω_0 relative to preferred movement frequencies must not be ignored.

4.5.3 Effects of Reduced Muscle Activation *Only*

There was a clear reduction in force production capability between an ω_{spike} of 60 and 100Hz for fixed end contractions (**fig. 1Bi**), but it was not apparent under dynamic loading in the (80%*Stim*, 0% k_{MTU}) and (100%*Stim*, 0% k_{MTU}) conditions (**fig. 3A**). This is likely due to subtle changes in muscle level mechanics that can ultimately compensate for reduced active force production. The (60%*Stim*, 0% k_{Exo}) generally had a slightly higher strain at peak force (**fig. 3C**), and lower peak shortening velocity following stimulation onset (**fig. 3E**). This would result in slightly higher passive CE forces, a more favorable force-velocity operating point, and reduced work dependent muscle deactivation [51], all of which would increase CE force output. This suggests a robust mechanism for maintaining CE force

output for variable patterns of activation in a compliant MTU system. However, because these subtle changes in CE strain and velocity dynamics were not statistically significant (**table 3**), it is not possible to make any definitive statements here regarding their effects on observed behavior.

4.5.4 Effects of Increased Stiffness *Only*

Increasing k_{Exo} without reducing %*Stim* in the (100%*Stim*, 60% k_{MTU}) condition significantly enhanced MTU+Exo performance (i.e. F_{peak} , \bar{P}_{mech}^+ , ε_{app}) relative to the (100%*Stim*, 0% k_{MTU}) condition (**fig. 3A, 4A, 5B, table 3**). That being said, increases in MTU+Exo F_{peak} and \bar{P}_{mech}^+ were no greater than those observed for the (80%*Stim*, 60% k_{MTU}) and (60%*Stim*, 120% k_{MTU}) conditions (**fig. 3A, 4A**), and MTU+Exo ε_{app} was considerably lower (**fig. 5B**). This was due primarily to a considerable (but not statistically significant) increase in modeled \bar{P}_{met} relative to all conditions (**fig. 5A, table 3**). In general, all positive outcomes from the (100%*Stim*, 60% k_{Exo}) condition were observed in reduced %*Stim* and increased k_{Exo} conditions but consumed less metabolic energy (**fig. 5A**), and performed with greater MTU+Exo ε_{app} (**fig. 5B**). The only positive outcome from the (100%*Stim*, 60% k_{Exo}) condition that was not replicated elsewhere was a large reduction in CE strain at F_{peak} , which would ultimately drive down risk of injury to a greater extent than the (80%*Stim*, 60% k_{MTU}) and (60%*Stim*, 120% k_{MTU}) conditions (**fig. 3C**).

Based on data presented here, it can be argued that there are advantages to either reducing levels of muscle activation in response to Exo assistance (e.g. reduced \bar{P}_{met} , increased MTU+Exo ε_{app}) (**fig. 5A,B**), or maintaining unassisted levels of muscle activation (e.g. reduced CE strain/injury risk) (**fig. 3C**). Previous data from human studies of preference driven response to Exo assisted hopping, however, demonstrates that people generally choose reduce muscle activation [30,31]. In other words, it seems likely that metabolic demand and system (MTU+Exo) efficiency trump injury avoidance as a driving factor underlying human response to an assistive device.

4.6 Future Directions

The test-bed we have developed and demonstrated here is a powerful tool to explore the impact of local inertial environment (e.g. gravitational load with springy assistance) on the mechanics and energetics of biological MTU function. In future work, we hope to further modify controllers to explore alternative environment perturbations. For example, we plan to virtually design active exoskeletons that uses measurements of CE mechanical state (i.e. length and velocity) and MTU force as real-time parameters governing levels of assistance. We can also hope to alter inertial environments (e.g. reduce gravity, make loads fluid instead of gravitational) to understand the utility of biological MTU outside the context of earth-bound terrestrial locomotion. Finally, we hope to combine these two approaches for rapid

prototyping and testing of exoskeleton controllers that optimize MTU function in novel environments.

4.7 Tables

Table 1, Measured and Estimated Parameters: Mean \pm 1STD values of measured and predicted physiological constants from all experimental subjects

<i>Physiological Parameter</i>	<i>Mean \pm 1STD</i>
<i>Initial ω_0</i>	2.40 \pm 0.11 Hz
<i>Initial k_{MTU}</i>	8559 \pm 919 N/m
<i>Adjusted l_{out}</i>	23.6 \pm 0.89
<i>Adjusted M</i>	0.095 \pm 0.004 kg
<i>Adjusted ω_0</i>	2.25 \pm 0.05 Hz
<i>Final k_{MTU}</i>	11241 \pm 681 N/m
<i>F_{max}</i>	42.00 \pm 9.63 N
<i>τ_{act}</i>	0.074 \pm 0.006 s
<i>τ_{deact}</i>	0.100 \pm 0.02 s
<i>l_0</i>	14.57 \pm 1.23 mm
<i>v_{max}</i>	-201 \pm 17.03 mm/s
<i>Muscle mass</i>	5.52 \pm 1.17 g
<i>Animal mass</i>	406.6 \pm 42.6 g
<i>Fatigue %</i>	66.8 \pm 14.5%

Table 2, Regression Fits: Table of regression fit order, equation, R^2 , and p values for all reported metrics. A p value with red text indicates a non-significant regression trend

<u>Metric</u>	<u>Fit Order</u>	<u>Fit Equation</u>	<u>R^2</u>	<u>p-value</u>	<u>Figure</u>
MTU + Exo F_{peak}	2nd	$1.17 + 0.83CI - 0.32CI^2$	0.43	0.035	3A
MTU F_{peak}	1st	$1.18 - 0.35CI$	0.55	0.0015	3A
Exo F_{peak}	2nd	$1.15CI - 0.30CI^2$	0.43	<0.0001	3A
% Phase F_{peak}	1st	$49.45 + 0.095CI$	0.002	0.88	3B
%Phase Stim Onset	2nd	$30.47 - 11.80CI + 13.77CI^2$	0.43	0.034	3B
CE Strain @ F_{peak}	2nd	$1.33 - 0.33CI + 0.15CI^2$	0.20	0.085	3C
CE v @ F_{peak}	2nd	$-0.0028 - 0.012CI - 0.012CI^2$	0.06	0.48	3D
CE peak shortening v	2nd	$0.059 + 0.11CI - 0.034CI^2$	0.42	0.04	3E
MTU+Exo \bar{P}_{mech}^+	1st	$40.54 + 15.43CI$	0.27	0.046	4A
MTU+Exo \bar{P}_{mech}^-	1st	$43.51 - 10.93CI$	0.22	0.079	4A
MTU+Exo \bar{P}_{mech}^{net}	1st	$-2.96 + 4.50CI$	0.27	0.049	4A
MTU \bar{P}_{mech}^+	1st	$36.31 - 9.30CI$	0.39	0.013	4B
MTU \bar{P}_{mech}^-	1st	$-38.94 + 12.20CI$	0.55	0.0017	4B
MTU \bar{P}_{mech}^{net}	1st	$-2.62 + 2.90CI$	0.25	0.06	4B
CE \bar{P}_{mech}^+	1st	$12.47 - 1.17CI$	0.04	0.46	4C
CE \bar{P}_{mech}^-	1st	$-7.11 + 2.96CI$	0.33	0.025	4C
CE \bar{P}_{mech}^{net}	2nd	$4.20 + 10.49CI - 5.44CI^2$	0.21	0.35	4C
SEE \bar{P}_{mech}^+	1st	$29.51 - 7.21CI$	0.31	0.031	4D
SEE \bar{P}_{mech}^-	1st	$-37.5CI + 8.33CI$	0.23	0.076	4D
SEE \bar{P}_{mech}^{net}	2nd	$-6.57 - 9.52CI + 6.65CI^2$	0.3	0.5	4D
Exo \bar{P}_{mech}^+	2nd	$56.63CI - 19.92CI^2$	0.7	0.0008	4E
Exo \bar{P}_{mech}^-	2nd	$-5.57CI + 21.52CI^2$	0.74	0.0003	4E
Exo \bar{P}_{mech}^{net}	1st	$-0.34 + 1.63CI$	0.28	0.042	4E
%P_{mech}^+ CE	2nd	$0.29 - 0.21CI + 0.075CI^2$	0.68	0.001	4F
%P_{mech}^+ SEE	2nd	$0.71 - 0.56CI + 0.17CI^2$	0.81	<0.0001	4F
%P_{mech}^+ Exo	2nd	$0.77CI - 0.25CI^2$	0.91	<0.0001	4F
\bar{P}_{met}	2nd	$82.21 + 3.13CI - 8.17CI^2$	0.25	0.17	5A

Table 2 Continued

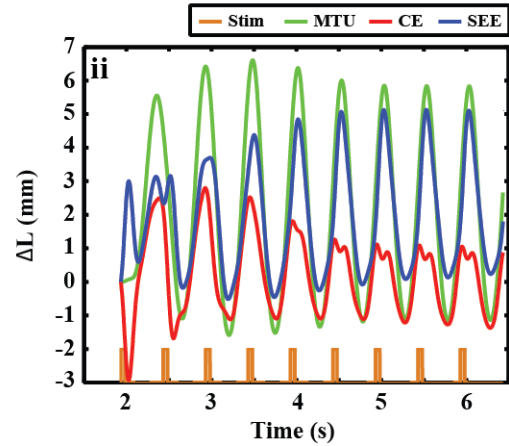
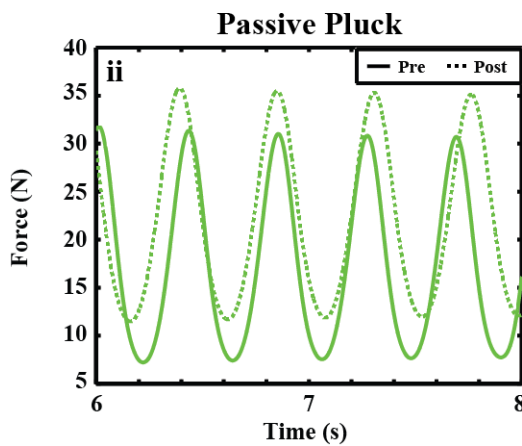
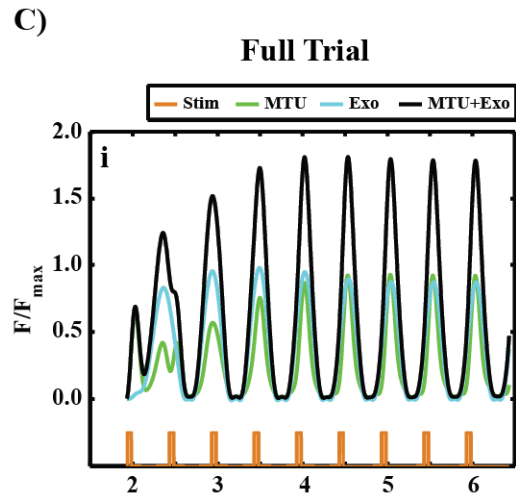
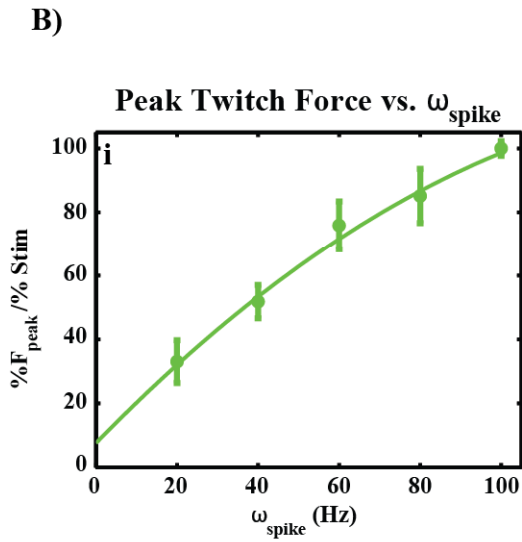
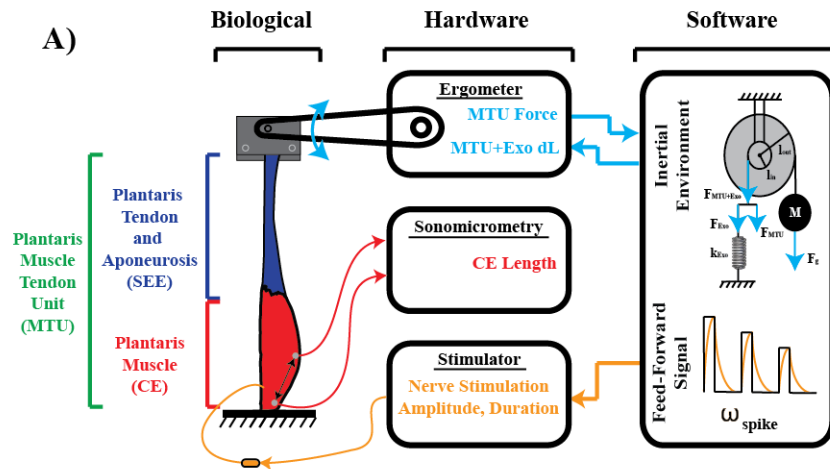
<i>MTU+Exo</i> ε_{app}	2nd	$0.46 + 0.51CI - 0.14CI^2$	0.46	0.024	5B
<i>MTU</i> ε_{app}	2nd	$0.46 - 0.17CI + 0.056CI^2$	0.20	0.27	5C
<i>CE</i> ε_{app}	2nd	$0.15 + 0.021CI - 0.011CI^2$	0.01	0.96	5D

Table 3, Paired t-tests: Table of p values from students t-test for significant difference in experimental metrics relative to the (100%*Stim*, 0% k_{MTU}) condition. A red value indicates a non-significant difference.

Metric	(80% <i>Stim</i> , 0% k_{Exo}) <i>p-value</i>	(100% <i>Stim</i> , 60% k_{Exo}) <i>p-value</i>	Figure
<i>MTU + Exo F_{peak}</i>	-	0.15	3A
<i>MTU F_{peak}</i>	0.21	0.0014	3A
<i>Exo F_{peak}</i>	-	0.029	3A
% <i>Phase F_{peak}</i>	0.036	0.63	3B
% <i>Phase Stim Onset</i>	0.29	0.75	3B
<i>CE Strain @ F_{peak}</i>	0.75	0.07	3C
<i>CE v @ F_{peak}</i>	0.29	0.59	3D
<i>CE peak shortening v</i>	0.29	0.046	3E
<i>MTU+Exo P_{mech}⁺</i>	-	0.0075	4A
<i>MTU+Exo P_{mech}⁻</i>	-	0.013	4A
<i>MTU+Exo P_{mech}^{net}</i>	-	0.86	4A
<i>MTU P_{mech}⁺</i>	0.16	0.31	4B
<i>MTU P_{mech}⁻</i>	0.15	0.28	4B
<i>MTU P_{mech}^{net}</i>	0.90	0.76	4B
<i>CE P_{mech}⁺</i>	0.86	0.48	4C
<i>CE P_{mech}⁻</i>	0.73	0.15	4C
<i>CE P_{mech}^{net}</i>	0.47	0.13	4C
<i>SEE P_{mech}⁺</i>	0.048	0.95	4D
<i>SEE P_{mech}⁻</i>	0.084	0.52	4D
<i>SEE P_{mech}^{net}</i>	0.41	0.16	4D
<i>Exo P_{mech}⁺</i>	-	0.007	4E
<i>Exo P_{mech}⁻</i>	-	0.0011	4E
<i>Exo P_{mech}^{net}</i>	-	0.82	4E
% <i>P_{mech}⁺ CE</i>	0.35	0.044	4F
% <i>P_{mech}⁺ SEE</i>	0.35	0.0002	4F
% <i>P_{mech}⁺ Exo</i>	-	0.0017	4F
<i>P_{met}</i>	0.19	0.22	5A
<i>MTU+Exo ε_{app}</i>	-	0.95	5B
<i>MTU ε_{app}</i>	0.83	0.06	5C
<i>CE ε_{app}</i>	0.48	0.032	5D

4.8 Figures

Figure 1, Experimental Schematic and Sample Data: **A)** Schematic of experimental preparation including, biological, hardware, and software components. **Bi)** Influence of ω_{spike} on muscle force/activation levels. **Bii)** Force vs. time in initial and final passive pluck conditions for a single prep. Note higher forces and lower oscillation frequency for the post condition. Representative **Ci)** Force and **Cii)** length change dynamics from a single ($80\%Stim, 60\%k_{MTU}$) trial. Note that steady state behavior is generally achieved within the first 5 stimulation cycles.



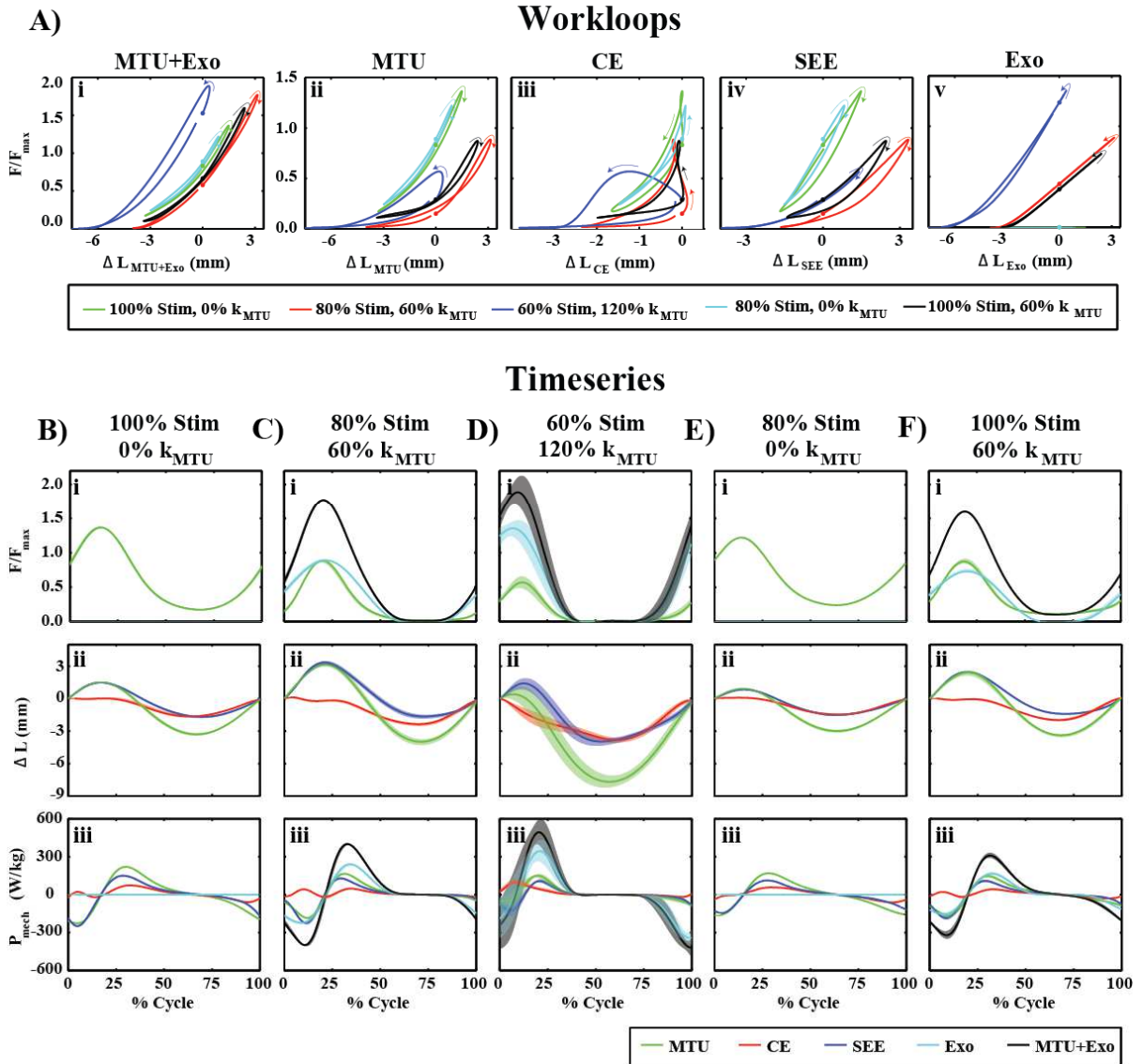


Figure 2, Cycle Dynamics: All data shown here were taken from a single representative prep. Workloop data for **Ai)** MTU+Exo, **Aii)** MTU, **Aiii)** CE, **Aiv)** SEE, and **Av)** Exo in all experimental conditions. **B-F)** Time series data of **i)** force, **ii)** length change, and **iii)** power output for all system components and all experimental conditions. Note that, in exo assisted conditions, reduced biological (i.e. MTU) forces (**i)**) occur concomitantly with increased CE excursions (**ii)**).

Figure 3, Peak Force, Phasing, and CE Operating Point: Plots of mean \pm 1SE **A)** peak force **B)** stimulation and peak force phasing, **C)** CE strain at peak force, **D)** CE velocity at peak force, and **E)** peak CE shortening velocity across all experimental subjects and conditions. Data points to the left of dashed line are for parameter combinations meant to mimic human response to Exo assisted hopping. Regression trends in each figure are fit to the compensation indexes for these conditions. Statistically significant regression fits are indicated with a bracket and star. Data points to the right of the dashed line are for reduced activation and increased k_{Exo} only conditions. Statistically significant difference from the (100%*Stim*, 0% k_{MTU}) condition is indicated by a star. Note that increased k_{Exo} generally resulted in reduced biological forces and CE strains at peak force, as well as increased stimulation phasing and peak shortening velocity.

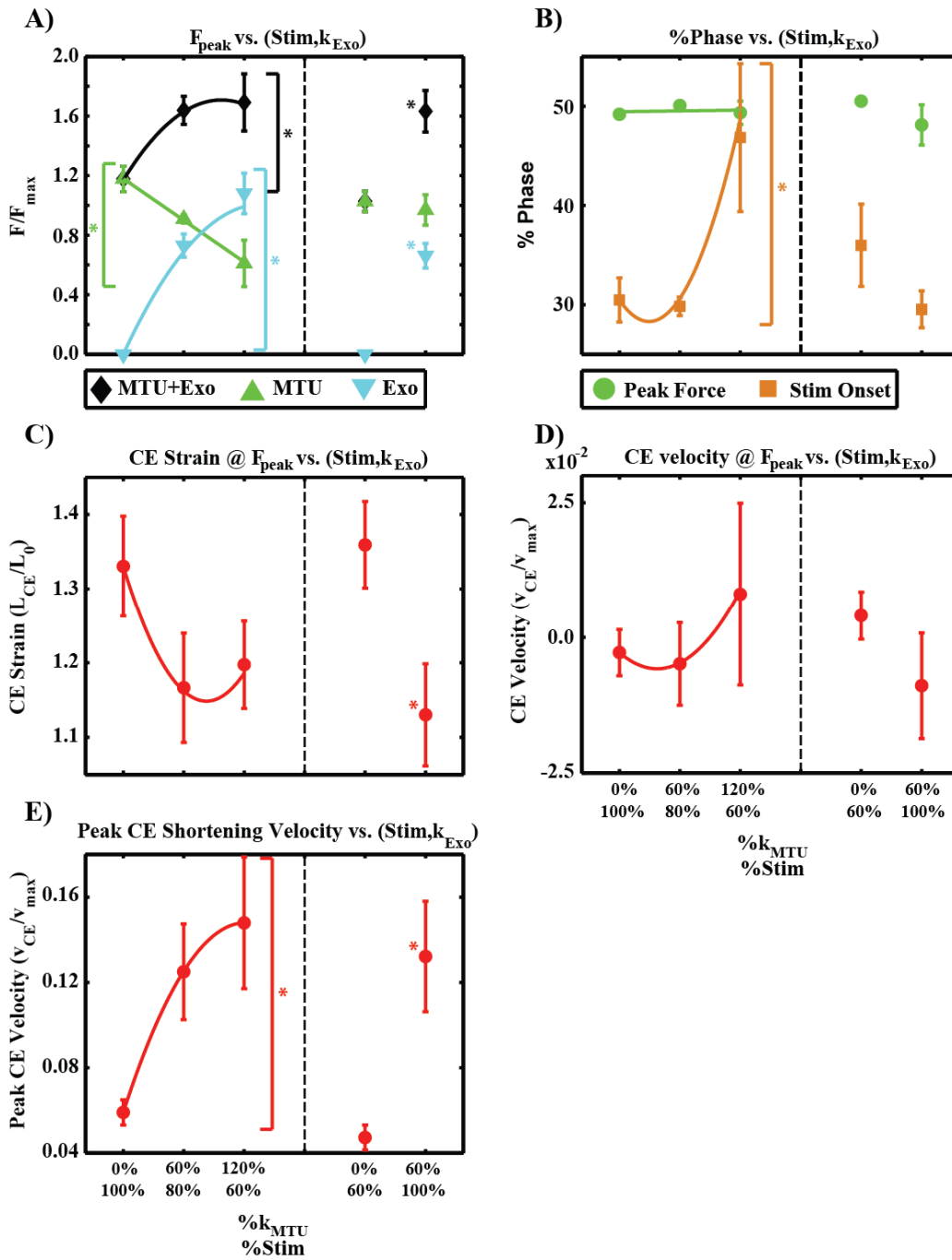
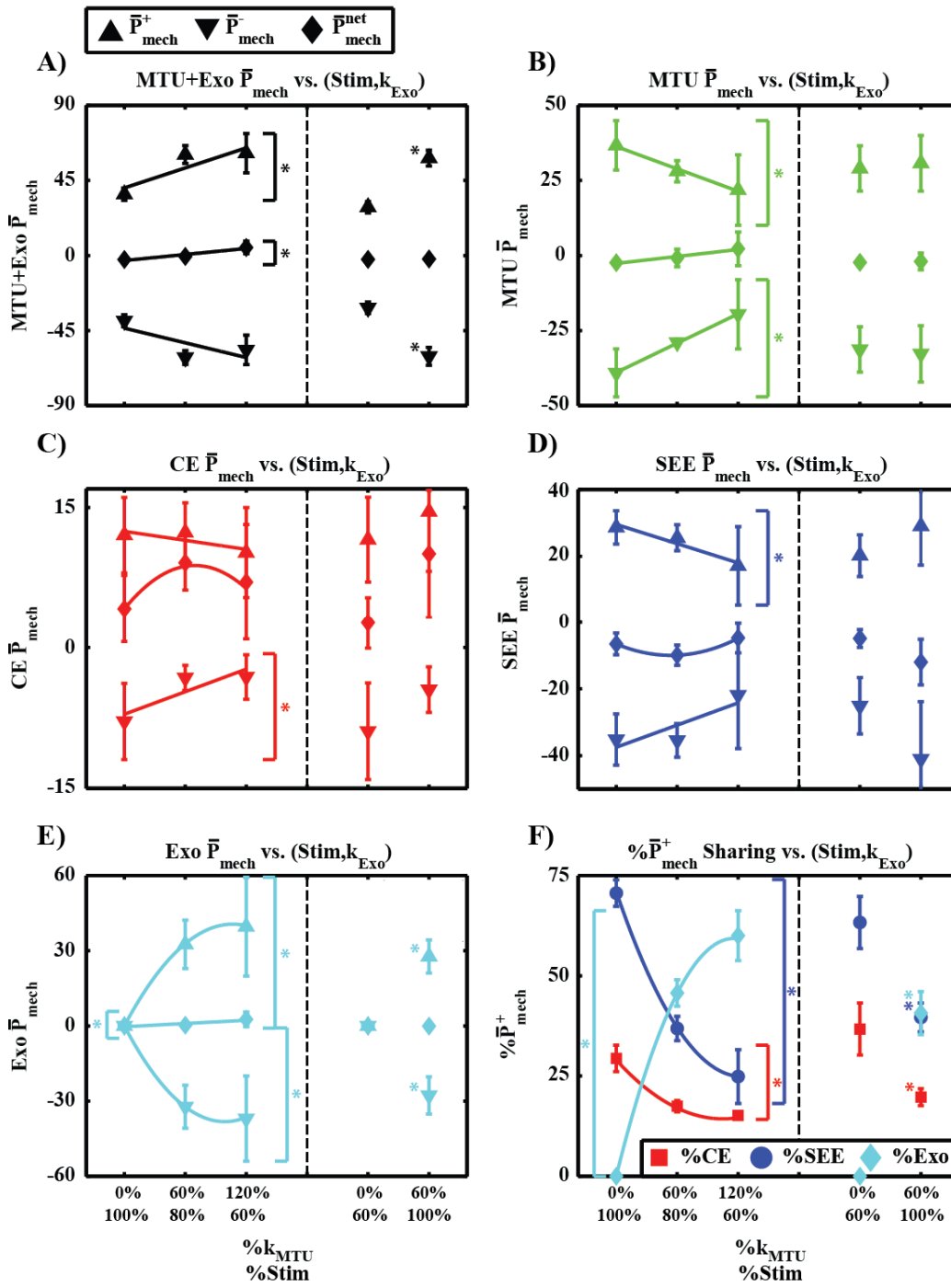


Figure 4, Average Power Output and Sharing: Plots of mean \pm 1SE \bar{P}_{mech}^+ , \bar{P}_{mech}^- , and \bar{P}_{mech}^{net} for **A)** MTU+Exo, **B)** MTU, **C)** CE, **D)** SEE, and **E)** Exo for all subjects and experimental conditions. **F)** Plot of mean \pm 1SE % contribution from CE, SEE, and Exo to overall positive power for all subjects and experimental conditions. In all figures, data to the left of the dashed line mimics human response to Exo assistance, and trend lines are fit to compensation indexes for these conditions. Significant trends are indicated by a bracket around data and a star. Data to the right of the dashed line is for reduced activation and increased k_{Exo} only conditions. Significant differences from the (100%*Stim*, 0% k_{MTU}) data point are indicated by stars for these conditions. Note that net MTU+Exo \bar{P}_{mech}^{net} was ~ 0 for all conditions, indicating generally cyclic behavior. Also note that, in conditions with an Exo, MTU+Exo \bar{P}_{mech}^+ is increased, MTU and SEE \bar{P}_{mech}^+ is decreased, and CE \bar{P}_{mech}^+ is relatively constant compared to the baseline



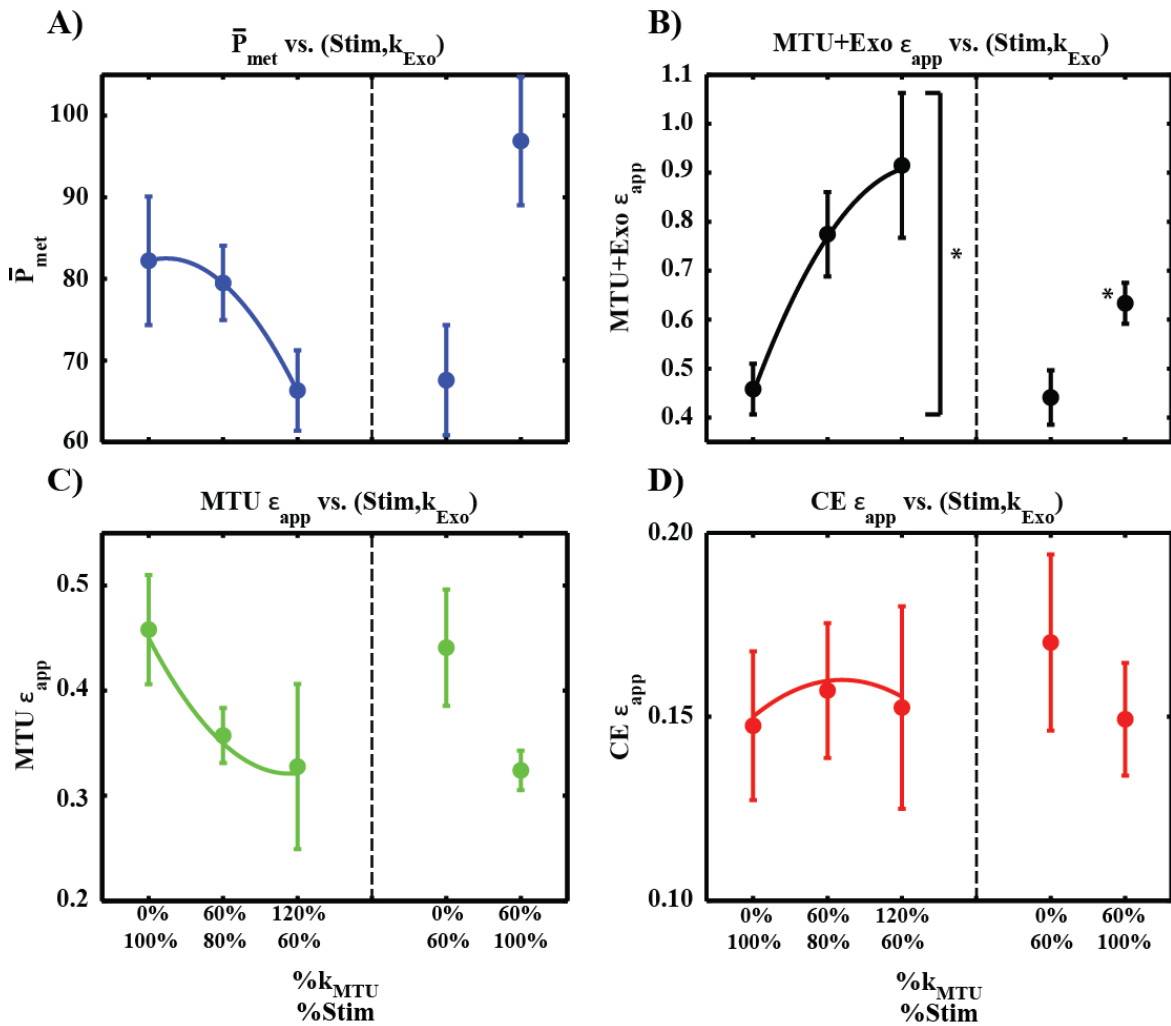


Figure 5, Estimated Metabolic Rate and Apparent Efficiency: Plots of mean \pm 1SE **A)** predicted \bar{P}_{met} **B)** MTU+Exo ϵ_{app} , **C)** MTU ϵ_{app} , and **D)** CE ϵ_{app} for all subjects and experimental conditions. Data to the left of the dashed line mimics human response to exo assistance, and regression trends are fit to compensation index values for these conditions. Significant trends are bracketed and starred. Data to the right of the dashed line is for decreased activation and increased k_{Exo} only conditions. Significant differences from the (100%Stim, 0% k_{MTU}) are indicated by stars on appropriate data points. Note that the addition of an Exo generally resulted in increased MTU+Exo ϵ_{app} , decreased \bar{P}_{met} and MTU ϵ_{app} , and nearly constant CE ϵ_{app} .

References

1. Ferris DP (2009) The exoskeletons are here. *J Neuroeng Rehabil* 6: 17.
2. Ferris DP, Lewis CL (2009) Robotic lower limb exoskeletons using proportional myoelectric control. *Conf Proc IEEE Eng Med Biol Soc* 2009: 2119-2124.
3. Hocoma.
4. Malcolm P, Derave W, Galle S, De Clercq D (2013) A simple exoskeleton that assists plantarflexion can reduce the metabolic cost of human walking. *PLoS One* 8: e56137.
5. Kawamoto H, Lee S, Kanbe S, Sankai Y. Power Assist Method for HAL-3 using EMG-based Feedback Controller; 2003. pp. 1648-1653.
6. Zoss AB, Kazerooni H, Chu A (2006) Biomechanical design of the Berkley lower extremity exoskeleton (BLEEX). *IEEE/ASME Transaction on Mechatronics* 11: 128-138.
7. Mooney LM, Rouse EJ, Herr HM (2014) Autonomous exoskeleton reduces metabolic cost of human walking during load carriage. *J Neuroeng Rehabil* 11: 80.
8. Wehner M, Quinlivan B, Aubin PM, Martinez-Villalpando E, Baumann M, et al. A Lightweight Soft Exosuit for Gait Assistance; 2013 May 6-10, 2013; Karlsruhe, Germany.
9. Wiggin MB, Sawicki GS, Collins SH. An exoskeleton using controlled energy storage and release to aid ankle propulsion; 2011. pp. 1-5.
10. Hasegawa Y, Ogura K. First report on passive exoskeleton for easy running: PEXER IV; 2013; Nagoya. IEEE. pp. 1-6.

11. Elliot G, G.S. S, A. M, Herr H. The biomechanics and energetics of human running using an elastic knee exoskeleton; 2013.
12. Geyer H, Seyfarth A, Blickhan R (2006) Compliant leg behaviour explains basic dynamics of walking and running. *Proc Biol Sci* 273: 2861-2867.
13. Farley CT, Blickhan R, Saito J, Taylor CR (1991) Hopping frequency in humans: a test of how springs set stride frequency in bouncing gaits. *J Appl Physiol* 71: 2127-2132.
14. Seyfarth A, Geyer H, Herr H (2003) Swing-leg retraction: a simple control model for stable running. *J Exp Biol* 206: 2547-2555.
15. Daley MA, Biewener AA (2006) Running over rough terrain reveals limb control for intrinsic stability. *Proc Natl Acad Sci U S A* 103: 15681-15686.
16. Shamaei K, Cenciarini M, Adams AA, Gregorczyk KN, Schiffman JM, et al. (2014) Design and Evaluation of a Quasi-Passive Knee Exoskeleton for Investigation of Motor Adaptation in Lower Extremity Joints. *IEEE Trans Biomed Eng (In Press)*.
17. Shamaei K, Sawicki GS, Dollar AM (2013) Estimation of quasi-stiffness and propulsive work of the human ankle in the stance phase of walking. *PLoS One* 8: e59935.
18. Shamaei K, Sawicki GS, Dollar AM (2013) Estimation of quasi-stiffness of the human knee in the stance phase of walking. *PLoS One* 8: e59993.
19. Shamaei K, Sawicki GS, Dollar AM (2013) Estimation of quasi-stiffness of the human hip in the stance phase of walking. *PLoS One* 8: e81841.
20. Farris DJ, Robertson BD, Sawicki GS (2013) Passive elastic exoskeletons reduce soleus muscle force but not work in human hopping. *J Appl Phys*.

21. Farris DJ, Sawicki GS (2012) Human medial gastrocnemius force-velocity behavior shifts with locomotion speed and gait. *Proc Natl Acad Sci U S A* 109: 977-982.
22. Takeshita D, Shibayama A, Muraoka T, Muramatsu T, Nagano A, et al. (2006) Resonance in the human medial gastrocnemius muscle during cyclic ankle bending exercise. *J Appl Physiol* 101: 111-118.
23. Roberts TJ, Azizi E (2011) Flexible mechanisms: the diverse roles of biological springs in vertebrate movement. *J Exp Biol* 214: 353-361.
24. Roberts TJ, Marsh RL, Weyand PG, Taylor CR (1997) Muscular force in running turkeys: the economy of minimizing work. *Science* 275: 1113-1115.
25. Barclay CJ, Lichtwark GA (2007) The mechanics of mouse skeletal muscle when shortening during relaxation. *J Biomech* 40: 3121-3129.
26. Lichtwark GA, Barclay CJ (2010) The influence of tendon compliance on muscle power output and efficiency during cyclic contractions. *J Exp Biol* 213: 707-714.
27. Farris DJ, Robertson BD, Sawicki GS (2013) Elastic ankle exoskeletons reduce soleus muscle force but not work in human hopping. *J Appl Physiol* (1985) 115: 579-585.
28. Farley CT, Blickhan R, Saito J, Taylor CR (1991) Hopping frequency in humans: a test of how springs set stride frequency in bouncing gaits. *J Appl Physiol* (1985) 71: 2127-2132.
29. Farley CT, Morgenroth DC (1999) Leg stiffness primarily depends on ankle stiffness during human hopping. *J Biomech* 32: 267-273.
30. Ferris DP, Bohra ZA, Lukos JR, Kinnaird CR (2006) Neuromechanical adaptation to hopping with an elastic ankle-foot orthosis. *J Appl Physiol* 100: 163-170.

31. Farris DJ, Sawicki GS (2012) Linking the mechanics and energetics of hopping with elastic ankle exoskeletons. *J Appl Physiol*.
32. Chang YH, Roiz RA, Auyang AG (2008) Intralimb compensation strategy depends on the nature of joint perturbation in human hopping. *J Biomech* 41: 1832-1839.
33. Grabowski AM, Herr HM (2009) Leg exoskeleton reduces the metabolic cost of human hopping. *J Appl Physiol* 107: 670-678.
34. Robertson BD, Farris DJ, G.S. S More is not always better: modeling the effects of elastic exoskeleton compliance on underlying ankle muscle-tendon dynamics. *Bioinspir Biomim: In Press*.
35. Lichtwark GA, Wilson AM (2005) A modified Hill muscle model that predicts muscle power output and efficiency during sinusoidal length changes. *J Exp Biol* 208: 2831-2843.
36. Caiozzo VJ, Baldwin KM (1997) Determinants of work produced by skeletal muscle: potential limitations of activation and relaxation. *Am J Physiol* 273: C1049-1056.
37. Sandercock TG, Heckman CJ (1997) Force from cat soleus muscle during imposed locomotor-like movements: experimental data versus Hill-type model predictions. *J Neurophysiol* 77: 1538-1552.
38. Curtin NA, Gardner-Medwin AR, Woledge RC (1998) Predictions of the time course of force and power output by dogfish white muscle fibres during brief tetani. *J Exp Biol* 201: 103-114.
39. Robertson BD, G.S. S Frequency-phase coupling in cyclically driven biological muscle-tendons. *Proceedings of the National Academy of Sciences of the United States of America: In Preparation*.

40. Farris DJ, Sawicki GS (2012) Linking the mechanics and energetics of hopping with elastic ankle exoskeletons. *J Appl Physiol* 113: 1862-1872.
41. Stevens ED (1996) The pattern of stimulation influences the amount of oscillatory work done by frog muscle. *J Physiol* 494 (Pt 1): 279-285.
42. Rack PM, Westbury DR (1969) The effects of length and stimulus rate on tension in the isometric cat soleus muscle. *J Physiol* 204: 443-460.
43. Pennycuik CJ (1964) Response of Fast Muscle Fibres to Series of Impulses. *J Exp Biol* 41: 291-298.
44. Robertson BD, Sawicki GS (2014) Exploiting elasticity: Modeling the influence of neural control on mechanics and energetics of ankle muscle-tendons during human hopping. *J Theor Biol* 353C: 121-132.
45. Azizi E, Roberts TJ (2010) Muscle performance during frog jumping: influence of elasticity on muscle operating lengths. *Proc Biol Sci* 277: 1523-1530.
46. Sheppard P, Sawicki GS, Roberts TJ. Power Augmentation in a Compliant Muscle-Tendon System; 2009 2009; State College, Pennsylvania.
47. Zajac FE (1989) Muscle and tendon: properties, models, scaling, and application to biomechanics and motor control. *Crit Rev Biomed Eng* 17: 359-411.
48. Josephson RK (1999) Dissecting muscle power output. *J Exp Biol* 202: 3369-3375.
49. Alexander RM (1997) Optimum Muscle Design for Oscillatory Movements. *Journal of Theoretical Biology* 184: 253-259.

50. Krishnaswamy P, Brown EN, Herr HM (2011) Human leg model predicts ankle muscle-tendon morphology, state, roles and energetics in walking. *PLoS Comput Biol* 7: e1001107.

51. Josephson RK, Stokes DR (1999) Work-dependent deactivation of a crustacean muscle. *J Exp Biol* 202: 2551-2565.

GENERAL CONCLUSIONS

Work presented here has successfully identified intrinsic mechanisms linking the form of biological systems back to their overall function. Much like a classic linear system, overall mechanical behavior was dependent on the system driving frequency (ω_{Drive}), and the system natural resonant frequency (ω_0) [1]. The numeric value of ω_0 was shown to depend on passive system stiffness (k), mass (M), and lever arm ratio (l_{in}/l_{out}) as follows:

$$\omega_0 = \left(l_{in}/l_{out} \right) \sqrt{k/M}$$

Evidence presented here also revealed an intrinsic frequency-phase coupling between driving and resonant frequency. The first two chapters reveal this by varying ω_{Drive} relative to a constant ω_0 , while the last two keep ω_{Drive} constant and add stiffness to increase ω_0 . In both cases, an ω_{Drive} well below ω_0 resulted in poor overall mechanical and energetic performance because of emergent phasing dynamics poorly suited for tuned interactions between muscle and tendon.

In addition to these findings, there is evidence to suggest that humans are able to identify their own resonant frequency in an ankle driven task. A study from Raburn et. al. demonstrates that, in an ankle driven bouncing task on an incline sled, humans adjust their frequency of movement in response to altered environments. In their study, adding mass drove preferred ω_{Drive} down, while added stiffness drove it up [2]. This is consistent with

expected changes in ω_0 for a linear system under added mass/increased stiffness conditions. In a followup study, Merritt et. al. demonstrate that $\omega_{Drive} = \omega_0$ is a preferred movement pattern in a sustained cyclic bouncing task. They also show that neuromechanical feedback modulates intrinsic limb ‘tuning’ by administering an ischemic block, and observing that human subjects are no longer able to find ω_0 [3].

This concept of ‘limb tuning’ is not only applicable to ankle driven tasks, but also observed patterns of pathological gait where reflex is still intact. For example, in the case of obese gait, one would expect added mass to reduce ω_0 , and ultimately ω_{Drive} for preferred patterns of movement. This expectation is confirmed by studies which observe significantly lower frequency of movement in obese individuals [4-6]. Another example of how these concepts apply in pathological gait is in elderly populations, where tendons become more compliant [7], lowering stiffness and ω_0 . One would expect elderly individuals to lower their frequency of movement to maintain tuned behavior. Interestingly, elderly prefer to maintain relatively high frequency of movement and develop ‘shuffling’ gait patterns [8]. While this poor selection of movement frequency may ultimately be the result of aberrant sensorimotor feedback [2,9,10], work presented here would suggest that high ω_{Drive} relative to system ω_0 should result in poorly tuned muscle-tendon interactions that cause series tendon to function as a buffer, rather than a springy transmission, between active muscle and environment. This would require active compensation from joints not dependent on elastic energy storage and return (i.e. hip). This is exactly what happens in elderly gait, resulting in

a ~300% increase in hip work occurring concomitantly with ~40% and 30% reductions in work produced at the knee and ankle respectively [8].

In the case of the elderly in particular, work presented here also suggests that efficient function might be restored through altered form. That is to say, passive exoskeletons of appropriate stiffness at the ankle and knee may be able to offset changes in tendon material properties [7], and ‘re-tune’ limb function by appropriately applying stiffness to insure resonant behavior at self-selected frequencies of movement.

While there are many other factors influencing that can influence pathological gait patterns not addressed here (i.e. altered proprioceptive feedback, traumatic injury, asymmetry due to injury or atrophy, etc.), concepts related to form and function still apply. It is my hope that, in highlighting the relationship between limb form and function, this work provides a simple conceptual framework for conceptual design clinical intervention. The technology required for this already exists (e.g. ankle-foot orthoses to alter stiffness or biological moment arms, body weight support systems for reducing inertial loads), but it remains to be seen whether these tools can be intelligently applied to enhance clinical outcomes.

References

1. Ogata K (2003) System Dynamics. Upper Saddle River, NJ: Prentice Hall.
2. Raburn CE, Merritt KJ, Dean JC (2011) Preferred movement patterns during a simple bouncing task. *J Exp Biol* 214: 3768-3774.
3. Merritt KJ, Raburn CE, Dean JC (2012) Adaptation of the preferred human bouncing pattern toward the metabolically optimal frequency. *J Neurophysiol* 107: 2244-2249.
4. DeVita P, Hortobagyi T (2003) Obesity is not associated with increased knee joint torque and power during level walking. *J Biomech* 36: 1355-1362.
5. Peyrot N, Morin JB, Thivel D, Isacco L, Taillardat M, et al. (2010) Mechanical work and metabolic cost of walking after weight loss in obese adolescents. *Med Sci Sports Exerc* 42: 1914-1922.
6. Browning RC, Kram R (2007) Effects of obesity on the biomechanics of walking at different speeds. *Med Sci Sports Exerc* 39: 1632-1641.
7. Magnusson SP, Narici MV, Maganaris CN, Kjaer M (2008) Human tendon behaviour and adaptation, in vivo. *J Physiol* 586: 71-81.
8. DeVita P, Hortobagyi T (2000) Age causes a redistribution of joint torques and powers during gait. *J Appl Physiol* (1985) 88: 1804-1811.
9. Gu MJ, Schultz AB, Shepard NT, Alexander NB (1996) Postural control in young and elderly adults when stance is perturbed: dynamics. *J Biomech* 29: 319-329.
10. Petrella RJ, Lattanzio PJ, Nelson MG (1997) Effect of age and activity on knee joint proprioception. *Am J Phys Med Rehabil* 76: 235-241.